Journal of Research of the National Bureau of Standards

In This Issue:

Vol. 92, No. 2, March–April 1987

Departments

News Briefs

News Reports

Conferences/Events

Articles

News Briefs

Developments

NBS CONTRIBUTING TO CANCER PREVENTION STUDY

Can supplemental doses of certain vitamins and minerals reduce cancer risks? NBS is helping answer this question by contributing to a larger government study—sponsored by the National Cancer Institute (NCI)—that is examining the cancer preventive properties of "micronutrients." These are compounds, such as vitamins A, C, and E, which may help prevent some tumors in persons at high risk due to lifestyle or occupational exposure, or in those who have had cancer but now are free of the disease.

Accurate measurements of nutrients in blood serum are crucial to the NCI study, so NBS has established a "quality assurance" program to ensure that the 20 laboratories participating in the program make reliable nutrient measurements in blood samples. To perform these quality checks, NBS sends samples with known values to the labs for analysis. If results are inaccurate, the Bureau suggests ways to improve. Ultimately, serum nutrient values will be correlated with the occurrence or recurrence of cancer in populations being studied.

For further information, contact Willie May, National Bureau of Standards, Gaithersburg, MD 20899 or Herbert Pierson, National Cancer Institute, Bethesda, MD 20892.

AUTOMATION LABORATORY COMPLETED

NBS has completed construction work on a unique automation laboratory designed as a proving ground for the technology of America's factories in the 21st century. This laboratory, called the Automated Manufacturing Research Facility (AMRF), will aid both large and small American manufacturers. The facility is a collaborative venture involving private industry, universities, and other government agencies, most notably the U.S. Navy.

Under construction since 1983, the AMRF is a research laboratory designed to study standard methods to link different computerized machines. It also is used to help manufacturers improve quality control by experimenting with efficient and reliable methods for monitoring the performance of automated machinery.

For further information, contact John Simpson, National Bureau of Standards, Gaithersburg, MD 20899.

PATENT GRANTED FOR HYDROPHOBIC DENTAL COMPOSITES

A patent has been granted for a dental composite system developed by NBS that offers dentists a material with improved wear and stability, as well as greater resistance to surface staining and discoloration. The composite system contains a high concentration of bulky fluorinated monomers that are highly immune to chemical softening and degradation in the oral environment.

Hydrophobic Dental Composites Based on a Polyfluorinated Dental Resin, Patent No. 4,616,073, was developed by NBS researcher Joseph M. Antonucci for the National Institute of Dental Research. The resin system can be used in two different ways; it can be cured photochemically with a dental light pen, or it can be cured as a two-part monomer system. Among the other advantages of this type of dental composite resin system based on hydrophobic polymer matrices are its low water sorption and low shrinkage especially at composite-cavity interfaces when used in dental restorations.

NBS DEVELOPS NEW WAY TO MEASURE STEEL ROUGHNESS

NBS researchers have developed a new way to measure the roughness of steel which has been "blasted" with an abrasive, such as sand. Blasting is a cleaning process which prepares a material for a coating. Surface roughness affects the life of the coating, but the exact relationship is not well understood since precise measurements are difficult and time consuming to make.

The NBS method uses an infrared thermographic camera coupled with a computer image processor to produce a depth profile—a pattern of the peaks and valleys—of the steel. Surface roughness can then be mathematically described. The procedure is faster and more precise than current methods. In addition, the measurements can be made without touching the material. Currently, the NBS researchers are experimenting with the procedure to see if it can be used to characterize engineered surfaces and whether it can be adapted to in-line processing such as spray-painting assembly lines.

For further information, contact Jonathan Martin, National Bureau of Standards, Gaithersburg, MD 20899.

ELECTROMAGNETIC COMPATIBILITY AND INTERFERENCE MEASUREMENTS

Electromagnetic compatibility/interference measurements are used to determine how electronic equipment undesirably generates or is affected by electromagnetic radiation. Reliable, accurate EMC/EMI measurements are essential to the design and operation of a broad variety of electronic equipment and products used in automotive, household, industrial, business, and military applications.

A new NBS publication [1] includes the text material for a short course in EMC/EMI measurements presented by NBS. It sets out basic EMC measurements, and includes chapters on measurements made using transverse electromagnetic (TEM) cells, anechoic chambers, open fields, reverberating chambers, and EM probes. Other chapters deal with measurement of the shielding effectiveness of materials, out-of-band EMC problems, conducted EMI, and complicated electromagnetic environments.

Reference

[1] NBS TN 1099, Electromagnetic Compatibility and Interference Metrology, Superintendent of Documents, U.S. Government Printing Office, Washington, DC 20402 ($8.50 prepaid, order by Stock No. 003-003-02760-0).

ARMSTRONG WORLD TO PERFORM POLYMER RESEARCH AT NBS

Armstrong World Industries, Lancaster, PA, has established a Research Associate Program at NBS to study the permeability of polymer composites to freon gases. An Armstrong researcher will use the NBS computerized volatile gas permeation facility to measure the gas transport properties of a series of polymers used as components in polymer blends. The information will be used to process blends into thermal insulating foams. The NBS Research Associate Program provides an opportunity for researchers from universities, industry, trade associations, and other organizations to conduct cooperative work at the Bureau on projects of mutual interest, with salaries paid by the sponsor.

For further information on the Research Associate Program, contact David Edgerly, National Bureau of Standards, Gaithersburg, MD 20899, telephone: 301/975-3087.

ASSESSING ELECTROEXPLOSIVE DEVICE VULNERABILITY

Hot-wire electroexplosive devices (EEDs) are electrically fired explosive initiators. They are used as automotive air bag initiators, separation devices in aerospace applications (explosive bolts), and many other military, mining, and construction applications. A new and rigorous approach for assessing an EED's vulnerability to pulsed electromagnetic interference is given in a recent NBS report [1]. This method uses statistical theory and thermodynamic modeling to determine the probability that an electrical pulse of a given duration and power will detonate the EED, and to determine thermodynamic parameters. The "Firing Likelihood Plot" is introduced to represent an EED's characteristic in a readily interpretable manner.

Reference

[1] NBS TN 1094, A Statistical Characterization of Electroexplosive Devices Relevant to Electromagnetic Compatibility Assessment, Superintendent of Documents, U.S. Government Printing Office, Washington, DC 20402 ($2.75 prepaid, order by Stock No. 003-003-02744-8).

MEASURING SHIELDING EFFECTIVENESS OF MATERIALS

The shielding effectiveness of a material is a measure of how well it is able to isolate a region from electromagnetic fields. Shielding is used to protect equipment from outside interference or to reduce unwanted emissions from equipment. While traditional metal shields have characteristics that are well understood, the recent use of more complex materials with less predictable shielding properties, such as plastic housings and composites, has made measurement of the shielding effectiveness essential.

In a new publication [1], NBS reports on an evaluation of several measurement approaches.

Reference

[1] NBS TN 1095, A Study of Techniques for Measuring the Electromagnetic Shielding Effectiveness of Materials, Superintendent of Documents, U.S. Government Printing Office, Washington, DC 20402 ($3.50 prepaid, order by stock No. 003-003-02735-9).

REPORT SUMMARIZES QUALITY ASSURANCE LITERATURE

Analytical chemists, laboratory managers, and quality assurance (QA) officials should find a new NBS report useful [1]. It contains abstracts of 160 papers selected as source materials for starting new QA programs or improving existing ones. The papers also are good resources for general guidance in producing reliable analytical chemical measurements. John K. Taylor, who has taught 75 NBS chemical QA workshops to industrial, academic, and government participants over the last 7 years, assembled the report. Taylor, who recently retired after 57 years at NBS, says much has been written on quality assurance of production processes, but considerably less is available about measurement QA, especially about chemical measurements. His goal in writing the 51-page report was to provide a good summary of what is available in chemical QA materials.

Reference

[1] NBSIR 86-3352, A Collection of Abstracts of Selected Publications Related to Quality Assurance of Chemical Measurements, National Technical Information Service (NTIS), Springfield, VA 22161 ($11.95 prepaid, order by PB# 87-106423).

DRAFT FEDERAL OSI STANDARD CIRCULATED FOR REVIEW

A draft specification for the acquisition of Federal Government computer systems that conform to the Open Systems Interconnection (OSI) standards has been completed by the Government OSI Users Committee, sponsored by NBS. The specification is based on a cooperative effort between NBS and industry to implement emerging OSI standards in commercial, off-the-shelf products, and is compatible with both the Manufacturing Automation Protocol (MAP) and the Technical and Office Protocols (TOP) which have been developed by industry. NBS is circulating the draft specification to Federal agencies and to industry and standards organizations for review before recommending its adoption as a joint Federal Information Processing Standard/Federal Telecommunication Standard for use in 1987 and 1988 procurements.

For further information, contact Shirley Radack, National Bureau of Standards, Gaithersburg, MD 20899.

Standard Reference Data

NBS DEVELOPS COMPUTERIZED DATABASE FROM AIChE/DIPPR STANDARD REFERENCE SOURCE ON PURE CHEMICAL COMPOUNDS

Chemical manufacturers; engineers who design plants; chemical processes, and new products; as well as scientists in industry, government, and universities will be interested in a new computerized standard reference database from NBS on the thermodynamic and physical properties of chemicals.

The new computerized database provides users with quick access to important information on the behavior of substances and their reactions under various pressures and temperatures. It was produced under an agreement between NBS and the American Institute of Chemical Engineers (AIChE).

The database, DIPPR (Design Institute for Physical Property Data), Data Compilation of Pure Compound Properties, 1986, contains information on 39 properties for 346 chemical compounds of high industrial priority. These chemicals were selected by the industry members of AIChE's DIPPR group, a cooperative organization of chemical manufacturers and related companies. The chemicals in the database are considered to be the most important ones to users, based on their volume of production and other economic factors.

Information is provided on the thermodynamic, physical, and transport properties of each chemical. And for each compound included, values are given for 26 single-valued property constants and for 13 properties as functions of temperature, calculated from correlation coefficients.

The database, which is interactive or "conversational" for users, also includes estimates of the accuracy of each property value and provides references to the sources of measured or predicted data that were used in selecting the recommended values.

It was automated by the NBS Office of Standard Reference Data from AIChE's 1985 resource book, Data Compilation: Tables of Properties of Pure Compounds. This printed database was prepared for DIPPR by Thomas E. Daubert and Ronald P. Danner of Pennsylvania State University.

The printed reference is one of several cooperative projects on evaluated standard data to be sponsored by industry through DIPPR. NBS has provided technical support to the industrial group since it was established by AIChE in 1978, particularly in the area of computerized information.

AIChE is a national organization of 60,000 scientists and engineers in research and manufacturing.

NBS Standard Reference Database 11, DIPPR, Data Compilation of Pure Compound Properties, 1986, are one of 11 databases in magnetic tape form that is available from OSRD for lease to individuals, distributors, or subscription search services. For information on fees and lease agreements for DIPPR, or for a list of the other computerized standard reference databases available from NBS, contact: Office of Standard Reference Data, A323 Physics Building, National Bureau of Standards, Gaithersburg, MD 20899, telephone: 301/975-2208.

MICROCOMPUTER FORTRAN PROGRAMS CALCULATE FLUID PROPERTIES

The thermophysical and transport properties of 12 selected fluids have been programmed in FORTRAN 77 for microcomputers. When any two of pressure, temperature, or density values are input (in single phase regions), or either pressure or temperature (in saturated liquid or vapor states), the programs calculate pressure, density, temperature, internal energy, enthalpy, entropy, specific heat capacities (Cv and Cp), speed of sound, and in most cases, viscosity, thermal conductivity, and dielectric constant.

The fluids included are helium, hydrogen, nitrogen, oxygen, argon, nitrogen trifluoride, methane, ethylene, ethane, propane, iso- and normal butane. Properties are given over a wide range of temperatures and pressures.

A description and listing of the program, along with sample calculations and a typical computer run, is available in a recent NBS publication [1].

Copies of the program on microcomputer diskette are available for $400 from the Office of Standard Reference Data, A320 Physics Building, National Bureau of Standards, Gaithersburg, MD 20899, telephone: 301/975-2208.

Reference

[1] NBS TN 1097, Interactive FORTRAN Programs for Microcomputers to Calculate the Thermophysical Properties of Twelve Fluids (MIPROPS), Superintendent of Documents, U.S. Government Printing Office, Washington, DC 20402 ($4.25 prepaid, order by stock No. 003-003-02745-6).

NBS Services

NBS AND USAF SIGN MEMO OF UNDERSTANDING ON MILSTAR

NBS and the U.S. Air Force have reached agreement on a two-year program to develop millimeter-wave metrology and standards in support of the Milstar Satellite Communications System. Milstar is the next generation of extremely sophisticated military communications satellites. NBS will receive a total of $2.8 million over fiscal years 1987 and 1988 to develop measurement services and standards support over a wide range of parameters including millimeter wave power, impedance, noise temperature, antenna gain, and phase noise. The work will be carried out principally in the 19-22 and 42-46 GHz range. This program will enable NBS to provide interim (special test) measurement services to the three military branches, Milstar contractors, and their subcontractors.

Direct inquiries to Ernest Garner, National Bureau of Standards, Gaithersburg, MD 20899, telephone: 301/975-2007.

News Reports

FREE-ELECTRON LASER FACILITY TO BE CONSTRUCTED AT NBS

An important new national facility for research in physics, materials science, and biomedicine will be constructed at NBS under a congressionally authorized program aimed at exploiting free-electron lasers in biomedical and materials science.

A proposal to build the new facility, submitted jointly by NBS and the Naval Research Laboratory, has been recommended for funding by the Office of Naval Research and the Air Force Office of Scientific Research. The two agencies jointly manage the free-electron laser research program for the Strategic Defense Initiative Organization. That organization would provide $4.9 million to build the facility.

A free-electron laser is an exotic light source in which the gases, liquids, or crystals normally used to produce the laser effect are replaced by bunches of electrons traveling through a periodically varying magnetic field. Such lasers are capable of very short, intense bursts of light that can be tuned very finely across a broad range of frequencies.

The new laser will be constructed in the accelerator complex at the NBS laboratories in Gaithersburg, MD, and will be driven by the Bureau's 185 MeV continuous wave (cw) racetrack microtron, which is currently nearing completion. The cw microtron is an experimental electron accelerator, being built in collaboration with Los Alamos National Laboratory. It will be one of the most powerful high-current cw accelerators in the world.

When completed in 1990, the free-electron laser will supply light in the wavelength range of 0.2 micrometer to 10 micrometers, with a bandwidth on the order of 0.001, at average power levels of hundreds of watts. In addition, copious amounts (milliwatts to watts) of coherent UV light will be produced at harmonics of the laser frequency down to wavelengths of approximately 30 nm.

The light will be a continuous train of 3-ps pulses at repetition frequencies of 20 MHz or 100 MHz. This pulse length is of particular interest in the study of organic and biological molecules.

The unique properties of the free-electron laser, including broad wavelength tunability, high peak and average power, and extremely short pulse lengths, open up a broad range of exciting new research opportunities in such diverse areas as atomic and molecular physics, surface science, photochemistry, biophysics and biomedicine.

An external advisory panel comprised of senior scientists and managers from the academic, industrial and government sectors will help guide the project.

Plans for the facility call for close collaboration with the medical and materials science communities, including the Uniformed Services University of the Health Sciences, the Food and Drug Administration, the Center for Advanced Research in Biotechnology, and a number of universities in the Washington, DC, metropolitan area.

For further information, contact Samuel Penner, National Bureau of Standards, Gaithersburg, MD 20899.

Journal of Research of the National Bureau of Standards

The 1986 CODATA Recommended Values Of the Fundamental Physical Constants

Volume 92 Number 2 March–April 1987

E. Richard Cohen

Rockwell International
Science Center
Thousand Oaks, CA 91360

Barry N. Taylor

National Bureau of Standards
Gaithersburg, MD 20899

This paper gives the values of the basic constants and conversion factors of physics and chemistry resulting from the 1986 least-squares adjustment of the fundamental physical constants as recently published by the CODATA Task Group on Fundamental Constants and as recommended for international use by CODATA. The new, 1986 CODATA set of recommended values replaces its predecessor published by the Task Group and recommended for international use by CODATA in 1973.

Key words: CODATA; conversion factors; fundamental physical constants; least-squares adjustments; recommended values; Task Group on Fundamental Constants.

Accepted: January 14, 1987.

CODATA (Committee on Data for Science and Technology[1]) has recently published a report of the CODATA Task Group on Fundamental Constants prepared by the authors [1][2] under the auspices and guidance of the Task Group. The report summarizes the 1986 least-squares adjustment of the fundamental physical constants and gives a set of self-consistent values for the basic constants and conversion factors of physics and chemistry derived from that adjustment. Recommended for international use by CODATA, this 1986 set of values is reprinted here for the convenience of the many readers of the *Journal of Research of the National Bureau of Standards* and to assist in its dissemination throughout the scientific and technological communities. The 1986 CODATA set entirely replaces its immediate predecessor, that recommended for international use by CODATA in 1973. This set was based on the 1973 least-squares adjustment of the fundamental physical constants which was also carried out by the authors under the auspices and guidance of the Task Group [2,3].

As in previous least-squares adjustments of the constants [3,4,5], the data for the 1986 adjustment were divided into two groups: auxiliary constants and stochastic input data. Examples of the 1986 auxiliary constants are the speed of light in vacuum $c=299792458$ m/s; the permittivity of vacuum $\mu_0=4\pi\times10^{-7}$ N/A^2; the Rydberg constant for infinite mass R_∞; and the quantity $E=483594.0\times10^9$ Hz/V which is equal numerically to the value of the Josephson frequency-voltage ratio $2e/h$ (e is the elementary charge and h is the Planck constant) adopted in 1972 by the Consultative Committee on Electricity of the International Committee of

About the Authors: E. Richard Cohen is Distinguished Fellow, Rockwell International Science Center, and Barry N. Taylor is chief of the Electricity Division in the Center for Basic Standards, part of the NBS National Measurement Laboratory. Both Drs. Cohen and Taylor are physicists and members of the CODATA Task Group on Fundamental Constants.

---

[1] CODATA was established in 1966 as an interdisciplinary committee of the International Council of Scientific Unions. It seeks to improve the compilation, critical evaluation, storage, and retrieval of data of importance to science and technology. Dr. David R. Lide, chief of the NBS Office of Standard Reference Data, is the current President of CODATA.

[2] Figures in brackets indicate literature references.

Weights and Measures for defining laboratory representations of the volt [6,7]. Quantities in this category are either defined constants such as c, μ_0, and E with no uncertainty, or constants such as R_∞ with assigned uncertainties sufficiently small in comparison with the uncertainties assigned the stochastic input data with which they are associated in the adjustment that they can be taken as exact (i.e., their values are not subject to adjustment in contrast to the stochastic data). In the 1986 adjustment the uncertainty of each auxiliary constant was no greater than 0.02 parts-per-million or ppm.[3] In contrast, the uncertainties assigned the 38 items of stochastic input data considered in the 1986 adjustment were in the range 0.065 to 9.7 ppm. (The 38 items were of 12 distinct types with the number of items of each type ranging from one to six.) Examples of such data are measurements of the proton gyromagnetic ratio γ'_p (uncertainty in the range 0.24 to 5.4 ppm), the molar volume of silicon $M(\mathrm{Si})/\rho(\mathrm{Si})$ (1.15 ppm), and the quantized Hall resistance $R_H=h/e^2$ (0.12 to 0.22 ppm).

Because new results which can influence a least-squares adjustment of the constants are reported continually, it is always difficult to choose an optimal time at which to carry out a new adjustment and to revise the recommended values of the constants. In the present case, all data available up to 1 January 1986 were considered for inclusion, with the recognition that any additional changes to the 1973 recommended values that might result by taking into account more recent data would be much less than the changes resulting from the data available prior to that date.

Each of the 38 items of stochastic data are expressed (using the auxiliary constants as necessary) in terms of five quantities that serve as the "unknowns" or variables of the 1986 adjustment. These are α^{-1}, the inverse fine-structure constant; K_V, a dimensionless quantity relating the SI (International System of Units) volt V to the unit of voltage $V_{76\text{-BI}}$ maintained at the International Bureau of Weights and Measures (BIPM) using a value of the Josephson frequency-voltage ratio equal numerically to E: $V_{76\text{-BI}}=K_V$ V, and thus $2e/h=E/K_V$; K_Ω, a dimensionless quantity relating the SI ohm to the BIPM as-maintained unit of resistance as it existed on 1 January 1985, Ω_{BI85}, based on the mean resistance of a particular group of wire-wound precision resistors: $\Omega_{BI85}=K_\Omega\ \Omega$; d_{220}, the (220) lattice spacing of a perfect crystal of pure silicon at 22.5 °C in vacuum; and μ_μ/μ_p, the ratio of the magnetic moment of the muon to that of the proton. "Best" values in the least-squares sense for these five quantities, with their variances and covariances, are thus the immediate output of the adjustment.

After a thorough analysis using a number of least-squares algorithms, the initial group of 38 items of stochastic input data was reduced to 22 items by deleting those that were either highly inconsistent with the remaining data or had assigned uncertainties so large that they carried negligible weight. The adjusted values of the five unknowns, and hence all the other 1986 recommended values that were subsequently derived from them (with the aid of the auxiliary constants), are therefore based on a least-squares adjustment with 17 degrees of freedom.

The 1986 adjustment represents a major advance over its 1973 counterpart; the uncertainties of the recommended values have been reduced by roughly an order of magnitude due to the enormous advances made throughout the precision measurement-fundamental constants field in the last dozen years. This can be seen from the following comparison of the 1973 and 1986 recommended values for the inverse fine-structure constant α^{-1}, the elementary charge e, the Planck constant h, the electron mass m_e, the Avogadro constant N_A, the proton electron mass ratio m_p/m_e, the Faraday constant F, and the Josephson frequency-voltage ratio $2e/h$:

	Uncertainty of recommended value in ppm		Change in 1973 recommended value in ppm resulting from 1986 adjustment
Quantity	1973	1986	
α^{-1}	0.82	0.045	−0.37
e	2.9	0.30	−7.4
h	5.4	0.60	−15.2
m_e	5.1	0.59	−15.8
N_A	5.1	0.59	+15.2
m_p/m_e	0.38	0.020	+0.64
F	2.8	0.30	+7.8
$2e/h$	2.6	0.30	+7.8

It is also clear from this comparison that unexpectedly large changes have occurred in the 1973 recommended values of a number of these constants (i.e., a change which is large relative to the uncertainty assigned the 1973 value). These changes are a direct consequence of the 7.8 ppm decrease from 1973 to 1986 in the quantity K_V and the high correlation between K_V and the calculated values of e, h, m_e, N_A, and F. Since $2e/h=E/K_V$, the 1986 value of K_V also implies that the value of the Josephson frequency-voltage ratio adopted by the Consultative Committee on Electricity in 1972, which was believed to be consistent with the SI value and which most national standards laborato-

---

[3] Throughout, all uncertainties are one standard deviation estimates.

ries adopted to define and maintain their laboratory unit of voltage, is actually 7.8 ppm smaller than the SI value. This unsatisfactory situation should be rectified in the near future [8,9].

The large change in K_V and hence in many other quantities between 1973 and 1986 would have been avoided if two determinations of F which seemed to be discrepant with the remaining data had not been deleted in the 1973 adjustment. In retrospect, the disagreement was comparatively mild. In view of this experience it is important to recognize that there are no similar disagreements in the 1986 adjustment; the measurements which were deleted were so discrepant that they obviously could not be correct, or of such low weight that if retained the adjusted values of the five unknowns would change negligibly. Thus, it is unlikely that any alternate evaluation of the data considered in the 1986 least-squares adjustment could lead to significant changes in the 1986 recommended values. Moreover, the quality of the 1986 data and its redundancy would seem to preclude future changes in the 1986 recommended values relative to their uncertainties comparable to the changes which occurred in the 1973 values.

The 1986 recommended values of the fundamental physical constants are given in five tables. Table 1 is an abbreviated list containing the quantities which should be of greatest interest to most users. Table 2 is a much more complete compilation.

Table 1. Summary of the 1986 recommended values of the fundamental physical constants.

An abbreviated list of the fundamental constants of physics and chemistry based on a least-squares adjustment with 17 degrees of freedom. The digits in parentheses are the one-standard-deviation uncertainty in the last digits of the given value. Since the uncertainties of many of these entries are correlated, the full covariance matrix must be used in evaluating the uncertainties of quantities computed from them.

Quantity	Symbol	Value	Units	Relative Uncertainty (ppm)
speed of light in vacuum	c	299 792 458	$\mathrm{m\,s^{-1}}$	(exact)
permeability of vacuum	μ_0	$4\pi\times10^{-7}$	$\mathrm{N\,A^{-2}}$	
		$=12.566\,370\,614\ldots$	$10^{-7}\,\mathrm{N\,A^{-2}}$	(exact)
permittivity of vacuum	ϵ_0	$1/\mu_0 c^2$		
		$=8.854\,187\,817\ldots$	$10^{-12}\,\mathrm{F\,m^{-1}}$	(exact)
Newtonian constant of gravitation	G	6.672 59(85)	$10^{-11}\,\mathrm{m^3\,kg^{-1}\,s^{-2}}$	128
Planck constant	h	6.626 0755(40)	$10^{-34}\,\mathrm{J\,s}$	0.60
$h/2\pi$	$\hbar$	1.054 572 66(63)	$10^{-34}\,\mathrm{J\,s}$	0.60
elementary charge	e	1.602 177 33(49)	$10^{-19}\,\mathrm{C}$	0.30
magnetic flux quantum, $h/2e$	Φ_0	2.067 834 61(61)	$10^{-15}\,\mathrm{Wb}$	0.30
electron mass	m_e	9.109 3897(54)	$10^{-31}\,\mathrm{kg}$	0.59
proton mass	m_p	1.672 6231(10)	$10^{-27}\,\mathrm{kg}$	0.59
proton-electron mass ratio	m_p/m_e	1836.152 701(37)		0.020
fine-structure constant, $\mu_0 ce^2/2h$	α	7.297 353 08(33)	10^{-3}	0.045
inverse fine-structure constant	α^{-1}	137.035 9895(61)		0.045
Rydberg constant, $m_e c\alpha^2/2h$	R_∞	10 973 731.534(13)	$\mathrm{m^{-1}}$	0.0012
Avogadro constant	N_A, L	6.022 1367(36)	$10^{23}\,\mathrm{mol^{-1}}$	0.59
Faraday constant, $N_A e$	F	96 485.309(29)	$\mathrm{C\,mol^{-1}}$	0.30
molar gas constant	R	8.314 510(70)	$\mathrm{J\,mol^{-1}\,K^{-1}}$	8.4
Boltzmann constant, R/N_A	k	1.380 658(12)	$10^{-23}\,\mathrm{J\,K^{-1}}$	8.5
Stefan–Boltzmann constant, $(\pi^2/60)k^4/\hbar^3c^2$	σ	5.670 51(19)	$10^{-8}\,\mathrm{W\,m^{-2}\,K^{-4}}$	34
		Non-SI units used with SI		
electron volt, $(e/\mathrm{C})\,\mathrm{J} = \{e\}\,\mathrm{J}$	eV	1.602 177 33(49)	$10^{-19}\,\mathrm{J}$	0.30
(unified) atomic mass unit, $1\ \mathrm{u} = m_u = \frac{1}{12}m(^{12}\mathrm{C})$	u	1.660 5402(10)	$10^{-27}\,\mathrm{kg}$	0.59

Table 2. The 1986 recommended values of the fundamental physical constants.

This list of the fundamental constants of physics and chemistry is based on a least-squares adjustment with 17 degrees of freedom. The digits in parentheses are the one-standard-deviation uncertainty in the last digits of the given value. Since the uncertainties of many of these entries are correlated, the full covariance matrix must be used in evaluating the uncertainties of quantities computed from them.

Quantity	Symbol	Value	Units	Relative Uncertainty (ppm)
GENERAL CONSTANTS				
Universal Constants				
speed of light in vacuum	c	299 792 458	$\mathrm{m\,s^{-1}}$	(exact)
permeability of vacuum	μ_0	$4\pi \times 10^{-7}$	$\mathrm{N\,A^{-2}}$	
		=12.566 370 614...	$10^{-7}\,\mathrm{N\,A^{-2}}$	(exact)
permittivity of vacuum	ϵ_0	$1/\mu_0 c^2$		
		=8.854 187 817...	$10^{-12}\,\mathrm{F\,m^{-1}}$	(exact)
Newtonian constant of gravitation	G	6.672 59(85)	$10^{-11}\,\mathrm{m^3\,kg^{-1}\,s^{-2}}$	128
Planck constant	h	6.626 0755(40)	$10^{-34}\,\mathrm{J\,s}$	0.60
in electron volts, $h/\{e\}$		4.135 6692(12)	$10^{-15}\,\mathrm{eV\,s}$	0.30
$h/2\pi$	$\hbar$	1.054 572 66(63)	$10^{-34}\,\mathrm{J\,s}$	0.60
in electron volts, $\hbar/\{e\}$		6.582 1220(20)	$10^{-16}\,\mathrm{eV\,s}$	0.30
Planck mass, $(\hbar c/G)^{\frac{1}{2}}$	m_P	2.176 71(14)	$10^{-8}\,\mathrm{kg}$	64
Planck length, $\hbar/m_\mathrm{P}c = (\hbar G/c^3)^{\frac{1}{2}}$	l_P	1.616 05(10)	$10^{-35}\,\mathrm{m}$	64
Planck time, $l_\mathrm{P}/c = (\hbar G/c^5)^{\frac{1}{2}}$	t_P	5.390 56(34)	$10^{-44}\,\mathrm{s}$	64
Electromagnetic Constants				
elementary charge	e	1.602 177 33(49)	$10^{-19}\,\mathrm{C}$	0.30
	e/h	2.417 988 36(72)	$10^{14}\,\mathrm{A\,J^{-1}}$	0.30
magnetic flux quantum, $h/2e$	Φ_0	2.067 834 61(61)	$10^{-15}\,\mathrm{Wb}$	0.30
Josephson frequency–voltage ratio	$2e/h$	4.835 9767(14)	$10^{14}\,\mathrm{Hz\,V^{-1}}$	0.30
quantized Hall conductance	e^2/h	3.874 046 14(17)	$10^{-5}\,\mathrm{S}$	0.045
quantized Hall resistance, $h/e^2 = \mu_0 c/2\alpha$	R_H	25 812.8056(12)	Ω	0.045
Bohr magneton, $e\hbar/2m_\mathrm{e}$	μ_B	9.274 0154(31)	$10^{-24}\,\mathrm{J\,T^{-1}}$	0.34
in electron volts, $\mu_\mathrm{B}/\{e\}$		5.788 382 63(52)	$10^{-5}\,\mathrm{eV\,T^{-1}}$	0.089
in hertz, μ_B/h		1.399 624 18(42)	$10^{10}\,\mathrm{Hz\,T^{-1}}$	0.30
in wavenumbers, μ_B/hc		46.686 437(14)	$\mathrm{m^{-1}\,T^{-1}}$	0.30
in kelvins, μ_B/k		0.671 7099(57)	$\mathrm{K\,T^{-1}}$	8.5
nuclear magneton, $e\hbar/2m_\mathrm{p}$	μ_N	5.050 7866(17)	$10^{-27}\,\mathrm{J\,T^{-1}}$	0.34
in electron volts, $\mu_\mathrm{N}/\{e\}$		3.152 451 66(28)	$10^{-8}\,\mathrm{eV\,T^{-1}}$	0.089
in hertz, μ_N/h		7.622 5914(23)	$\mathrm{MHz\,T^{-1}}$	0.30
in wavenumbers, μ_N/hc		2.542 622 81(77)	$10^{-2}\,\mathrm{m^{-1}\,T^{-1}}$	0.30
in kelvins, μ_N/k		3.658 246(31)	$10^{-4}\,\mathrm{K\,T^{-1}}$	8.5

Table 2. The 1986 recommended values of the fundamental physical constants (continued).

Quantity	Symbol	Value	Units	Relative Uncertainty (ppm)
ATOMIC CONSTANTS				
fine-structure constant, $\mu_0 ce^2/2h$	α	7.297 353 08(33)	10^{-3}	0.045
inverse fine-structure constant	α^{-1}	137.035 9895(61)		0.045
Rydberg constant, $m_e c\alpha^2/2h$	R_∞	10 973 731.534(13)	m^{-1}	0.0012
in hertz, $R_\infty c$		3.289 841 9499(39)	10^{15} Hz	0.0012
in joules, $R_\infty hc$		2.179 8741(13)	10^{-18} J	0.60
in eV, $R_\infty hc/\{e\}$		13.605 6981(40)	eV	0.30
Bohr radius, $\alpha/4\pi R_\infty$	a_0	0.529 177 249(24)	10^{-10} m	0.045
Hartree energy, $e^2/4\pi\epsilon_0 a_0 = 2R_\infty hc$	$E_{\rm h}$	4.359 7482(26)	10^{-18} J	0.60
in eV, $E_{\rm h}/\{e\}$		27.211 3961(81)	eV	0.30
quantum of circulation	$h/2m_e$	3.636 948 07(33)	$10^{-4}\ \mathrm{m^2\,s^{-1}}$	0.089
	h/m_e	7.273 896 14(65)	$10^{-4}\ \mathrm{m^2\,s^{-1}}$	0.089
Electron				
electron mass	m_e	9.109 3897(54)	10^{-31} kg	0.59
		5.485 799 03(13)	10^{-4} u	0.023
in electron volts, $m_e c^2/\{e\}$		0.510 999 06(15)	MeV	0.30
electron–muon mass ratio	m_e/m_μ	4.836 332 18(71)	10^{-3}	0.15
electron–proton mass ratio	m_e/m_p	5.446 170 13(11)	10^{-4}	0.020
electron–deuteron mass ratio	m_e/m_d	2.724 437 07(6)	10^{-4}	0.020
electron–α-particle mass ratio	m_e/m_α	1.370 933 54(3)	10^{-4}	0.021
electron specific charge	$-e/m_e$	−1.758 819 62(53)	$10^{11}\ \mathrm{C\,kg^{-1}}$	0.30
electron molar mass	$M(\mathrm{e}), M_e$	5.485 799 03(13)	10^{-7} kg/mol	0.023
Compton wavelength, $h/m_e c$	$\lambda_{\rm C}$	2.426 310 58(22)	10^{-12} m	0.089
$\lambda_{\rm C}/2\pi = \alpha a_0 = \alpha^2/4\pi R_\infty$	$\bar{\lambda}_{\rm C}$	3.86 159 323(35)	10^{-13} m	0.089
classical electron radius, $\alpha^2 a_0$	r_e	2.817 940 92(38)	10^{-15} m	0.13
Thomson cross section, $(8\pi/3)r_e^2$	σ_e	0.665 246 16(18)	$10^{-28}\ \mathrm{m^2}$	0.27
electron magnetic moment	μ_e	928.477 01(31)	$10^{-26}\ \mathrm{J\,T^{-1}}$	0.34
in Bohr magnetons	$\mu_e/\mu_{\rm B}$	1.001 159 652 193(10)		1×10^{-5}
in nuclear magnetons	$\mu_e/\mu_{\rm N}$	1838.282 000(37)		0.020
electron magnetic moment anomaly, $\mu_e/\mu_{\rm B} - 1$	a_e	1.159 652 193(10)	10^{-3}	0.0086
electron g-factor, $2(1+a_e)$	g_e	2.002 319 304 386(20)		1×10^{-5}
electron–muon magnetic moment ratio	μ_e/μ_μ	206.766967(30)		0.15
electron–proton magnetic moment ratio	μ_e/μ_p	658.210 6881(66)		0.010
Muon				
muon mass	m_μ	1.883 5327(11)	10^{-28} kg	0.61
		0.113 428 913(17)	u	0.15
in electron volts, $m_\mu c^2/\{e\}$		105.658 389(34)	MeV	0.32
muon–electron mass ratio	m_μ/m_e	206.768 262(30)		0.15
muon molar mass	$M(\mu), M_\mu$	1.134 289 13(17)	10^{-4} kg/mol	0.15
muon magnetic moment	μ_μ	4.490 4514(15)	$10^{-26}\ \mathrm{J\,T^{-1}}$	0.33
in Bohr magnetons,	$\mu_\mu/\mu_{\rm B}$	4.841 970 97(71)	10^{-3}	0.15
in nuclear magnetons,	$\mu_\mu/\mu_{\rm N}$	8.890 5981(13)		0.15

Table 2. The 1986 recommended values of the fundamental physical constants (continued).

Quantity	Symbol	Value	Units	Relative Uncertainty (ppm)
muon magnetic moment anomaly, $[\mu_\mu/(e\hbar/2m_\mu)]-1$	a_μ	1.165 9230(84)	10^{-3}	7.2
muon g-factor, $2(1+a_\mu)$	g_μ	2.002 331 846(17)		0.0084
muon–proton magnetic moment ratio	μ_μ/μ_p	3.183 345 47(47)		0.15
Proton				
proton mass	m_p	1.672 6231(10)	10^{-27} kg	0.59
		1.007 276 470(12)	u	0.012
in electron volts, $m_\mathrm{p}c^2/\{e\}$		938.272 31(28)	MeV	0.30
proton–electron mass ratio	$m_\mathrm{p}/m_\mathrm{e}$	1836.152 701(37)		0.020
proton–muon mass ratio	m_p/m_μ	8.880 2444(13)		0.15
proton specific charge	e/m_p	9.578 8309(29)	10^{7} C kg^{-1}	0.30
proton molar mass	$M(\mathrm{p}), M_\mathrm{p}$	1.007 276 470(12)	10^{-3} kg/mol	0.012
proton Compton wavelength, $h/m_\mathrm{p}c$	$\lambda_\mathrm{C,p}$	1.321 410 02(12)	10^{-15} m	0.089
$\lambda_\mathrm{C,p}/2\pi$	$\bar{\lambda}_\mathrm{C,p}$	2.103 089 37(19)	10^{-16} m	0.089
proton magnetic moment	μ_p	1.410 607 61(47)	10^{-26} J T^{-1}	0.34
in Bohr magnetons	$\mu_\mathrm{p}/\mu_\mathrm{B}$	1.521 032 202(15)	10^{-3}	0.010
in nuclear magnetons	$\mu_\mathrm{p}/\mu_\mathrm{N}$	2.792 847 386(63)		0.023
diamagnetic shielding correction for protons in pure water, spherical sample, 25 °C, $1-\mu_\mathrm{p}'/\mu_\mathrm{p}$	$\sigma_{\mathrm{H_2O}}$	25.689(15)	10^{-6}	–
shielded proton moment (H_2O, sph., 25 °C)	μ_p'	1.410 571 38(47)	10^{-26} J T^{-1}	0.34
in Bohr magnetons	$\mu_\mathrm{p}'/\mu_\mathrm{B}$	1.520 993 129(17)	10^{-3}	0.011
in nuclear magnetons	$\mu_\mathrm{p}'/\mu_\mathrm{N}$	2.792 775 642(64)		0.023
proton gyromagnetic ratio	γ_p	26 752.2128(81)	10^{4} s^{-1} T^{-1}	0.30
	$\gamma_\mathrm{p}/2\pi$	42.577 469(13)	MHz T^{-1}	0.30
uncorrected (H_2O, sph., 25 °C)	γ_p'	26 751.5255(81)	10^{4} s^{-1} T^{-1}	0.30
	$\gamma_\mathrm{p}'/2\pi$	42.576 375(13)	MHz T^{-1}	0.30
Neutron				
neutron mass	m_n	1.674 9286(10)	10^{-27} kg	0.59
		1.008 664 904(14)	u	0.014
in electron volts, $m_\mathrm{n}c^2/\{e\}$		939.565 63(28)	Mev	0.30
neutron–electron mass ratio	$m_\mathrm{n}/m_\mathrm{e}$	1838.683 662(40)		0.022
neutron–proton mass ratio	$m_\mathrm{n}/m_\mathrm{p}$	1.001 378 404(9)		0.009
neutron molar mass	$M(\mathrm{n}), M_\mathrm{n}$	1.008 664 904(14)	10^{-3} kg/mol	0.014
neutron Compton wavelength, $h/m_\mathrm{n}c$	$\lambda_\mathrm{C,n}$	1.319 591 10(12)	10^{-15} m	0.089
$\lambda_\mathrm{C,n}/2\pi$	$\bar{\lambda}_\mathrm{C,n}$	2.100 194 45(19)	10^{-16} m	0.089
neutron magnetic moment *	μ_n	0.966 237 07(40)	10^{-26} J T^{-1}	0.41
in Bohr magnetons	$\mu_\mathrm{n}/\mu_\mathrm{B}$	1.041 875 63(25)	10^{-3}	0.24
in nuclear magnetons	$\mu_\mathrm{n}/\mu_\mathrm{N}$	1.913 042 75(45)		0.24
neutron–electron magnetic moment ratio	$\mu_\mathrm{n}/\mu_\mathrm{e}$	1.040 668 82(25)	10^{-3}	0.24
neutron–proton magnetic moment ratio	$\mu_\mathrm{n}/\mu_\mathrm{p}$	0.684 979 34(16)		0.24

Table 2. The 1986 recommended values of the fundamental physical constants (continued).

Quantity	Symbol	Value	Units	Relative Uncertainty (ppm)
Deuteron				
deuteron mass	$m_{\rm d}$	3.343 5860(20)	10^{-27} kg	0.59
		2.013 553 214(24)	u	0.012
in electron volts, $m_{\rm d}c^2/\{e\}$		1875.613 39(57)	MeV	0.30
deuteron–electron mass ratio	$m_{\rm d}/m_{\rm e}$	3670.483 014(75)		0.020
deuteron–proton mass ratio	$m_{\rm d}/m_{\rm p}$	1.999 007 496(6)		0.003
deuteron molar mass	$M({\rm d}), M_{\rm d}$	2.013 553 214(24)	10^{-3} kg/mol	0.012
deuteron magnetic moment *	$\mu_{\rm d}$	0.433 073 75(15)	10^{-26} J T^{-1}	0.34
in Bohr magnetons,	$\mu_{\rm d}/\mu_{\rm B}$	0.466 975 4479(91)	10^{-3}	0.019
in nuclear magnetons,	$\mu_{\rm d}/\mu_{\rm N}$	0.857 438 230(24)		0.028
deuteron–electron magnetic moment ratio	$\mu_{\rm d}/\mu_{\rm e}$	0.466 434 5460(91)	10^{-3}	0.019
deuteron–proton magnetic moment ratio	$\mu_{\rm d}/\mu_{\rm p}$	0.307 012 2035(51)		0.017
PHYSICO-CHEMICAL CONSTANTS				
Avogadro constant	$N_{\rm A}, L$	6.022 1367(36)	10^{23} mol^{-1}	0.59
atomic mass constant, $\frac{1}{12}m(^{12}{\rm C})$	$m_{\rm u}$	1.660 5402(10)	10^{-27} kg	0.59
in electron volts, $m_{\rm u}c^2/\{e\}$		931.494 32(28)	MeV	0.30
Faraday constant	F	96 485.309(29)	C mol^{-1}	0.30
molar Planck constant	$N_{\rm A}h$	3.990 313 23(36)	10^{-10} J s mol^{-1}	0.089
	$N_{\rm A}hc$	0.119 626 58(11)	J m mol^{-1}	0.089
molar gas constant	R	8.314 510(70)	J mol^{-1} K^{-1}	8.4
Boltzmann constant, $R/N_{\rm A}$	k	1.380 658(12)	10^{-23} J K^{-1}	8.5
in electron volts, $k/\{e\}$		8.617 385(73)	10^{-5} eV K^{-1}	8.4
in hertz, k/h		2.083 674(18)	10^{10} Hz K^{-1}	8.4
in wavenumbers, k/hc		69.503 87(59)	m^{-1} K^{-1}	8.4
molar volume (ideal gas), RT/p				
$T = 273.15\,{\rm K}$, $p = 101\,325\,{\rm Pa}$	$V_{\rm m}$	22.414 10(19)	L/mol	8.4
Loschmidt constant, $N_{\rm A}/V_{\rm m}$	$n_{\rm o}$	2.686 763(23)	10^{25} m^{-3}	8.5
$T = 273.15\,{\rm K}$, $p = 100\,{\rm kPa}$	$V_{\rm m}$	22.711 08(19)	L/mol	8.4
Sackur-Tetrode constant (absolute entropy constant), ** $\frac{5}{2} + \ln\{(2\pi m_{\rm u}kT_1/h^2)^{\frac{3}{2}}kT_1/p_{\rm o}\}$				
$T_1 = 1$ K, $p_{\rm o} = 100$ kPa	$S_{\rm o}/R$	−1.151 693(21)		18
$p_{\rm o} = 101\,325$ Pa		−1.164 856(21)		18
Stefan–Boltzmann constant, $(\pi^2/60)k^4/\hbar^3c^2$	σ	5.670 51(19)	10^{-8} W m^{-2} K^{-4}	34
first radiation constant, $2\pi hc^2$	c_1	3.741 7749(22)	10^{-16} W m^2	0.60
second radiation constant, hc/k	c_2	0.014 387 69(12)	m K	8.4
Wien displacement law constant, $b = \lambda_{\rm max}T = c_2/4.965\,114\,23\ldots$	b	2.897 756(24)	10^{-3} m K	8.4

---

*The scalar magnitude of the neutron moment is listed here. The neutron magnetic dipole is directed oppositely to that of the proton, and corresponds to the dipole associated with a spinning negative charge distribution. The vector sum, $\mu_{\rm d} = \mu_{\rm p} + \mu_{\rm n}$, is approximately satisfied.

**The entropy of an ideal monatomic gas of relative atomic weight $A_{\rm r}$ is given by $S = S_{\rm o} + \frac{3}{2}R \ln A_{\rm r} - R \ln(p/p_{\rm o}) + \frac{5}{2}R \ln(T/{\rm K})$.

Table 3 is a list of related "maintained units and standard values," while table 4 contains a number of scientifically, technologically, and metrologically useful energy conversion factors. Finally, table 5 is an extended covariance matrix containing the variances, covariances, and correlation coefficients of the unknowns and a number of different constants (included for convenience) from which the like quantities for other constants may be readily calculated.[4] Such a matrix is necessary, of course, because the variables in a least-squares adjustment are statistically correlated. Thus, with the exception of quantities which depend only on aux-

---

[4] The variable d_{220} is omitted from table 5 because there is little need for its correlations with other quantities. Moreover, since the more significant and related quantity N_A is included (note that $N_A \sim d_{220}^{-3}$), there is no loss of information by omitting d_{220}.

Table 3. Maintained units and standard values.

A summary of "maintained" units and "standard" values and their relationship to SI units, based on a least-squares adjustment with 17 degrees of freedom. The digits in parentheses are the one-standard-deviation uncertainty in the last digits of the given value. Since the uncertainties of many of these entries are correlated, the full covariance matrix must be used in evaluating the uncertainties of quantities computed from them.

Quantity	**Symbol**	**Value**	**Units**	**Relative Uncertainty (ppm)**
electron volt, $(e/\mathrm{C})\,\mathrm{J} = \{e\}\,\mathrm{J}$	eV	1.602 177 33(49)	10^{-19} J	0.30
(unified) atomic mass unit, $1\ \mathrm{u} = m_\mathrm{u} = \frac{1}{12}m(^{12}\mathrm{C})$	u	1.660 5402(10)	10^{-27} kg	0.59
standard atmosphere	atm	101 325	Pa	(exact)
standard acceleration of gravity	g_n	9.806 65	m s^{-2}	(exact)
		'As-Maintained' Electrical Units		
BIPM maintained ohm, $\Omega_{69-\mathrm{BI}}$ $\Omega_{\mathrm{BI85}} \equiv \Omega_{69-\mathrm{BI}}(1\ \mathrm{Jan}\ 1985)$	Ω_{BI85}	$1 - 1.563(50) \times 10^{-6}$ $= 0.999\,998\,437(50)$	Ω Ω	0.050
Drift rate of $\Omega_{69-\mathrm{BI}}$	$\dfrac{d\Omega_{69-\mathrm{BI}}}{dt}$	−0.0566(15)	μΩ/a	—
BIPM maintained volt, $\mathrm{V}_{76-\mathrm{BI}} \equiv 483\,594\ \mathrm{GHz}(h/2e)$	$\mathrm{V}_{76-\mathrm{BI}}$	$1 - 7.59(30) \times 10^{-6}$ $= 0.999\,992\,41(30)$	V V	0.30
BIPM maintained ampere, $\mathrm{A}_{\mathrm{BIPM}} = \mathrm{V}_{76-\mathrm{BI}}/\Omega_{69-\mathrm{BI}}$	$\mathrm{A}_{\mathrm{BI85}}$	$1 - 6.03(30) \times 10^{-6}$ $= 0.999\,993\,97(30)$	A A	0.30
		X-Ray Standards		
Cu x-unit : $\lambda(\mathrm{CuK}\alpha_1) \equiv 1537.400\ \mathrm{xu}$	$\mathrm{xu}(\mathrm{CuK}\alpha_1)$	1.002 077 89(70)	10^{-13} m	0.70
Mo x-unit : $\lambda(\mathrm{MoK}\alpha_1) \equiv 707.831\ \mathrm{xu}$	$\mathrm{xu}(\mathrm{MoK}\alpha_1)$	1.002 099 38(45)	10^{-13} m	0.45
Å* : $\lambda(\mathrm{WK}\alpha_1) \equiv 0.209\,100\ \mathrm{Å}^*$	Å*	1.000 014 81(92)	10^{-10} m	0.92
lattice spacing of Si (in vacuum, 22.5 °C), +	a	0.543 101 96(11)	nm	0.21
$d_{220} = a/\sqrt{8}$	d_{220}	0.192 015 540(40)	nm	0.21
molar volume of Si, $M(\mathrm{Si})/\rho(\mathrm{Si}) = N_\mathrm{A} a^3/8$	$V_\mathrm{m}(\mathrm{Si})$	12.058 8179(89)	cm^3/mol	0.74

+The lattice spacing of single-crystal Si can vary by parts in 10^7 depending on the preparation process. Measurements at PTB indicate also the possibility of distortions from exact cubic symmetry of the order of 0.2 ppm.

iliary constants, the uncertainty associated with a quantity calculated from other constants in general can be found only with the use of the full covariance matrix.

To use table 5, note that the covariance between two quantities Q_k and Q_s which are functions of a common set of variables $x_i (i=1,\ldots,N)$ is given by

$$v_{ks}=\sum_{i,j=1}^{N}\frac{\partial Q_k}{\partial x_i}\frac{\partial Q_s}{\partial x_j}v_{ij} \tag{1}$$

where v_{ij} is the covariance of x_i and x_j. In this general form, the units of v_{ij} are the product of the units of x_i and x_j and the units of v_{ks} are the product of the units of Q_k and Q_s. For most cases of interest

Table 4. Energy conversion factors.

To use this table note that all entries on the same line are equal; the unit at the top of a column applies to all of the values beneath it.

Example: 1 eV=806544.10 m^{-1}

	J	**kg**	**m^{-1}**	**Hz**
1 J =	1	$1/\{c^2\}$ $1.112\,650\,06\times10^{-17}$	$1/\{hc\}$ $5.034\,1125(30)\times10^{24}$	$1/\{h\}$ $1.509\,188\,97(90)\times10^{33}$
1 kg =	$\{c^2\}$ $8.987\,551\,787\times10^{16}$	1	$\{c/h\}$ $4.524\,4347(27)\times10^{41}$	$\{c^2/h\}$ $1.356\,391\,40(81)\times10^{50}$
1 m^{-1} =	$\{hc\}$ $1.986\,4475(12)\times10^{-25}$	$\{h/c\}$ $2.210\,2209(13)\times10^{-42}$	1	$\{c\}$ 299 792 458
1 Hz =	$\{h\}$ $6.626\,0755(40)\times10^{-34}$	$\{h/c^2\}$ $7.372\,5032(44)\times10^{-51}$	$1/\{c\}$ $3.335\,640\,952\times10^{-9}$	1
1 K =	$\{k\}$ $1.380\,658(12)\times10^{-23}$	$\{k/c^2\}$ $1.536\,189(13)\times10^{-40}$	$\{k/hc\}$ 69.503 87(59)	$\{k/h\}$ $2.083\,674(18)\times10^{10}$
1 eV =	$\{e\}$ $1.602\,177\,33(49)\times10^{-19}$	$\{e/c^2\}$ $1.782\,662\,70(54)\times10^{-36}$	$\{e/hc\}$ 806 554.10(24)	$\{e/h\}$ $2.417\,988\,36(72)\times10^{14}$
1 u =	$\{m_\mathrm{u}c^2\}$ $1.492\,419\,09(88)\times10^{-10}$	$\{m_\mathrm{u}\}$ $1.660\,5402(10)\times10^{-27}$	$\{m_\mathrm{u}c/h\}$ $7.513\,005\,63(67)\times10^{14}$	$\{m_\mathrm{u}c^2/h\}$ $2.252\,342\,42(20)\times10^{23}$
1 hartree =	$\{2R_\infty hc\}$ $4.359\,7482(26)\times10^{-18}$	$\{2R_\infty h/c\}$ $4.850\,8741(29)\times10^{-35}$	$\{2R_\infty\}$ 21 947 463.067(26)	$\{2R_\infty c\}$ $6.579\,683\,8999(78)\times10^{15}$

	K	**eV**	**u**	**hartree**
1 J =	$1/\{k\}$ $7.242\,924(61)\times10^{22}$	$1/\{e\}$ $6.241\,5064(19)\times10^{18}$	$1/\{m_\mathrm{u}c^2\}$ $6.700\,5308(40)\times10^{9}$	$1/\{2R_\infty hc\}$ $2.293\,7104(14)\times10^{17}$
1 kg =	$\{c^2/k\}$ $6.509\,616(55)\times10^{39}$	$\{c^2/e\}$ $5.609\,5862(17)\times10^{35}$	$1/\{m_\mathrm{u}\}$ $6.022\,1367(36)\times10^{26}$	$\{c/2R_\infty h\}$ $2.061\,4841(12)\times10^{34}$
1 m^{-1} =	$\{hc/k\}$ 0.014 387 69(12)	$\{hc/e\}$ $1.239\,842\,44(37)\times10^{-6}$	$\{h/m_\mathrm{u}c\}$ $1.331\,025\,22(12)\times10^{-15}$	$1/\{2R_\infty\}$ $4.556\,335\,2672(54)\times10^{-8}$
1 Hz =	$\{h/k\}$ $4.799\,216(41)\times10^{-11}$	$\{h/e\}$ $4.135\,6692(12)\times10^{-15}$	$\{h/m_\mathrm{u}c^2\}$ $4.439\,822\,24(40)\times10^{-24}$	$1/\{2R_\infty c\}$ $1.519\,829\,8508(18)\times10^{-16}$
1 K =	1	$\{k/e\}$ $8.617\,385(73)\times10^{-5}$	$\{k/m_\mathrm{u}c^2\}$ $9.251\,140(78)\times10^{-14}$	$\{k/2R_\infty hc\}$ $3.166\,829(27)\times10^{-6}$
1 eV =	$\{e/k\}$ 11 604.45(10)	1	$\{e/m_\mathrm{u}c^2\}$ $1.073\,543\,85(33)\times10^{-9}$	$\{e/2R_\infty hc\}$ 0.036 749 309(11)
1 u =	$\{m_\mathrm{u}c^2/k\}$ $1.080\,9478(91)\times10^{13}$	$\{m_\mathrm{u}c^2/e\}$ $931.494\,32(28)\times10^{6}$	1	$\{m_\mathrm{u}c/2R_\infty h\}$ $3.423\,177\,25(31)\times10^{7}$
1 hartree =	$\{2R_\infty hc/k\}$ $3.157\,733(27)\times10^{5}$	$\{2R_\infty hc/e\}$ 27.211 3961(81)	$\{2R_\infty h/m_\mathrm{u}c\}$ $2.921\,262\,69(26)\times10^{-8}$	1

Table 5. Expanded covariance and correlation coefficient matrix for the 1986 recommended set of fundamental physical constants.

The elements of the covariance matrix appear on and above the major diagonal in (parts in 10^9)^2; correlation coefficients appear in *italics* below the diagonal. The values are given to as many as six digits only as a matter of consistency.

The correlation coefficient between m_e and N_A appears as −1.000 in this table because the auxiliary constants were considered to be exact in carrying out the least-squares adjustment. When the uncertainties of m_p/m_e and M_p are properly taken into account, the correlation coefficient is −0.999 and the variances of m_e and N_A are slightly increased.

	α^{-1}	K_V	K_Ω	μ_μ/μ_p	e	h	m_e	N_A	F
α^{-1}	1997	−1062	925	3267	−3059	−4121	−127	127	−2932
K_V	*−0.080*	87988	90	−1737	89050	177038	174914	−174914	−85864
K_Ω	*0.416*	*0.006*	2477	1513	−835	−744	1105	−1105	−1939
μ_μ/μ_p	*0.498*	*−0.040*	*0.207*	21523	−5004	−6742	−208	208	−4796
e	*−0.226*	*0.989*	*−0.055*	*−0.112*	92109	181159	175042	−175042	−82933
h	*−0.154*	*0.997*	*−0.025*	*−0.077*	*0.997*	358197	349956	−349956	−168797
m_e	*−0.005*	*0.997*	*0.038*	*−0.002*	*0.975*	*0.989*	349702	−349702	−174660
N_A	*0.005*	*−0.997*	*−0.038*	*0.002*	*−0.975*	*−0.989*	*−1.000*	349702	174660
F	*−0.217*	*−0.956*	*−0.129*	*−0.108*	*−0.902*	*−0.931*	*−0.975*	*0.975*	91727

involving the fundamental constants, the variables x_i may be taken to be the fractional change in the physical quantity from some fiducial value, and the quantities Q can be expressed as powers of physical constants Z_j according to

$$Q_k=q\prod_{j=1}^{N} Z_j^{Y_{kj}}, \tag{2}$$

where q is a numerical factor. If the variances and covariances are then expressed in relative units, eq (1) becomes

$$v_{ks}=\sum_{i,j=1}^{N} Y_{ki}Y_{sj}v_{ij}, \tag{3}$$

where the v_{ij} are to be expressed, for example, in (parts in 10^9)^2. Equation (3) is the basis for the expansion of the covariance matrix to include e, h, m_e, N_A, and F.

In terms of correlation coefficients defined by $r_{ij}\equiv v_{ij}(v_{ii}v_{jj})^{-1/2}\equiv v_{ij}/\epsilon_i\epsilon_j$, where ϵ_i is the standard deviation ($\epsilon_i^2=v_{ii}$), we may write, from eq (3),

$$\epsilon_k^2=\sum_{i=1}^{N} Y_{ki}^2\epsilon_i^2+2\sum_{j<i}^{N} Y_{ki}Y_{kj}r_{ij}\epsilon_i\epsilon_j, \tag{4}$$

where the standard deviations are to be expressed in relative units.

As an example of the use of table 5, consider the calculation of the uncertainty of the Bohr magneton $\mu_B=e\hbar/2m_e$ ($\hbar=h/2\pi$). In terms of the variables of the 1986 adjustment this ratio is given by

$$\mu_B=[2\pi\mu_0R_\infty\, E]^{-1}(\alpha^{-1})^{-3}K_V, \tag{5}$$

where the quantities in brackets are auxiliary constants taken to be exact. Using eq (3) and letting α^{-1} correspond to $i=1$ and K_V to $i=2$ gives[5]

$$\epsilon_{\mu_B}^2=Y_1^2\,v_{11}+2Y_1Y_2v_{12}+Y_2^2v_{22}. \tag{6}$$

Comparing eq (5) with eq (2) yields $Y_1=-3$ and $Y_2=1$. Thus eq (6) and table 5 lead to

$$\epsilon_{\mu_B}^2=[9\,(1997)-6(-1062)+1(87988)]\times(10^{-9})^2 \tag{7}$$

or $\epsilon_{\mu_B}=0.335$ ppm. An alternate approach is to evaluate $e\hbar/2m_e$ directly from table 5; then e corresponds to $i=5$, h to $i=6$, and m_e to $i=7$ with $Y_5=Y_6=1$ and $Y_7=-1$. Then

$$\epsilon_{\mu_B}^2=Y_5^2v_{55}+2Y_5Y_6v_{56}+Y_6^2v_{66}$$

$$+2Y_5Y_7v_{57}+2Y_6Y_7v_{67}+Y_7^2v_{77} \tag{8a}$$

$$=[1(92109)+2(181159)+1(358197)$$

$$-2(175042)-2(349956)$$

$$+1(349702)]\times(10^{-9})^2 \tag{8b}$$

which also yields $\epsilon_{\mu_B}=0.335$ ppm.

---

[5] Note that in using eq (3), we set $s=k$, $\epsilon_k^2=v_{kk}$, suppress k as a subscript on Y, and replace k with μ_B.

References

[1] Cohen, E. R., and B. N. Taylor, The 1986 Adjustment of the Fundamental Physical Constants, a Report of the CODATA Task Group on Fundamental Constants, CODATA Bulletin 63, Pergamon Press: Maxwell House, Fairview Park, Elmsford, NY, 10523, or Headington Hill Hall, Oxford OX3 OBW, U.K. (November, 1986).

[2] Recommended Consistent Values of the Fundamental Physical Constants, 1973, a Report of the CODATA Task Group on Fundamental Constants, CODATA Bulletin 11, CODATA Secretariat, 51 Blvd. de Monmorency, 75016 Paris, France (August, 1973).

[3] Cohen, E. R., and B. N. Taylor, J. Phys. Chem. Ref. Data 2 663 (1973).

[4] Taylor, B. N.; W. H. Parker and D. N. Langenberg, Rev. Mod. Phys. **41** 375 (1969); also published as The Fundamental Constants and Quantum Electrodynamics, Academic Press: New York (1969).

[5] Cohen, E. R., and J. W. M. DuMond, Rev. Mod. Phys. **37** 537 (1965).

[6] Com. Intl. Poids Mes. Com. Consult. d'Electricité, Trav. 13^e Session (Bur. Intl. Poids Mes., Sèvres, France, Oct. 1972), p. E 13; Terrien, J., Metrologia **9** 40 (1973).

[7] P. V. Séances Com. Intl. Poids Mes., 61^e Session, **40** (Bur. Intl. Poids Mes., Sèvres, France, Oct. 1972), pp. 22, 100.

[8] Taylor, B. N., J. Res. Natl. Bur. Stand. **91** 299 (1986).

[9] Taylor, B. N., J. Res. Natl. Bur. Stand. **92** 55 (1987).

Journal of Research of the National Bureau of Standards

Far Ultraviolet Detector Standards

Volume 92 Number 2 March–April 1987

L. Randall Canfield,
Nils Swanson

National Bureau of Standards
Gaithersburg, MD 20899

A description is given of the NBS program in which special photodiodes for the far ultraviolet spectral region (5–254 nm) are made available as transfer standards. These detectors are calibrated in terms of quantum efficiency (photoelectrons per incident photon) as a function of wavelength. Descriptions are also given of the calibration principles, calibration systems, and photodiode types involved in this program. Calibrations reference to the photoionization of rare gases.

Key words: calibration; detectors; far ultraviolet; photodiodes; photoionization; quantum efficiency.

Accepted: November 28, 1986

1. Introduction

During the period 1955–1965 there occurred a rapid increase in interest in scientific activity in the far ultraviolet, primarily due to two developments. First, advances in both vacuum and optical technology had led to the development and manufacture of convenient instruments (spectrographs, monochromators, etc.) with which many new experiments could be successfully conducted in the far ultraviolet. Second, the accomplishment of operating spacecraft had provided the opportunity to pursue solar and astronomical studies beyond the absorption of the earth's atmosphere, hence into the far ultraviolet. With the great increase in far ultraviolet activity came the parallel need for radiometric capability in this region. The situation became rather obvious when it developed that experiments orbiting on different spacecraft, but observing the same phenomena, were recording vastly differing flux levels. Clearly a common, accurate radiometric base was needed and NBS undertook the establishment of a program which would lead to transfer standard detectors for the far ultraviolet.

The far ultraviolet detector radiometry program attempts to furnish transfer standards capable of determining absolute flux levels in the spectral range 5–254 nm. These standards should be relatively stable, simple to use, and within the typical laboratory budget. Calibrations furnished with these standards should be state-of-the-art in accuracy. Improvements in accuracy and stability should be constantly sought and incorporated when possible.

Two detector types (described in section 2) are now available from NBS as calibrated transfer standards covering the spectral regions 5–122 nm (probable errors 8–15%) and 116–254 nm (probable errors 6–10%). Users are furnished with the quan-

About the Authors: L. Randall Canfield and Nils Swanson are physicists in the Radiation Physics Division in NBS' National Measurement Laboratory. The work they describe will be more fully treated in the forthcoming NBS Special Publication 250–2.

tum efficiency of their detector as a function of wavelength (with quantum efficiency defined as the number of photoelectrons per incident photon).

Additionally, special detectors which do not lend themselves to convenient on-site cross-calibration may be calibrated at NBS if the detectors merit radiometric application and if the NBS facilities are suitable for the particular device.

It is hoped that eventually all far ultraviolet detector calibration activities can be conducted at the NBS Synchrotron Ultraviolet Radiation Facility (SURF-II), using its calculable flux as the radiometric base. This would eliminate the weakest link in the calibration chain, the thermopile, and might also lead to the elimination of the need for working standards. Even before this is achieved there are several areas in which improvements may be made. Materials studies may lead to windowless detectors with better spatial uniformity, temporal stability and improved quantum efficiencies. It is hoped that the short wavelength limit of calibrations can be extended and that the uncertainties of calibrations at all wavelengths can be reduced.

2. Description of Detector Types

2.1 The NBS Windowless Photodiode (5–122 nm)

The NBS windowless photodiode transfer standard detector is the result of temporal stability and spatial uniformity studies which were conducted at NBS in the 1960's on several likely choices for a photocathode material suitable for use in an open vacuum photodiode [1].[1] The spectral region of interest was primarily at wavelengths shorter than the transmission limit of magnesium fluoride, so as to extend the range covered by sealed photodiodes.

2.1.1 Photocathode Material. The material of choice for the photocathode was and is aluminum with the natural oxide thickness artificially increased. Vacuum deposited aluminum (99.999% pure) samples on quartz substrates are anodized to increase the natural oxide thickness for use as photocathodes in NBS far UV windowless transfer standard photodiodes. The increased oxide (~15 nm thick) improves the stability of the photoyield over that of the deposited aluminum by preventing any further oxide development, and achieves more complete absorption of the incoming radiation, thus reducing wavelength-dependent variations in the photoyield caused by optical interference. (The aluminum has a very low coefficient of absorption in much of the spectral range and hence acts like a transparent film bounded on each surface by an absorbing film.) A description of the method used to accomplish this follows.

The anodizing method used has been described in the literature [2]. A pH 5.5 bath of tartaric acid is used with a 99.999% purity aluminum cathode. The bath is prepared by dissolving 3% (by weight) powdered tartaric acid in distilled water. The pH is measured and adjusted by the addition of small amounts of either extra tartaric acid or ammonium hydroxide, depending on whether more or less acidity is needed.

A simple teflon fixture holds the sample in contact with a pure aluminum wire at the edge of the circular substrate, so that most of the sample may be lowered into the bath without wetting the contact point. Electrical connection is made to this wire (+) and to the cathode wire (−) from a well-regulated power supply which has been preset to 10.5 V and current-limited to about 10 mA.

2.1.2 Photodiode Assembly. Figure 1 shows the configuration of this photodiode. A cylindrical anode is suspended very near the cathode, with a machined teflon component providing support for both. The photocathode is electrically connected to a machined piece of aluminum on the opposite side of the substrate by aluminum foil. Provision for physical location of the whole device is made by a threaded hole in the rear of the machined aluminum piece. This mounting is at cathode potential and must be well insulated from ground. The entire device is intended for use in vacuum.

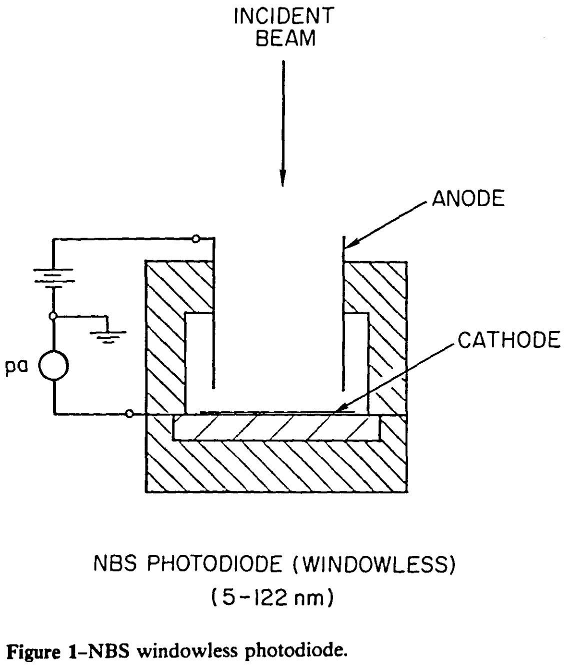

Figure 1–NBS windowless photodiode.

---

[1] Figures in brackets indicate literature references.

2.1.3 Operating Characteristics. Incident far UV photons cause the photocathode to emit low-energy electrons, which are accelerated away by the electric field established by the anode potential of 60–100 V. The rate of emission is measured with a suitable calibrated picoammeter. The usable range of photocurrents is roughly from 10^{-9} to less than 10^{-15} amperes. (The "dark" current—mostly thermionic emission—is known to be less than 10^{-15} amperes, but has not been measured.) From a table of quantum efficiencies (electrons per incident photon) given in the NBS Report of Test which accompanies each photodiode, the flux rate at the surface of the photocathode may be derived. Typical efficiencies range from a few percent at 5 nm to a peak value of about 20 percent in the 60–70 nm region, then back down to about 1 percent at 122 nm (see fig. 2). The photocathode surface, being unprotected from outside contamination, may change in efficiency due to such exposure, so it is important that potential sources of contamination be recognized and controlled. One should also ensure that the photocathode is protected from charged particles during operation, since any such particles arriving at the photocathode would result in an incorrect assessment of the radiant flux.

2.2 Windowed Photodiode (116–254 nm)

During the history of the NBS far ultraviolet transfer standard detector program several suppliers of windowed detectors have been used. Initially satisfactory photodiodes were obtained from the Stanford Electronics Laboratory at Stanford University and from EMR Photoelectric in New Jersey,[2] but in recent years both of these sources have ceased production of devices made to NBS specifications. We now obtain windowed photodiodes from the Electronic Vision & Systems Division (EVSD) of Science Applications International Corporation, which acquired the necessary competence as a result of a NASA contract to fabricate Digicon detectors for use in spacecraft.

2.2.1 Physical Characteristics. The photodiode supplied by EVSD (fig. 3) is known as their Model 54-0-000 and utilizes a semi-transparent cesium telluride photocathode deposited on the inner surface of a magnesium fluoride window. The device is fabricated in ultra-high vacuum with the photocathode being formed remote from the photodiode body, and the window/photocathode joined to the body by an indium alloy seal in the same vacuum. The body is made of OFHC copper electrodes brazed to ceramic spacers, with the center electrode isolating the cathode from anode leakage, and the rear electrode serving as the anode.

2.2.2 Operating Characteristics. A supply of 150 V is attached to the anode and a calibrated picoammeter measures cathode photocurrent (fig. 3). The center electrode is normally grounded. Maximum photocurrent should be kept at less than 10^{-8} amperes and the magnesium fluoride window must be maintained free of contamination. Fre-

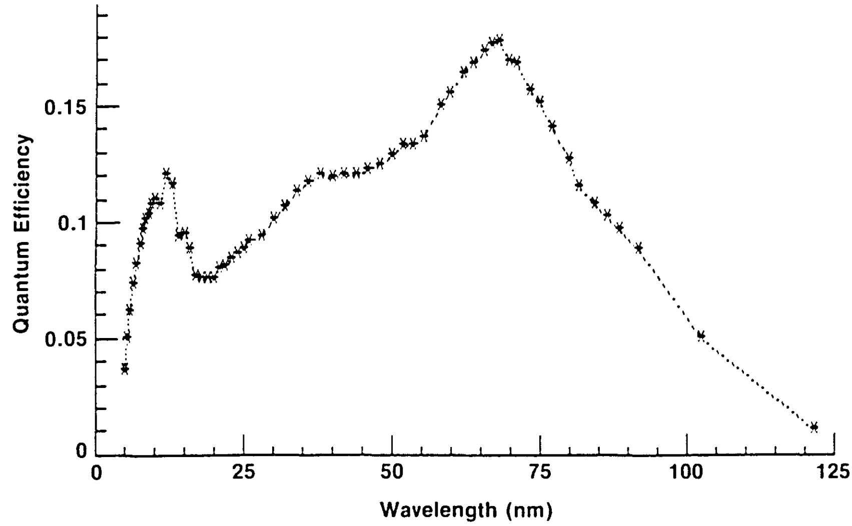

Figure 2-Typical quantum efficiency of NBS windowless photodiodes.

---

[2] Commercial products--materials and instruments--are identified in this document for the sole purpose of adequately describing experimental or test procedures. In no event does such identification imply recommendation or endorsement by the National Bureau of Standards of a particular product; nor does it imply that a named material or instrument is necessarily the best available for the purpose it serves.

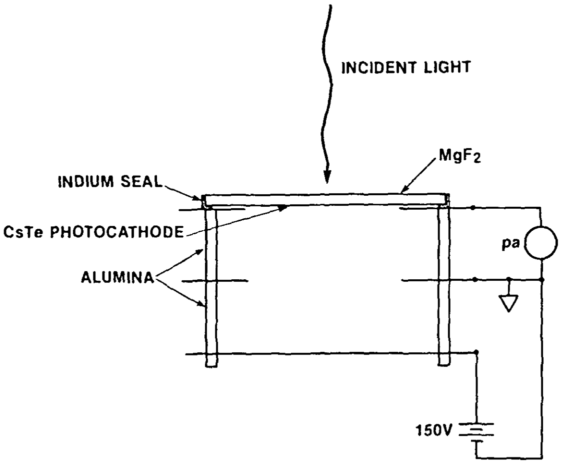

Figure 3-Schematic and wiring configuration of EVSD photodiode.

quent cleaning of the window may also degrade its transmittance, and should be avoided as a routine measure.

2.3 Rare Gas Ionization Chamber

The absolute detector which forms the basis for all present far ultraviolet detector calibrations at NBS is the rare gas ionization chamber. The basic operational principles and demonstration of the absolute nature of this detector have been discussed in the literature [3-5]. The design used at NBS (seen in fig. 4) has two 10.16 cm ion collector plates with a shorter guard plate at the rear to prevent field fringing in the ion collection region. The chamber which is used at wavelengths shorter than 58 nm has the anode extended to very near the ion collectors to reduce the field acting on electrons resulting from ionization events [4]. Direct calibrations of photodiodes are possible from 5-92 nm.

2.4 Thermopile

A windowless thermopile (see section 4) is used to transfer the capability of absolute detection by the ionization chamber to longer wavelengths. (In the region >100 nm the photon energy is insufficient to ionize any practical rare gas.) The thermopile employed is an extended junction, windowless device which uses very thin gold leaves coated with thin gold black to form a detecting area which is effectively much larger than the actual thermocouples. Such a detector is in no way absolute and must be calibrated by reference to an absolute detector, in our case, the rare gas ionization chamber. Detection of relatively weak UV energy with a thermal detector is extremely difficult, and to achieve reasonable signal-to-noise it is nec-

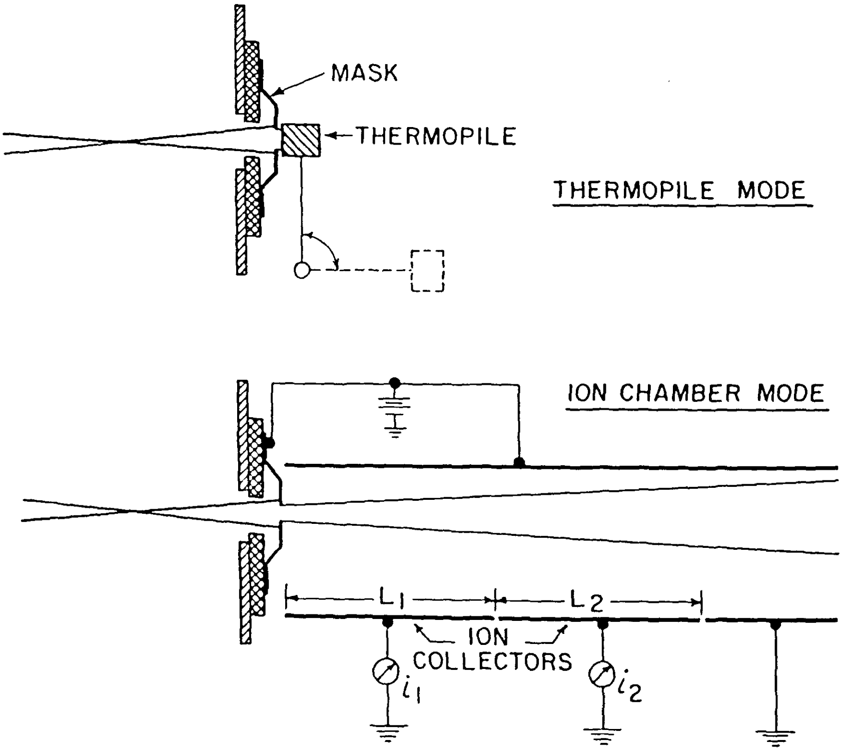

Figure 4-Configuration of thermopile and ionization chamber detectors.

essary to use ac phase-locked techniques. Further discussion of this application of a thermopile detector is given in section 4.

3. Calibration Techniques

Although the exact calibration procedures differ in various portions of the spectral region covered, in all cases the absolute reference standard is the rare gas ionization chamber [3,4]. At wavelengths at which the photon energy is sufficient to ionize a rare gas, calibration of a photodiode can be accomplished directly; otherwise a windowless thermopile is used to transfer the calibration in wavelength. The mathematical treatment of the absolute calibrations follows.

3.1 Calibration Principles

3.1.1 Ionization Chamber (long wavelengths). The use of the rare gas ionization chamber in the 50–92 nm region is fairly straightforward, since the light source and grating used in this region preclude the existence of second or higher orders from the grating, and the photon energies are insufficient to ionize the appropriate rare gas more than singly and the electrons resulting from ionization events have insufficient energy to cause secondary ionization of the gas. The so-called double ionization chamber is used exclusively in this region, obviating the need for pressure and temperature measurements, or knowledge of the cross section of the gas.

The theory is treated in reference [3]. The fundamental equation from which the radiant flux may be calculated is:

$$I=\frac{i_1^2}{e(i_1-i_2)} \tag{1}$$

where

	example
i_1=ion current (plate 1)	1×10^{-10} A (C/s)
i_2=ion current (plate 2)	1×10^{-11} A
e=the electronic charge	1.6×10^{-19} C
I=radiant flux entering chamber	6.944×10^{8} photons/s

The numbers shown at the right are examples of a "typical" hypothetical case.

3.1.1.1 Direct Calibration of Photodiodes. If a windowless photodiode is being calibrated directly by use of the ionization chamber, the relationship

$$E=\frac{i_D}{eIk} \tag{2}$$

where

i_D=the emissive photocurrent from the photodiode
I=the radiant flux incident on the photocathode
E=the quantum efficiency (electrons/photon) of the photodiode
k=the correction for monochromator gas absorption (in the ionization chamber mode)

may be used to determine the quantum efficiency. Combining eqs (1) and (2) gives:

$$E=\frac{i_D(i_1-i_2)}{i_1^2\,k}. \tag{3}$$

(In principle, if the currents from both the ionization chamber plates and the photodiode are measured with the same picoammeter using the same feedback resistors, absolute calibration of the picoammeter is not required.)

3.1.1.2 Calibration of Thermopile. There is no need to obtain an absolute thermopile calibration if the response of thermopile to incident radiant flux can be determined relative to a stable reference. Such a reference, a mercury battery, is used to do this, enabling easy relative calibration of the ac thermopile system with the dc ionization chamber.

The general relationship describing the calibration of the thermopile, which is easily derived is:

$$I=\frac{i_1^2}{e(i_1-i_2)}=\frac{F\,R\,l\,\lambda}{k} \quad \text{so } F=\frac{k\,i_1^2}{R\,l\,\lambda\,e(i_1-i_2)} \tag{4}$$

where

l=thermopile photoelectric correction
I=radiant flux incident on thermopile or ion chamber (photons/s)
F=thermopile calibration factor
λ=wavelength (A) (to normalize irradiance)
R=ratio of thermopile signal to test signal

The subsequent calibration of a photodiode using the thermopile is given by:

$$I'=\frac{i_D}{eE}=F\,R'\,l\,\lambda \quad \text{so } E=\frac{i_D}{e\,F\,R'\,l\,\lambda}. \tag{5}$$

(Here "I" and "R" have the same meaning as above, but are different values, since the thermopile and photodiode calibrations are done separately.)

3.1.2 Ionization Chamber (short wavelengths). The use of the rare gas ionization chamber in this region is complicated by the fact that photon energies are high enough to create both multiple ionization (more than one ion-electron pair per event) and secondary ionization from electrons with sufficient energy to ionize the gas. There is also an unrelated complication which the double ionization chamber helps to deal with: high order impurity in the diffracted light from the gratings used. Reference [10] describes a method for using the double ionization chamber to determine the fraction of the incident light which is first order. Since the range of photon energies used and the distribution of the continuum of SURF-II are now different from those described in the reference, the technique must be somewhat different.

In order to proceed, certain assumptions must be made. It is assumed that if there are high order impurities, they are only second order. It is also assumed that there exists a portion of the region in which there is only first order (appropriate choices of filters and machine energies can ensure this and the first assumption).

In regions where the fraction of first order is expected to be less than 1, determination of the inci dent radiant flux (normalized by use of a monitor) is made with both high and low pressure ion chamber measurements. The current from each of two equal length ion collector plates is measured independently in the high pressure mode (the ratio of currents will be seen to be needed); pressure and temperature data are measured in both modes. Two low pressure measurements are made at about 0.010 and 0.020 Torr presure and the normalization is extrapolated to zero pressure to eliminate any effects of secondary ionization (which cannot occur at zero pressure). The relationship which describes the amount of secondary ionization present during the high pressure measurement is then:

$$C=\frac{I_H}{I_L} \tag{6}$$

where

C = secondary ionization coefficient
I_L = radiant flux entering the chamber (zero pressure)
I_H = radiant flux entering the chamber (high pressure)

In either pressure mode the flux is calculated from:

$$I=\frac{i}{e(1-\exp[-\mu\, kg])} \tag{7}$$

where

i = total ion current
p = pressure
T = temperature (C)
μ = gas absorption coefficient (per cm)
$kg=\frac{273.16}{(T+273.16)}\cdot\frac{p}{760}$.

To determine the fraction of first order "f" at a given wavelength, the above values of "C" are used with the data from the two ion collector plates (high pressure) in the relationship:

$$f=\frac{m_2(1-\tau b)}{\tau(m_1 a-m_2 b)+m_2-m_1} \tag{8}$$

where

a = exponential term at T, P for primary wavelength
b = exponential term at T, P for half wavelength
c_1 = secondary ionization correction coefficient at primary wavelength
c_2 = secondary ionization correction coefficient at half wavelength
$m_1=C_1(1-a)$
$m_2=C_2(1-b)$
$\tau=\frac{i_1}{i_2}$

Only low pressure ionization chamber data are used to determine photodiode quantum efficiencies in the 5–50 nm region. The equations describing the contributions to total ion current are:

$$\text{ion current from 1st order } \bar{i}_1=\frac{fQ_1\, i}{Q_2K_2(1-f)+fQ_1K_1} \tag{9}$$

$$\text{ion current for 2nd order } \bar{i}_2=\frac{i-\bar{i}_1 K_1}{K_2} \tag{10}$$

where

f = fraction of total flux which is first order
Q_1 = absorption term for 1st order
Q_2 = absorption term for 2nd order
K_1, K_2 = multiple ionization corrections for 1st and 2nd orders

The relationships for the general case in which the fraction of first order (f) is less than 1 are:

$$\text{Radiant flux at primary wavelength: } I_1=\frac{\bar{i}_1}{e\,Q_1} \tag{11}$$

Radiant flux at half wavelength: $I_2 = \frac{\bar{i}_2}{e\,Q_2}$ (12)

The above calculations are used, with a prior measurement of the quantum efficiency at the half wavelength (where $f=1$) to arrive at the efficiency at the primary wavelength:

QE at primary wavelength $E_1 = \frac{i_D - E_2\,e\,I_2}{e\,I_1}$ (13)

where

i_D=measured photodiode current
$E_2=QE$ at half wavelength
I_1=radiant flux at primary wavelength
I_2=radiant flux at half wavelength

3.2 Measurement Methods

3.2.1 5–50 nm Region. Calibrations in this region are done at the NBS SURF-II facility, which is described in detail in section 4.1. The basic technique is to use the photoionization of a rare gas to calibrate a photodiode which can intercept the incoming light before it passes through a thin foil (preventing the ion chamber gas from flowing into the storage ring) into the ionization chamber. The calibration of the monitor photodiode is transferred to a working standard which is then used to calibrate outgoing photodiodes by intercomparison.

The calibration of the monitor photodiode is in terms of response per unit flux passing through the ionization chamber foil (as a function of wavelength). (It is, of course, impossible to operate a photodiode in the presence of ionization chamber gas.) The calibration of the monitor photodiode must be transferred to a working standard which is illuminated through the same foil(s) that were used during ionization chamber measurements.

3.2.2 50–122 nm Region. In this region calibrations are done using a measurement system incorporating a normal incidence monochromator and a duoplasmatron light source. This system is described in detail in section 4.3. Absolute calibrations of a working standard windowless photodiode are done by direct interchange with a rare gas ionization chamber in the region 50–92 nm. Two additional wavelengths, 102.6 nm and 121.6 nm cannot be done using the ionization chamber directly, so the thermopile technique described in the next section is applied directly to a working standard at 102.6 nm, and the 121.6 nm point is obtained from intercomparison with a windowed standard. It is not necessary to correct for any of the sources of spurious ionization chamber data described in section 3.1 since the photon energy is always less than twice the ionization potential and there is no possibility of second order contamination in the exit beam (due to the use of a line source and a monochromator grating with very low efficiency at wavelengths below 50 nm). After a working standard has been calibrated, it may be used to calibrate outgoing photodiodes by direct intercomparison.

3.2.3 116–254 nm Region. Calibrations in this region require the use of a thermopile to transfer the calibration from the ionization chamber (which cannot be used at wavelengths longer than 102 nm) to windowed photodiodes (which cannot be used at wavelengths shorter than 113 nm). Early studies proved that the appropriate thermopile appears to have the same sensitivity (probable error 3%) throughout the spectral region 58–92 nm [5,6]. Therefore it is proper to calibrate such a thermopile at ionization chamber wavelengths (several should give equal sensitivity), and then use the calibrated thermopile to calibrate a photodiode at longer wavelengths. This basic procedure is described in detail in section 4.2.

As an additional check on the thermopile-derived results, a low pressure Hg arc filtered lamp is used to determine the quantum efficiency of photodiodes. This lamp was calibrated by the Radiometric Physics Division of NBS by techniques traceable to blackbody radiometry, and is used as a single wavelength (253.7 nm) irradiance source, with the irradiance specified at 2 m distance from the source. Two such calibrated lamps are available

Outgoing calibrations of photodiodes are accomplished by intercomparison of known and unknown, measuring the ratio of photocurrents in a constant intensity monochromatic beam from the monochromator mentioned in section 4.2.

4. Calibration Systems

4.1 SURF-II Detector Calibration System (5–50 nm)

4.1.1 History. The capability of calibrating transfer standard photodiodes at wavelengths requiring grazing incidence optics was established at NBS in the mid-1970's making use of the SURF-II electron storage ring synchrotron radiation facility. This facility served as an extension to shorter wavelengths of the program which was already in place, in which both windowless and windowed transfer standards were made available to interested users. In both facilities the absolute reference detector was a rare gas ionization chamber.

Initially the SURF-II facility was used at wavelengths from about 20–50 nm [6]; eventually the range was extended to 5 nm. The transfer standards that were calibrated and issued were exclusively of the windowless NBS design, but on occasions the SURF-II facility was used to calibrate other special detectors for special needs of users [8,9].

In 1983 the existing facility was dismantled to make way for an incoming experiment, and the construction of a new apparatus was begun. A new, dual toroidal grating monochromator optimized for the 3–60 nm region was designed and constructed, as were the toroidal gratings for it. Also designed was a new experimental system incorporating the experiences of the original SURF-II detector facility. The new system was to provide greater flux levels at the experiment, coverage to shorter wavelengths, more accurate results, and faster throughput of calibrations.

4.1.2 Experiment. The basic configuration of the experimental system is shown schematically in figure 5. A pneumatic gate valve isolates the calibration facility from the storage ring. The central portion of this valve is fitted with a window to allow transmission of visible light in the closed position as an aid in system alignment. A pneumatically actuated shutter intercepts the incoming beam, and manually adjustable vertical and horizontal masks limit the illumination of the monochromator grating as appropriate.

4.1.2.1 Monochromator. A sine bar drive monochromator with two interchangeable toroidal gratings is used. Dispersion is in the vertical plane, with the center 2 meters from the electron orbit tangent point. The angle of incidence at zero order is 83.5 degrees. The ruled gold gratings may be interchanged manually from outside the vacuum housing. At the shortest wavelengths (3–20 nm) a 1200 line/mm grating is used; a 300 line/mm grating is used at longer wavelengths. The spectral scanning range of the monochromator is from slightly below 0 to 20 nm (1200/mm grating) and ultimate resolution is .02 nm. The image of the electron beam is focused on an axially adjustable exit slit, with interchangeable prealigned slits available. A small pneumatic gate valve isolates the monochromator from the experimental chamber portion of the system.

4.1.2.2 Foil Chamber. A bellows couples the monochromator assembly to the balance of the system, with a 4 mm diameter capillary limiting gas flow toward the monochromator. Radiation emerging from the capillary may be intercepted by a windowless monitor photodiode (of the same type that is ordinarily calibrated) with interchangeable polypropylene or aluminum filters. This assembly (not shown in fig. 5) provides the intensity level reference for all calibration activities via photocurrent from the photodiode.

4.1.2.3 Ion Chamber. When the monitor detector and filter are not in the beam, radiation falls into the rare gas ion chamber through one of two manually interchangeable filters (as above) which also serve as gas seals during ion chamber activities, when the gas pressure may be as high as 2 Torr. These filters may be interchanged from outside the vacuum system. When non-ion chamber measurements are in progress, the chamber plates remain in place and have, in the absence of interacting rare gas molecules, no effect on the radiation beam.

4.1.2.4 Intercomparison Module. At the rear of the apparatus is an easily removable flange containing an internal mounting wheel for six photodiodes which may be used to make intercomparison measurements. Electrical contact to the photocathode

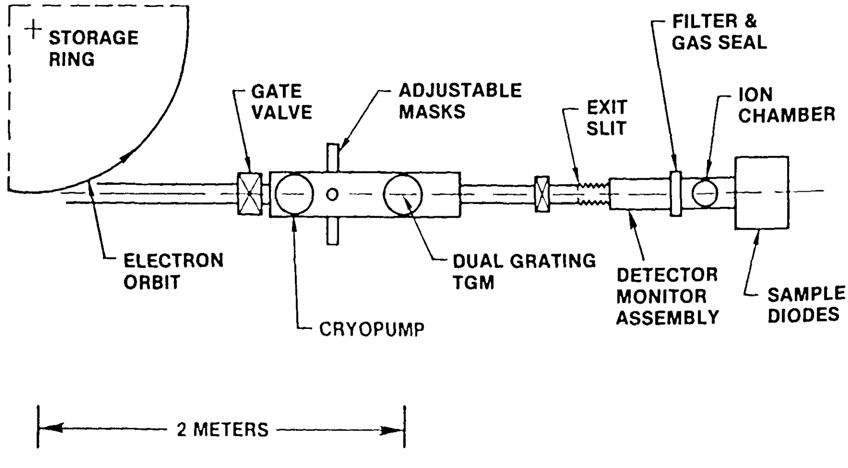

Figure 5-Schematic of Far Ultraviolet Detector Calibration Facility at SURF-II.

in the beam is made by an external pneumatic actuator, allowing photocurrent from this detector to be measured.

4.1.2.5 Data Acquisition. A Digital Equipment LSI-11/23 computer and CAMAC interface modules accomplish most data acquisition activities remotely from the SURF-II control room. Stepping motors control both the wavelength drive and diode intercomparison wheel rotation, with encoders monitoring shaft positions. Pneumatic actuators control the shutter, monitor detector and filter positions, and photocathode contact at the intercomparison wheel. Status switches monitor the positions of shutter, monitor detector and filter, gas seal filters, and photocathode actuator. The SURF beam current monitor line is connected to enable integration periods to be normalized regardless of beam intensity level. Incoming data from either emissive photocurrent or ion current are converted to pulses whose frequency is proportional to the current intensity. The pulses are then counted for the period determined by reference to the house beam monitor. Three electrometers are used, with each calibrated daily using a standard current source.

The concept of system operation is that the monitor diode package (diode + filter) monitors the beam intensity and provides a reference for all ion chamber measurements. In other words, the package response is related to the radiation passing through the ion chamber filter. However, when the calibration of the package is transferred to a diode on the rear wheel, the same filter is in the beam, so it is thus possible to have knowledge of the magnitude of radiation reaching the rear detector, and to arrive at an absolute calibration of the detector. (The calibration of the monitor package is, of course, only relative.)

4.1.2.6 Vacuum Systems. The vacuum components associated with the SURF-II detector calibration system are shown schematically in figure 6. Pumping in the monochromator section of the apparatus is accomplished by two 110 l/s triode ion pumps, with an open cycle liquid helium cryopump over a gate valve available if needed. A nude ion gauge monitors pressure and a residual gas analyzer head is resident for SURF-II beam line acceptance studies. Beneath the foil chamber is a closed cycle cryopump with an isolation valve and ion gauge. The diode intercomparison/ion chamber region is pumped by another 110 l/s triode ion pump. Both this region and the foil chamber have ion gauges. A dedicated roughing stand consisting of carbon vane mechanical and liquid nitrogen sorption pumps is connected to the system through a valve, as is the rare gas supply system.

4.2 Thermopile System (100–320 nm)

4.2.1 Introduction. At wavelengths below 102 nm, a rare gas double ionization chamber, which will count individual absorbed photons by the ion-electron pair produced in each absorption, can be used as an absolute photon detector [3,4]. Working standard photodiodes in this wavelength range can therefore be calibrated using this ionization chamber (although they will not operate properly in the gas environment of the ionization chamber).

At wavelengths above 102 nm, the photon energy is not sufficient to ionize xenon, the rare gas

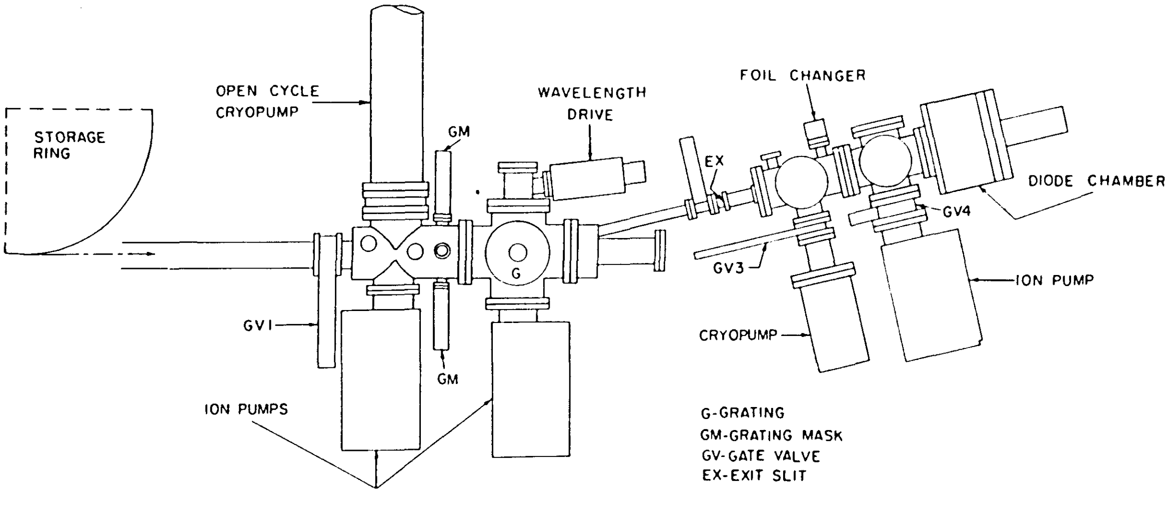

Figure 6–Detailed configuration of Far Ultraviolet Detector Facility at SURF-II.

with the lowest ionization potential (12.13 eV). In this case a method must be found for transferring the absolute calibration of the ionization chamber to the longer wavelength range. Thermal detectors measure the heating of an absorbing element in proportion to the power of the incident radiation and have a response that is generally independent of wavelength. Thus a thermal detector can be calibrated against an ionization chamber in the short wavelength range and then used in turn to calibrate a working standard photodiode in the long wavelength range.

4.2.2 Sources of Error. Thermopiles in particular have been studied as potential standards in the 100–300 nm range [5,6]. The assumption that a thermopile will develop a given voltage for a specific level of incident radiation, independent of wavelength, was tested with regard to four possible sources of error:

1) The thermopile may not absorb the same percentage of incident photons independent of wavelength.

2) The thermopile may have energy carried away by photoejected electrons.

3) The thermopile may have a wavelength-dependent time constant when ac response to chopped radiation is measured. This effect could cause wavelength-dependent variations in ac sensitivity.

4) The thermopile may have a wavelength-dependent spatial sensitivity.

Possibility 1) was checked for two typical gold blacks used on a windowless thermopile. The reflective scattering at three wavelengths in the vacuum UV was compared to that in the visible and near infrared and found to be the same within 1% of the incident intensity.

Possibility 2) was tested by measuring the thermopile signal with an electric or magnetic field either switched on to return photoejected electrons to the thermopile or switched off to let them escape. A correction curve (fig. 7) for the region 58–170 nm was derived to take account of this loss mechanism.

Possibilities 3) and 4) were tested by scanning a thermopile through a narrow beam in the far UV and visible with both dc and ac techniques. Both possibilities were found to have a negligible effect on the results.

The issue of whether such a thermopile indeed had wavelength-independent sensitivity was investigated by calibrating one both in the far UV (with a rare gas ionization chamber as an absolute detector), and in the visible/near infrared (using an NBS carbon filament lamp calibrated for total irradiance). The comparison agreed to about 3%, using the appropriate photoelectric corrections for the far UV data.

4.2.3 Calibration Technique. After the demonstration that the thermopile is a reliable detector at longer wavelengths when calibrated by an ion chamber below 100 nm, a UV spectrometer and detector chamber were built to perform UV calibrations on working standard diodes from 100–300 nm [10]. The detection system used ac signal detection and processing, since the magnitude of the thermopile emf in the far UV is very weak compared to changes in the background blackbody ra-

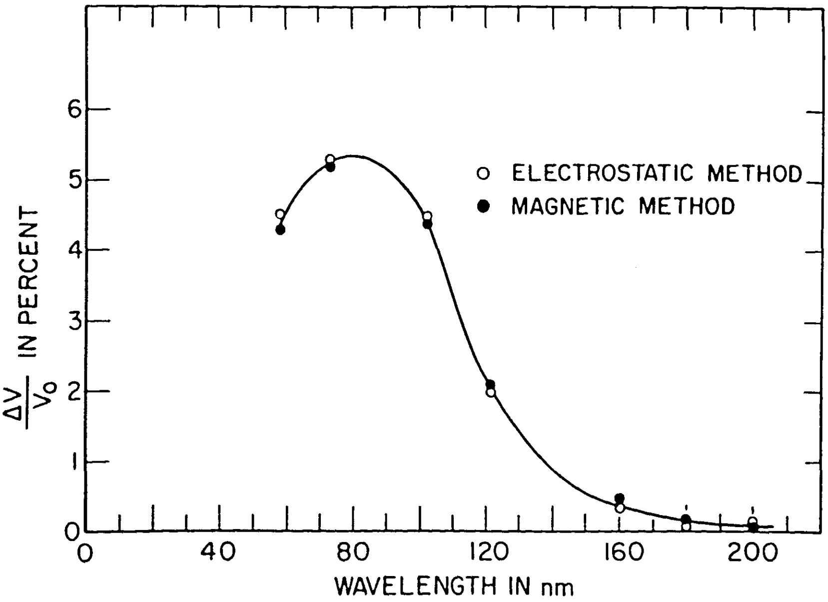

Figure 7–Wavelength dependence of thermopile signal loss due to photoejected electrons.

diation, which is also detected by a thermal detector in a dc mode.

Vacuum UV light is obtained from a 1-m normal incidence grating monochromator, equipped with a duoplasmatron light source. A 13 Hz chopper, located between the light source and the entrance slit, is used during thermopile measurements to interrupt the light entering the monochromator. Attached to the exit arm of the monochromator is a vacuum chamber which houses the ion chamber and thermopile.

The thermopile used is of the extended junction variety, employing three such junctions to give a sensitive area 1 mm×6 mm. It is essentially identical to the one used in the earlier study of thermopiles mentioned above. A rectangular mask with an opening slightly smaller than the area of the thermopile is used. A three point mounting, designed kinematically for accurate relocation, positions the thermopile relative to the surface of the mask, about 0.5 mm from its surface. The thermopile signal is amplified by a 13-Hz amplifier, rectified synchronously with the chopping frequency and recorded using calibrated picoammeters. Net emf readings are taken and referenced to a stable ac test voltage that is applied across the thermopile in the absence of radiation. Immediately following thermopile data acquisition, the thermopile is rotated away from the mask, and the ion chamber or diode being calibrated is exposed to the monochromatized light. The ion chamber or diode currents are then measured. (A gas manifold and set of pneumatic valves are programmed to initiate the appropriate flow of gas before the ion chamber current measurements are made. After the measurements the gas is pumped away.) The thermopile is then rotated back onto its kinematic mounts behind the mask for another measurement. Alternating measurements are made in this way until enough data have been accumulated to overcome the signal-to-noise problems of the thermopile in the far UV.

An additional, independent calibration of the standard diode is made at 253.7 nm. At this wavelength a stabilized low pressure Hg lamp, calibrated for spectral irradiance at this wavelength by blackbody radiometry techniques, is used as a spectral irradiance standard. The diode quantum efficiency is determined from the known flux falling on the diode and the measured diode current.

4.2.4 System Description. The system as it is presently operated is shown schematically in figure 8, and consists of three distinct parts:

1) Duoplasmatron light source
2) Grating Monochromator
3) Detector chamber

The duoplasmatron light source is a three electrode device, composed of a Pt mesh filament coated with an emitting material, a baffle electrode, and an anode (see fig. 9). A low pressure arc discharge is constricted by the funnel-shaped baffle and the anode. An axial magnetic field produced by a cylindrical permanent magnet surrounding the outer shell of the light source further constricts the discharge to a narrow plasma beam along the axis. Helium is used for 58.4 nm, neon for 73.6 nm, argon for 92.0 nm, and hydrogen for the 116–320 nm region. The first three gases are used in the ion chamber-thermopile calibration, and hydrogen for the standard diode vs. thermopile calibration. The

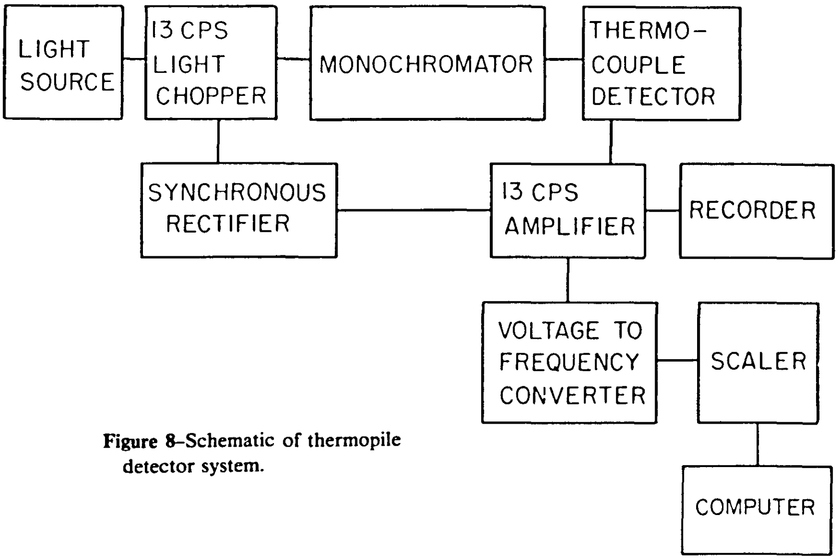

Figure 8–Schematic of thermopile detector system.

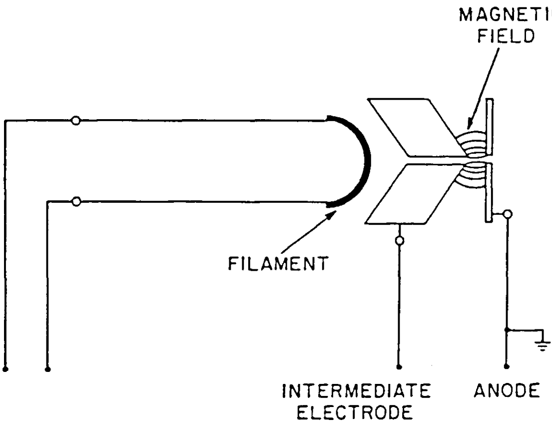

Figure 9-Duoplasmatron light source.

major arc currents are normally 1.5 A for the rare gases, and 1.1 A for hydrogen.

A chopper blade is located between the light source and the monochromator entrance slit, and is driven in a reciprocating motion through a bellows by a small motor immediately below the light source housing. A flap valve, operated by a stepping motor, is placed after the chopper blade and can be rotated either to seal off the light source from the monochromator, to block the light but allow pumping of the light source through the entrance slit, or to let the light enter the monochromator. The entrance slit is vertical and has a micrometer adjustment of 200 microns per turn.

The grating monochromator is a 1-m normal incidence monochromator with a spherical grating of 600 lines/mm and a dispersion at the exit slit of 1.67 nm/mm. The dispersion plane is horizontal. The monochromator is pumped by 6″ oil diffusion pump with a freon-refrigerated baffle to reduce oil contamination in the monochromator chamber. A pneumatic gate valve above the freon baffle is electrically connected to a presure-sensing relay, and closes automatically if the system pressure rises above a preset value. This arrangement protects the system from unforeseen pressure bursts or leaks. A separate roughing valve allows the monochromator to be pumped down from atmospheric pressure without turning off the diffusion pump.

The detector chamber contains the thermopile in its rotatable mount, and has provision for placing the double ionization chamber or the diode to be calibrated in the light beam passing through the exit slit (see fig. 4). The exit slit is a fixed vertical slit 0.8 mm wide, corresponding to about 1.3 nm band width.

The thermopile (fig. 10) is a series connection of three elements which are composed of bismuth-tellurium and bismuth-antimony alloys. The thermal junctions are extended using gold flakes of 1 mm×2 mm area. Together they form a sensitive area 1 mm×6 mm. The thermopile is compensated, designed for a 13 Hz chopping frequency and constructed entirely of nonmagnetic materials. The time constant of the thermopile is about 0.04 s, and has a typical sensitivity (in vacuum) of 1 microvolt/microwatt and an ENI (equivalent noise input) power of approximately 10^{-9} W. An impedance-matching transformer is used between the thermopile and a preamplifier.

The signal from the preamplifier is fed to a 13 Hz broadly tuned amplifier. The output of this amplifier is rectified synchronously with the chopping frequency by a mechanically coupled rectifier. The signal is then filtered, further amplified, and fed into a V-F converter. A small computer is used to record the data and perform statistical evaluation of the results.

A flap valve is mounted 6 cm in front of the mask, and when closed allows the detector chamber to be let up to atmospheric pressure without affecting the rest of the system. The rear section of the detector chamber is bolted to the rest of the chamber using a Viton gasket as a vacuum seal. Entrance to the detector chamber is obtained by removing this rear section.

The thermopile is attached to a rotatable mounting so that, under computer control, it may be brought into registration with the kinematic mount, or rotated between the plates of the ion chamber out of the beam.

The ion chamber used is a double ion chamber similar to that described by Samson [3] (see also section 2). The length of each collector plate is 10.2 cm, and the forward end of the first plate is positioned in the plane of the mask. The axis of the light beam is 0.8 cm from the positive plate, which,

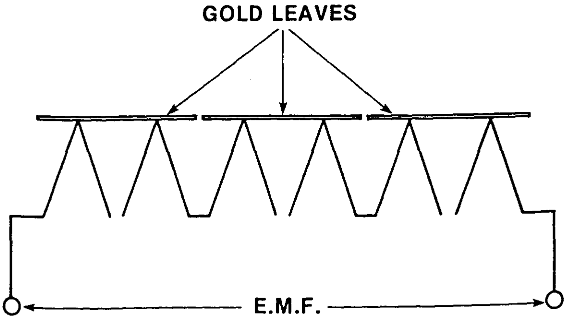

Figure 10-Schematic of thermopile detector.

with the mask, is kept at +22 V with respect to the collector plates. The ion chamber assembly is a self-contained unit with teflon bars used as framework to support the various polished stainless steel plates. The assembly is positioned behind the mask reproducibly by a locating screw and machined recess in the floor of the chamber.

Two corrections applied to the data as they are recorded (i.e. in real time) are as follows:
1) The thermopile signal is corrected for losses through photoemission, amounting to 4.4% at 58.4 nm, 5.3% at 73.6 nm, and 5.1% at 92.0 nm (fig. 7).
2) The reduction in flux entering the ion chamber due to absorption by the argon or xenon leaking into the monochromator through the exit slit is corrected for by making a separate measurement of attenuation vs. monochromator pressure over a range of pressures. Thus by monitoring the monochromator pressure the appropriate correction, typically 4%, can be applied.

The MgF_2-windowed diodes are then calibrated against the thermopile at 23 wavelengths from 116.4 to 253.7 nm. The light source gas is hydrogen over this entire wavelength range. From 116.4 to 160.8 nm, the hydrogen line spectrum is used. Above 160.8 nm the emission is from the molecular hydrogen continuum. A quartz filter is placed in front of the light source when wavelengths longer than 160.8 nm are used to prevent second order radiation from reaching the thermopile and diode.

4.3 Photodiode Intercomparison System (50–254 nm)

4.3.1 History. In 1968 a system was built whose primary purpose was to calibrate outgoing transfer standard detectors by intercomparison with NBS working standards which had been calibrated by the already existing thermopile system [5]. Initially, this system lacked any control or data reduction capabilities; this was added in the early 1970's and upgraded in an evolutionary fashion to the present configuration, in which nearly all data acquisition and reduction functions are automated. With this evolution came the additional capability of performing absolute calibrations of windowless photodiodes in the 50–92 nm spectral region, which greatly expanded the coverage possible and considerably reduced the time required. In the present form, intercomparison-type calibrations are conducted from 50 nm to 254 nm, and absolute calibrations from 50 nm to 92 nm.

4.3.2 Experiment. The basic configuration of the experimental system is very much the same as that of the thermopile system. A duoplasmatron light source illuminates the entrance slit of a normal-incidence vacuum monochromator, and the experimental chamber is attached to the exit slit flange. Various experiments are permanently attached to modular flanges, which can be exchanged on the otherwise empty chamber. Data acquisition and reduction is under the control of a programmable calculator.

4.3.2.1 Monochromator. A one meter normal-incidence McPherson model 225 monochromator is used with its own vacuum pumping system. A 15 cfm mechanical forepump is used for both rough pumping and for backing a 7″ diffusion pump, which uses DC705 silicone pumping fluid. A refrigerated chevron trap and pneumatic gate valve are attached to the top of the pump. A zeolite molecular sieve trap is used in the foreline to minimize the migration of forepump oil vapors into the high vacuum system. Both exit and entrance slits are laterally adjustable, and both the exit and entrance flanges may be isolated from the monochromator vacuum by manual flap valves. The diffraction grating is a 600/mm replica, with nominal blaze at 150 nm. The dispersion at the exit slit is thus 1.67 nm/mm. A modified sine-bar drive provides wavelength scanning by both rotation and translation of the grating.

4.3.2.2 Light Source. A duoplasmatron source, fabricated in-house, is used for all spectral regions in this system. A manifold allows the introduction of any of several gases as appropriate for the emission desired, and a roughing line is attached to the foreline of the experimental system. This type of source uses a hot filament, three electrodes and a pinching magnetic field to create a rather dense plasma which is on the optic axis of the monochromator. Because it is only about 1.5 mm in diameter and is several cm from the entrance slit, only the central portion of the grating is illuminated by the plasma. Gases routinely used at wavelengths short of 100 nm are helium, argon, krypton, and neon. For wavelengths longer than 100 nm hydrogen is used. Cooling of the source is by forced air both in the area where the plasma strikes the anode and around the exterior of the filament end. Separate unregulated power supplies are used for the filament (ac) and the minor and major arcs (dc). A cross section of the duoplasmatron is shown in figure 9.

4.3.2.3 Experimental Chamber. A cylindrical stainless steel chamber with provision for rear mounting of modular flanges is attached to the exit slit flange. This chamber is provided with an independent vacuum system, consisting of a 2″ pneumatic gate valve over a refrigerated chevron trap over a 2″ diffusion pump using polyphenyl ether fluid. The 2" pump is backed with a trapped mechanical forepump, which is also used for roughing. The usual valves isolate and protect. Experiments are attached to the chamber mounted on a flange, which attaches to the rear of the chamber.

4.3.2.4 Experimental Modules. Three such modules are routinely used: an intercomparison module, a mapping module, and an ion chamber module.

The intercomparison module contains a rotating wheel, on which two photodiodes may be mounted for intercomparison measurements. In general, the photocathodes of the two photodiodes are shorted to ground, the exception being that when either is in the beam, its photocathode is connected by means of a gold wiper to a vacuum feedthrough. The anodes are tied together and at all times connected to another feedthrough. Provision is made for rotational relocation of either photodiode about its center, and quartz or Vycor filters may be manually inserted in the beam to aid in eliminating overlapping orders orders from the grating.

The mapping module flange has orthogonal linear motions on the atmospheric side driving a shaft going through the flange with a bellows seal. The shaft is supported inside the vacuum by a gimbal mount, so that displacement of the outside end of the shaft will result in a proportional displacement of the end inside the vacuum. Thus an object may be scanned in space inside the vacuum system in a controlled manner. The normal applications of this module would be either to map the response of a photocathode (with the beam stopped by a fixed small aperture) or to map the intensity distribution of the beam (with the small aperture attached to a photodiode). The external motions can be driven by stepping motors, and the exact position may be monitored by linear displacement transducers.

The ion chamber module is used to directly calibrate a windowless photodiode by means of a rare gas double ion chamber [3,4]. Attached to a rotary motion on the vacuum side of the flange are an ion chamber with two 10 cm plates with a guard plate and a photodiode. Either one or the other may be placed in the beam by a stepping motor. As this module is placed into the experimental chamber a small teflon flange near the exit slit provides a seal so that the only leakage path for gas from the chamber into the monochromator is through a small aperture in the exit beam. High purity argon and xenon are individually brought into the chamber on demand with needle valves limiting the flow so as to balance the influx and leakage into the monochromator and give the desired gas pressure. The gate valve beneath the chamber may be program controlled to open and remove the residual rare gas before photodiode readings are taken and to close so that fresh gas may be admitted before making ion current readings.

4.3.2.5 Data Acquisition. Almost all system operations are controlled by a programmable calculator with an external CPU and interfaces to drive stepping motors, actuate solid state relays and hence valves, etc., switch between sources of very low current or analog voltages and actuate and read a counter-timer. Analog voltages are proportionally converted to pulses, which are counted for fixed periods by the counter-timer. The control programs also contain the data reduction routines, so that the final results of an experiment are available at the conclusion of the data acquisition sequences.

5. Treatment of Errors

Uncertainties associated with the measurement of quantum efficiencies are given in each Report of Test as "probable errors," meaning that there is a probability of 0.5 that the true quantum efficiency values lie within the stated error range about the values quoted. The errors represent the expected accuracy of the sample photodiode when properly used in a customer's system, without regard for any systematic errors present in that system.

The probable error values are determined by summation, in quadrature, of estimates of the effect of all sources of systematic errors in the NBS measurements, including the precision of repeated measurements, on the determination of the quantum efficiency of a photodiode. The analysis of the calibration of windowed photodiodes in the thermopile system follows.

The sources of possible error are shown in table 1. Those sources associated with current measurements are due primarily to the probable error of the current source used to calibrate the measuring picoammeters. The gas absorption uncertainty involves the repeatability of ion gauge measurements (the calibration of such gauges has been observed to drift in time). The photoelectric correction is an empirically determined quantity (see section 4.2) which may vary from the samples originally measured.

The cathode uniformity is measured on each photodiode and units with more than 5% variation in pixel spatial response over the central 1 cm diameter area are rejected. (Should a photodiode be

Table 1. Thermopile-based calibrations.

Error Source	Estimated Uncertainty (%)
Calibration of thermopile (58-92 nm):	
ion current (electrometer manufacturer)	2
gas absorption (estimated)	1
photoelectric correction (estimated)	0–1
measurement precision (observed)	3
radiation impurity (estimated)	0–0.5
Photodiode calibration by thermopile (116–253 nm):	
photocurrent (electrometer manufacturer)	2
photoelectric correction (estimated)	0–1
cathode uniformity (observed)	2
thermopile wavelength sensitivity variation (estimated)	3
measurement precision (observed)	2–8
radiation impurity (estimated)	0–1
Probable Error (%)	**6–10**

found to have a discontinuous uniformity function, even within the 5% acceptance criterion, it would not be issued as a transfer standard.) The portion of the measured area actually used in the NBS measurements is the central 4×5 mm section, and the intensity distribution in the incident beam is relatively uniform over much of this area. The ultimate user of a photodiode will also illuminate the central area of the photocathode, but with a generally different intensity distribution and, perhaps, a somewhat larger area illuminated. This would result in an error in the transfer of the NBS calibration, but not approaching the peak variation of 5% allowed in device acceptance. Our estimate is a probable error of 2% from this source.

The variation of thermopile sensitivity (with wavelength) is an estimate based on the variation seen within the 58–92 nm range and the cross-calibration of detectors using a calibrated mercury source (section 3). The measurement precision (repeatability) is a function of wavelength in the above case in the upper portion of the windowed photodiode calibration range because of deteriorating signal-to-noise in the thermopile measurements as the efficiency of the optics declines and the intensity of the beam is thus reduced.

The above example covers the case of uncertainties in the calibration of windowed photodiodes. The probable error currently being quoted for windowless photodiode calibrations is 10–15% in the 5-50 nm region and 8% in the 50–122 nm region. These errors are determined from the analyses displayed in tables 2 and 3.

In the table 2 analysis, the cross section and multiple yield data are taken from published sources with interpolation between published wavelengths where necessary. Since, in this region, the reduction of ionization chamber data entails the use of gas constants, including the pressure and temperature, the contribution to the error budget from these must be included. Errors arising from measurements of current are primarily from the variance within sets of three consecutive conversions of currents permitted in the acquisition program. The radiation impurity contribution can only be estimated from observation of system performance, and could include improper assessment of overlapping orders from the diffraction gratings, stray light from masks, baffles, walls, etc., the "zero order tail" from the gratings, and imperfections in the filters used to minimize this source of error. This error would be wavelength dependent, of course.

All current measurements in the region covered in table 2 are conducted with a single picoammeter, and since it is the ratio of photodiode to ion chamber currents that is used to calculate quantum efficiency, an absolute calibration of this picoammeter is not necessary. The estimated uncertainties associated with current measurements would be largely due to ionization of residual gases and other spurious effects. The gas absorption correction is necessary only during ion chamber measurements to account for the radiant flux absorbed in the monochromator (typically 10% or less) so the likely error from this source is minimal. The stabil-

Table 2. Windowless photodiode calibrations at SURF (5–50 nm).

Error Source	Estimated Uncertainty (%)
gas cross sections (data reference)	3–4
multiple yield (data reference)	0–1
gas temperature (estimated)	0–0.5
gas pressure (transducer manufacturer)	0–3
photocurrent precision (observed)	2–6
ion current precision (observed)	5–7
radiation impurity (estimated)	8–12
Probable Error (%)	**10–15**

Table 3. Windowless photodiode calibrations (non-SURF, 50–122 nm).

Error Source	Estimated Uncertainty (%)
photodiode current (estimated)	2
ion current (estimated)	2
gas absorption correction (estimated)	0–1
measurement precision (observed)	3
stability of quantum efficiency (estimated)	7
radiation impurity (estimated)	0–1
Probable Error (%)	**8**

ity of the quantum efficiency of working standard photodiodes is felt to be a possible source of error only in the longer wavelength region (50–122 nm), since in the 5–50 nm region (at SURF-II) the photodiodes are calibrated and stored in ultrahigh vacuum, whereas in the other facility calibrations are in an oil-pumped system, and storage is in air.

The assistance of Robert P. Madden, Edward B. Saloman, David L. Ederer and Lanny Hughey is gratefully acknowledged. Dr. Madden has been group leader of the Far Ultraviolet Physics Section throughout the period during which the far ultraviolet detector calibrations program has been active. Dr. Saloman was responsible for setting up the original SURF detector calibration system, with the technical assistance of Mr. Hughey, and, with Dr. Ederer, for conducting the analysis which led to the capability of interpreting data from short wavelengths.

References

[1] Canfield, L. R.; R. G. Johnston and R. P. Madden, NBS Report #9897.
[2] Hass, G., J. Opt. Soc. Am. **39** 532 (1949).
[3] Samson, J. A. R., J. Opt. Soc. Am. **54** 6 (1964).
[4] Samson, J. A. R., and G. N. Haddad, J. Opt. Soc. Am. **64** 47 (1974).
[5] Johnston, R. G., and R. P. Madden, Appl. Opt. **4** 1574 (1965).
[6] Canfield, L. R.; R. G. Johnston, K. Codling, and R. P. Madden, Appl. Opt. **6** 1886 (1967).
[7] Saloman, E. B., and D. L. Ederer, Appl. Opt. **14** 1029 (1975).
[8] Day, R. H.; P. Lee, E. B. Saloman, and D. J. Nagel, J. Appl. Phys. **52** 6965 (1981).
[9] Saloman, E. B.; J. S. Pearlman and B. L. Henke, Appl. Opt. **19** 749 (1980).
[10] Canfield, L. R.; R. G. Johnston and R. P. Madden, Appl. Opt. **12** 1611 (1973).

Journal of Research of the National Bureau of Standards

Description of the Thermotropic Behavior Of Membrane Bilayers In Terms of Raman Spectral Parameters: A Two-State Model

Volume 92 Number 2 March–April 1987

William H. Kirchhoff

National Bureau of Standards
Gaithersburg, MD 20899

Ira W. Levin

National Institutes of Health
Bethesda, MD 20205

An analytical expression is developed for describing the thermotropic behavior of membrane bilayers as studied by Raman spectroscopy. The expression is derived from a two-state model of the main gel to liquid crystalline phase transition in lipid bilayers. Experimental data for a variety of diacylphosphatidylcholines and their derivatives have been fit by least squares to the two-state expression to within currently achievable measurement error. Numerical techniques have been developed for placing bounds on the parameters of the two-state model in situations of sparse data in the phase transition region. By fitting the model to the measured spectroscopic data, estimates of the extent of cooperativity in the phase transition can be obtained in a systematic manner.

Key words: logistic function; membrane; phase transition; Raman spectroscopy; two-state model.

Accepted: December 3, 1986

Introduction

In recent years the use of Raman spectroscopy for the study of the phase transition and the order/disorder behavior of both intact and reconstituted membrane bilayers has gained dramatically in popularity through the wide range of applications amenable to spectroscopic techniques [1][1]. Although calorimetric measurements can provide accurate information on enthalpy changes that occur during phase transitions, they provide little insight into the nature of the molecular reorganization accompanying the phase transition. Since Raman spectra are particularly sensitive to the conformational, packing, and dynamical changes involving the hydrocarbon chains, bilayer reorganizations within, for example, the hydrophobic region of the membrane, may be monitored directly as a function of temperature. These observations can be made in an aqueous medium, without either the introduction of bulky molecular probes or elaborate sample preparation. By using low laser excitation powers (15–200 mW) at the sample, external perturbations to the system are minimized. Because of the sensitivity of the spectra to conformational changes, Raman spectroscopy has also been useful in elucidating the effects of intrinsic and peripheral components such as sterols and proteins on the thermal properties of membranes. In a few systems, reconstituted, naturally-occurring membranes have been studied and have provided useful information obtainable only from spectroscopic examination [2].

Although the vibrational assignments for the spectra of lipid bilayers are complex, they are understood sufficiently well to allow discussion of

About the Authors: William H. Kirchhoff is with the NBS Center for Chemical Physics. Ira W. Levin is with the Laboratory of Chemical Physics in the National Institute of Arthritis, Diabetes, and Digestive and Kidney Diseases, NIH.

---

[1] Figures in brackets indicate literature references.

membrane reorganizations in terms of the observed spectroscopic frequencies, intensities and linewidths of a variety of spectral features reflecting the headgroup, interface, and acyl chain regions of the lipid components. A particularly useful approach for presenting the thermal data has been in terms of spectral peak height intensity ratios determined from either the 2900 cm^{-1} carbon-hydrogen or 1100 cm^{-1} carbon-carbon stretching mode regions. In general, these data are primarily sensitive either to alterations in the lateral interactions or to intermolecular order of the acyl chains and intrachain *trans-gauche* conformational changes, respectively.

In this paper we propose an analytical expression, based upon a two-state model of the primary phase transition phenomenon, which is useful for systematically describing the form of the temperature profiles. We also describe an approach, based on a nonlinear, least squares analysis, for extracting relevant thermodynamic information from the temperature dependence of the observed spectra. This approach is robust in handling the range of data encountered in studies of membrane phase transitions.

Thermodynamic Model

Within the last 10 years a number of models have appeared describing within either a thermodynamic or statistical mechanical framework various features of the main phase transition in membrane bilayers. Most of these models have been critically reviewed by Nagle [3]. An additional review by Israelachvili, et al. [4] discusses the physical principles of membrane organization and includes descriptions of membrane-protein interactions and nonbilayer lipid structures. We concern ourselves here with the simplest of these phase transition models; namely, that of thermodynamic equilibrium between noninteracting domains in either one of two states [5]. We have been guided by the philosophy that the accuracy with which a simple model can quantitatively describe the experimental data serves as a guide to assessing the required features of a more complex model, to comparing and evaluating two or more models, and to defining the accuracy requirements of additional measurements.

The derivation of the thermodynamic model is presented in Appendix A in detail in order to distinguish clearly between numbers of molecules and numbers of domains in each of the two states since the observed spectral intensities are determined by the number of molecules in each of the states while the temperature dependence of the spectral intensities is determined by the distribution of domain sizes. The mathematical development follows closely the description by Hill of the two-state model for small systems [6]. The resulting analytical expression for the temperature dependence of the Raman spectra are identical to those published by Dluhy, et al. [7] using the Zimm-Bragg theory originally developed for describing polypeptide denaturation [8]. The difference between the thermodynamic and the Zimm-Bragg developments is in the interpretation of the parameters derived from the analysis. We prefer the thermodynamic development because of the simplicity of its physical interpretation. For so long as the data are described by a simple model, it seems little more than a matter of taste as to how the parameters are to be interpreted. Only when the data can be seen to contain additional information would it be fruitful to apply a more complex model. Finally, though the derivation is applied in this paper to Raman spectroscopic data, it is generally applicable to all spectroscopic studies of such cooperative phenomena.

In the two-state model, a single bilayer is considered to consist of domains of varying numbers of lipid molecules n with each domain existing in one of two states labeled A and B. The distribution of domain sizes and the requirement that all molecules within a domain exist either in state A (the low-temperature gel state) or in state B (the high-temperature liquid crystalline state) determine the cooperativity exhibited by the bilayers during the phase transition between the two states. The distribution of domain sizes is assumed to be temperature independent, while the number of domains in either state is temperature dependent. Although a phase transition in the strictest sense is excluded for a distribution of domains of finite size, the discontinuous nature of the phase transition will be approximated for large values of n.

The temperature dependence of the intensity $I\nu$ of a spectral feature (Raman or otherwise) that depends upon the distribution between two states of the molecules being observed is given by eq (A32) in Appendix A:

$$I=\frac{I_{A\nu}}{(1+e^{t})}+\frac{I_{B\nu}}{(1+e^{-t})} \tag{1}$$

The dimensionless, reduced temperature t is defined as $t=(T-T_0)/D$, where T_0 is the midpoint of the phase transition and the scale factor D is related to the enthalpy of transition per mole of lipid molecules, $\Delta\bar{H}$, and the effective domain size, n_{eff}, by:

$$D=(RT_0^2)/\Delta\bar{H}n_{\text{eff}} \tag{2}$$

As discussed in Appendix A, eq (1) represents an approximation to a summation over a distribution of domain sizes. To test the accuracy of this approximation, sets of hypothetical data were created using a lognormal distribution [9] of domain sizes from which Raman intensities were calculated for values of N_A and N_B, the numbers of molecules in states A and B respectively. The values of N_A and N_B were calculated for the lognormal distribution using eqs (A21) and (A24). The lognormal distribution was chosen because it excludes domains of negative size and allows for a pronounced skewing to high values of n. This skewing causes various measures of the center of the distribution to differ significantly and provides a sensitive test of a single-term approximation to a sum over a distribution. The data sets corresponded to distributions of varying breadth which, when fit by the method of least squares to eq (1), gave the same value of n_{eff}.

In table 1, five measures of the center of a distribution: the mode, M, which is the most populous value of n, the mean value of n, $<n>$, the root mean square of n, $\surd<n^2>$, the median, $n(50\%)$, and the value of $<n^2>/<n>$ are compared with the value of n_{eff} returned by the least squares fit for three distributions of varying spread. It can be seen that as the spread of the distribution narrows, the agreement of all of these measures improves. Even though, for the broadest distribution, the values of these measures covered more than an order of magnitude, eq (1) gave a satisfactory fit with a relative standard deviation of 2%.

Table 1. Comparison of a single term fit to three distributions.

	Mode	1	30	90
	Range in n[a]	1–11, 679	1–3, 963	21–387
Distribution Parameters	$<n>$	36.3	79.2	98.2
	$\surd<n^2>$	113.7	109.5	101.0
	$<n^2>/<n>$	356.3	151.3	104.0
	median	117	110	101
Least Squares Fit to Eq 1	n^{eff}	100	100	100
	s[b]	2.1%	1.2%	0.2%
to Eq 3	n_{eff}	136.2	113	101
	s	1.0%	0.8%	0.2%
	slope[c]	0.46%	0.24%	0.02%

[a] Range: values of n for which the population $>10^{-8}$ x population of mode.

[b] s: relative (to the value of A-B) standard deviation of the least squares fit.

[c] slope: value of baseline slope relative to the value of A-B.

Other conclusions may be drawn from the data presented in table 1. The value of n_{eff} obtained from the least squares fit was best approximated by the root mean square value $\surd<n^2>$, and the median, $n(50\%)$, rather than by $<n^2>/<n>$ as we had initially expected. This is a function, however, of the density of data in the vicinity of the transition interval. If the data range is narrowed to include only the transition interval and if the number of data in that region is increased, then the limit of $<n^2>/<n>$ is approached in agreement with the observation in Appendix A that this measure gives the correct temperature dependence at the asymptotes and at the inflection point when used in a single term approximation to the sum over domain sizes. Another pronounced effect of the spread of the distribution was to give a more gradual convergence to the asymptotic limits and thus, the appearance of sloping rather than horizontal asymptotes. This can be seen in figure 1 in which the hypothetical intensity ratio profiles are drawn for each of the three distributions listed in table 1. The sloping asymptotes arise from contributions from domains of small size as originally suggested by Sturtevant [10].

A somewhat better fit to broad distributions can be obtained by modifying eq (1) in order to allow for nonhorizontal asymptotes, namely:

$$I\nu=\frac{I_{A\nu}+I_{a\nu}(T-T_0)}{(1+e^{t})}+\frac{I_{B\nu}+I_{b\nu}(T-T_0)}{(1+e^{-t})}. \tag{3}$$

From table 1 it can be seen that inclusion of a nonhorizontal baseline in the fit of the hypothetical data improved the quality of the fit, as judged by the standard deviation, and increased the estimate of the value of n slightly, though not nearly enough to bring it to its expected value of $<n^2>/<n>$.

In the absence of an analytical expression such as eq (3), it has been customary to estimate T_0 and the van't Hoff enthalpies from observed temperature profiles using straight line approximations to the three distinct regions of the profiles. Thus, ΔT has been defined as the temperature interval between the intersection of a line drawn tangent to the phase transition curve at its inflection point and the two lines drawn tangent to the high and low temperature asymptotes. This definition of ΔT is illustrated in figure 2. The relationship of ΔT to the scale parameter D of eq (3) can be calculated directly to give $\Delta T=4D$, ignoring terms of order

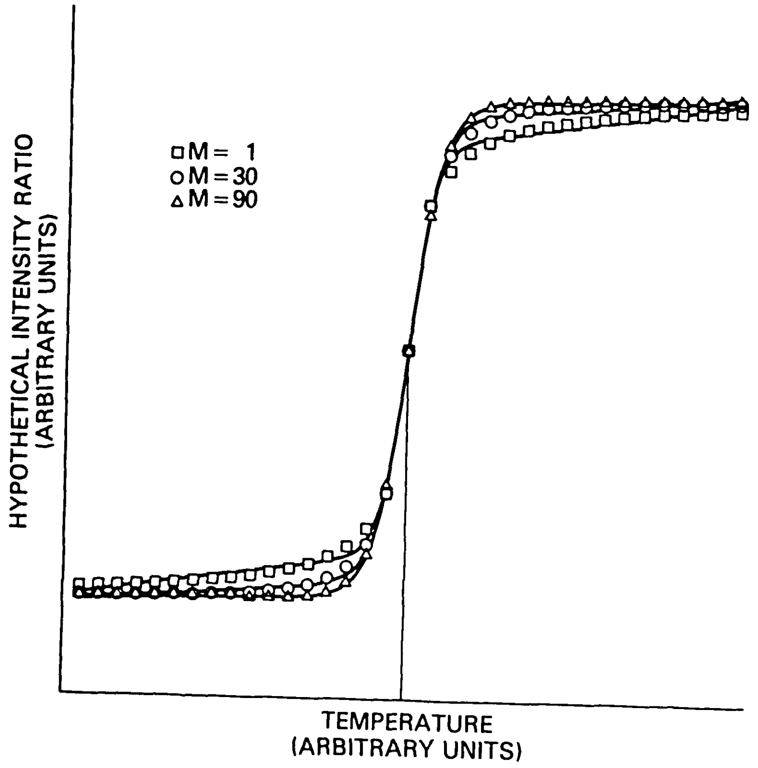

Figure 1–A graphical comparison of the temperature dependence of hypothetical Raman intensity ratios for three domain size distributions with modes $M=1$, 30, and 90 and $n_{\text{eff}}=100$.

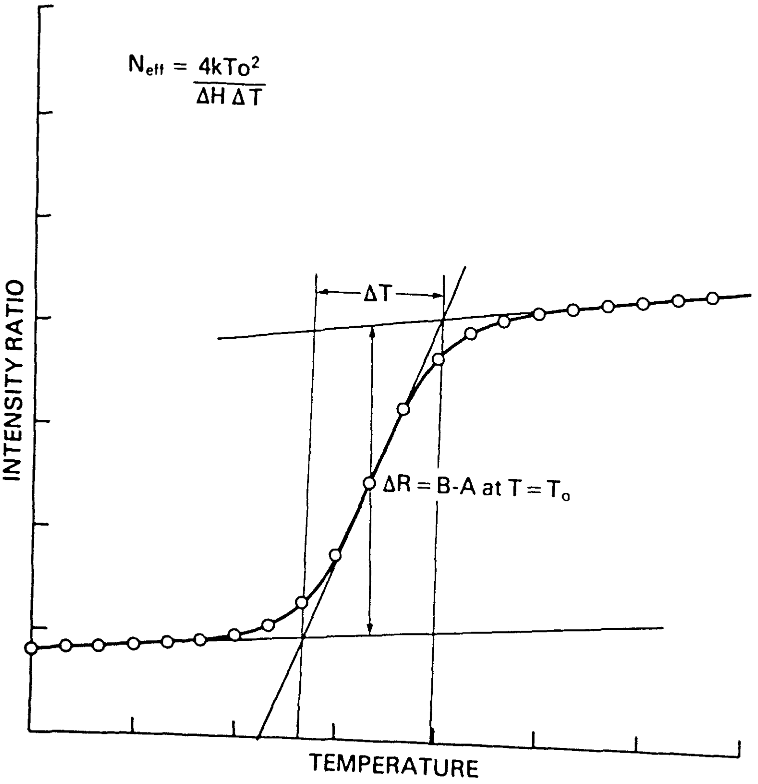

Figure 2–Relationship between the parameters of eq (5) and the graphical analysis of phase transition curves.

$(I_{b\nu}-I_{a\nu})/(I_{B\nu}-I_{A\nu})$. From the definition of D given by eq (2),

$$\Delta T=(4RT_0^2)/\Delta\bar{H}n_{\text{eff}}. \tag{4}$$

Comparison of eq (4) with similar expressions given by Sturtevant [11] indicates that ΔT corresponds to the ΔT used for calorimetric determinations of van't Hoff enthalpies. Care should be taken in the interpretation of n_{eff}, however, since estimates of the slope made as close to the inflection point as possible will give values of n_{eff} approaching $<n^2>/<n>$ which, for broad distributions of domain sizes, can be an order of magnitude higher than $<n>$.

In the Raman spectroscopic experiment temperature profiles are collected over periods of several hours. Since fluctuations in the intensity of the incident laser radiation lead to corresponding fluctuations in the observed Raman intensities, the ratio of the intensities of two spectral features at different scattering frequencies provides a more precisely defined temperature profile which is relatively independent of the experimental environment. Moreover, if the vibrational features are chosen to be sensitive to the ordering of the lipid hydrocarbon chains, the temperature dependence of the intensity ratio will be more pronounced than for the individual intensities themselves.

Forming the ratio $r_{12}=I_1/I_2$ and substituting eq (3) for I_1 and I_2, we obtain after rearrangement,

$$r_{12}=\frac{A+a(T-T_0)}{(1+\mathrm{e}^{t'})}+\frac{B+b(T-T_0)}{(1+\mathrm{e}^{-t'})} \tag{5}$$

where, to first order in $I_{a\nu}/I_{A\nu}$ or $I_{b\nu}/I_{B\nu}$,

$$A=\frac{I_{A1}}{I_{A2}},\quad a=\frac{1}{I_{A2}}\left(I_{a1}-I_{a2}\left(\frac{I_{A1}}{I_{A2}}\right)\right),\quad B=\frac{I_{B1}}{I_{B2}},$$

$$b=\frac{1}{I_{B2}}\left(I_{b1}-I_{b2}\left(\frac{I_{B1}}{I_{B2}}\right)\right),\quad t'=\frac{(T-T_0')}{D},$$

$$\text{and } T_0'=T-D\ln\left(\frac{I_{B2}}{I_{A2}}\right). \tag{6}$$

In the expression for T_0', the contributions from I_{b2} and I_{a2} have been ignored. A comparison of eqs (3) and (5) shows that the intensity ratio has approximately the same functional dependence on temperature as the individual intensities themselves, except that T_0', the apparent midpoint of the phase transition, has been shifted from the true value by an amount $D\ln(I_{B2}/I_{A2})$. If, instead of r_{12}, the temperature behavior of $r_{21}=I_2/I_1$ is analyzed, a new apparent midpoint, $T_0''=T_0-D\ln(I_{B1}/I_{A1})$, is obtained and a comparison of the temperature dependence of r_{21} with r_{12} shows an apparent shift of the transition temperature of $D\ln(B/A)$.

Eqs (3) and (5) are the expressions we have used for the analysis of the Raman intensity profiles. Spectral data are fit by the method of least squares to Raman intensities or intensity ratios. From these fits, estimates of transition temperatures and van't Hoff enthalpies are obtained in a systematic manner. For some systems in which this analysis has been applied, the sharpness of the phase transition requires a particularly robust least squares calculation. Therefore, the details of the least squares analysis are presented in Appendix B.

Analysis of Temperature Profiles Derived From Raman Intensity Ratios

The analytical approach outlined in the preceding section and in the appendices to this paper have been applied to dipalmitoylphosphatidylcholine (DPPC) as well as to several cyclopentanoid analogues of DPPC [12]. In the following discussion, the results of some of these analyses will be described for the purpose of examining the limitations of the two-state model and the ways in which these limitations are made manifest by the statistical analysis.

Although several Raman spectral regions are suitable for deriving temperature profiles from appropriate intensity ratios to assess bilayer reorganizations, we will use the 2900 cm^{-1} C-H stretching mode region for applying the present model. This congested and complex spectral interval, shown in figure 3, for the gel and liquid crystalline states of DPPC has been discussed numerous times (see, for example, ref. [1] and references contained therein). Temperature profiles can be conveniently constructed from changes in the peak height intensity ratios for the 2850, 2885 and 2940 cm^{-1} feature. These spectral transitions are assigned, respectively, to the acyl chain methylene C-H symmetric stretching modes, the methylene C-H asymmetric stretching modes and, in part, a Fermi resonance component of the chain terminal methyl symmetric C-H stretching mode [1].

Figure 4 illustrates the analysis of a typical phase transition profile for multilamellar dispersions of DPPC using the spectral intensity ratios constructed from the C-H stretching mode region. The values of A, B, a and b listed in the figure are the values of the parameters of eq (5) along with their estimated uncertainties. Only one datum, at

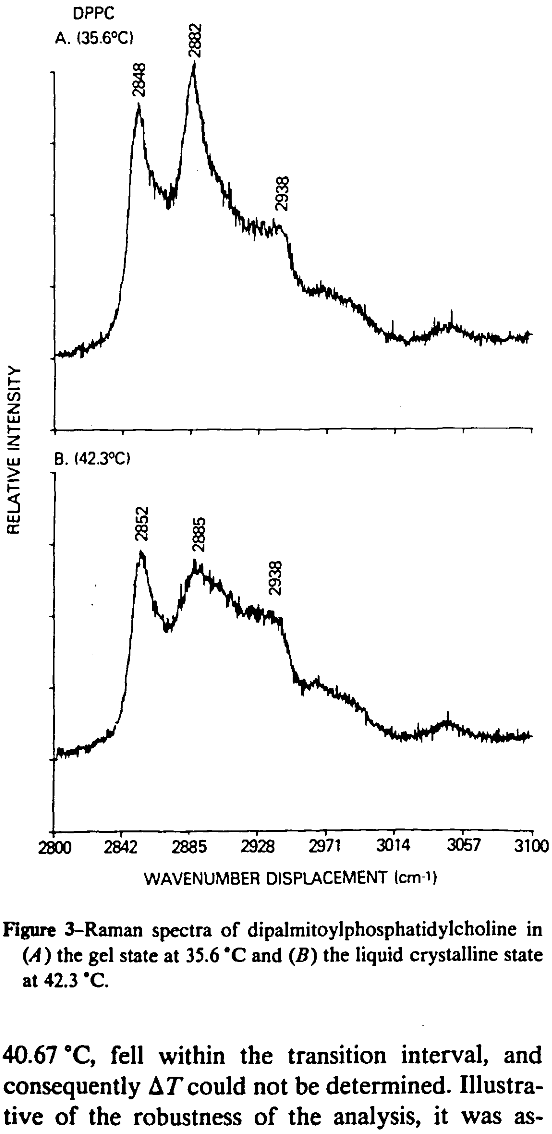

Figure 3–Raman spectra of dipalmitoylphosphatidylcholine in (*A*) the gel state at 35.6 °C and (*B*) the liquid crystalline state at 42.3 °C.

40.67 °C, fell within the transition interval, and consequently ΔT could not be determined. Illustrative of the robustness of the analysis, it was assigned a maximum value based on the temperature separation between the data on either side of 40.67 °C (39.58 and 41.78 °C) and on the standard deviation of the fit using eq (B11) in Appendix B. The transition data range given in figure 4, 1.10 K, is the value of the difference between the measured temperatures below and above T_0 and should be viewed as spanning the uncertainty in T_0. Ninety-five percent confidence limits for T_0 can be obtained from the standard deviation of T_0 returned by the least squares fit, 0.08°, by multiplying by 12.7, the value of the 95% confidence limits of a student's *t* distribution with one degree of freedom, giving 1.02 K in agreement with the transition data range. As might be expected, the value of T_0 as determined by the least squares fit is quite sensitive to the value estimated for ΔT. The estimated inverse shift presented in figure 4 is calculated from $D\ln(B/A)$ and is the shift in T_0 which would have been obtained if $I(2885)/I(2940)$ had been analyzed instead of $I(2940)/I(2885)$. The vertical bars at each data point in figure 4 are twice the value of the uncertainties in the intensity ratios as estimated from the standard deviation of the fit by eq (B1). The three curves passing through the data values correspond to the profile calculated from eq (5) along with plus or minus two standard deviations. Along the horizontal axis of figure 4 is the two standard deviation curve alone. The peak in the uncertainty curve at T_0 signifies that T_0 is being determined almost exclusively by the value of the intensity ratio at the one datum in the transition interval relative to the separation between A and B.

Figure 5 illustrates several of the limitations of the simple two-state model. Four phase transition curves for DPPC from our laboratory using data from different investigators, different spectrometers, and over a two-year interval were compared. Even though the data were separated by 2° intervals, and only one, but always one, datum fell within the transition interval, the analysis provided a surprisingly reproducible phase transition temperature of 40.38 to 41.09 °C, as compared with the more accurate value of 41.55 °C measured calorimetrically by Albon and Sturtevant [5]. The maximum value of ΔT varied from 1.42 to 1.91 °C and reflected varying temperature data intervals and intensity measurement precision.

Using the calorimetric data for DPPC measured by Albon and Sturtevant, namely, $\Delta\bar{H}=8.50$ kcal/mole and $T_0=314.70$ K, and the value obtained for ΔT, minimum values of the cooperative unit of 48 to 65 were calculated from eq (4). If values for the cooperative unit of 100 to 1000, which have been estimated for the phase transition in DPPC, are to be obtained from the analysis of Raman intensity profiles, measurements must be made with temperature increments of 0.1 °C in the phase transition region and with temperature control on the order of 0.01 °C.

If, for the moment, the data for the second run of sample #1B are excluded from figure 5, the values of A, B, a and b all agree to within three standard deviations as estimated by the least squares fit. For the temperature profile of sample #1B, which was measured within 24 hours of the profile of sample #1A, the values of A, B, a and b all varied by more than five standard deviations from the average of the other three profiles. We interpret this observation as an indication that the sample had not yet annealed into its preferred low temperature state.

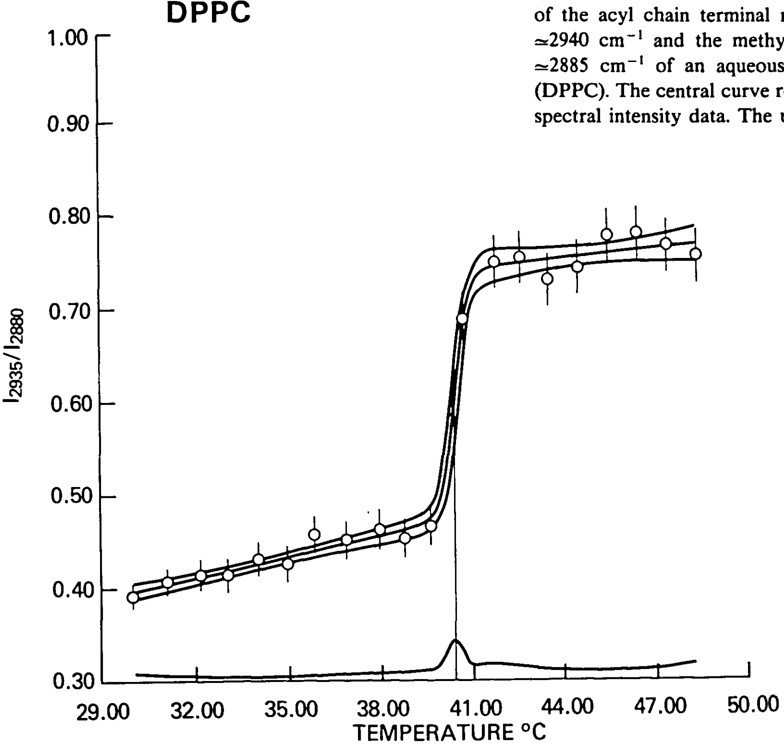

Figure 4–Temperature profile for the ratio of the intensity of the Raman spectral feature associated with, in part, the Fermi resonance component of the acyl chain terminal methyl symmetric C-H stretching mode at $\approx$2940 cm^{-1} and the methylene asymmetric C-H stretching modes at $\approx$2885 cm^{-1} of an aqueous dispersion dipalmitoylphosphatidylcholine (DPPC). The central curve represents the least squares fit of eq (5) to the spectral intensity data. The upper curve represents the calculated curve plus two standard deviations and the lower curve minus two standard deviations. The curve drawn along the bottom axis is the two standard deviation curve alone. The vertical bars are estimates of the uncertainties in the experimental ratios and are based on the weights of the ratios and the overall standard deviation of the fit. The values of the parameters obtained from the fit are as follows: $A=0.474\pm0.006$, $B=0.740\pm0.012$, $a=0.0074\pm0.0008$ and $b=0.0036\pm0.0023$, $T_0=40.38\pm0.08$ °C and $\Delta T<1.76$ °C. The transition data range = 1.10 °C. The estimated inverse shift $=-0.10$ °C. The standard deviation $s=1.70\%$ relative to the value of r at the midpoint of the transition interval.

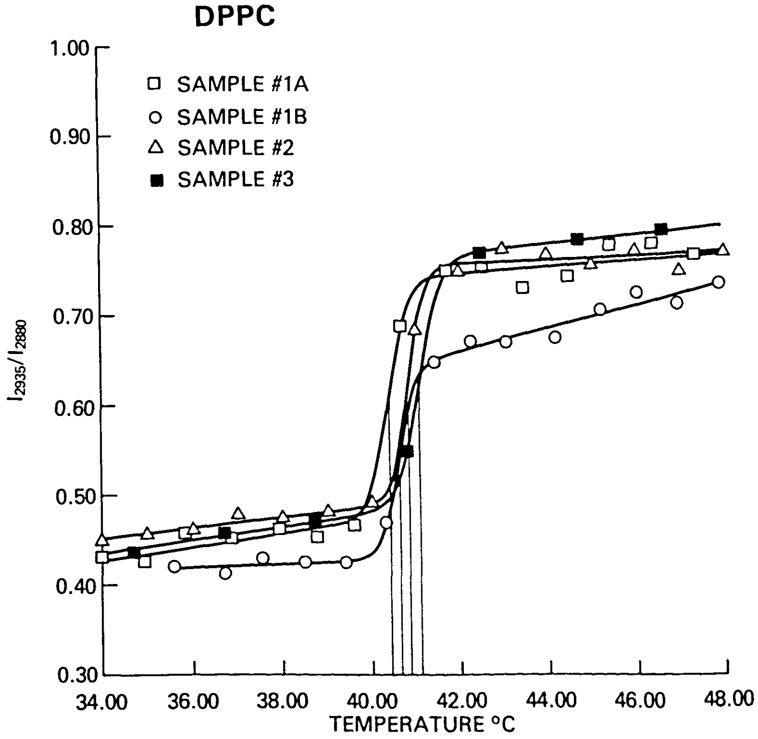

Figure 5–A comparison of four temperature profiles for dipalmitoylphosphatidylcholine (DPPC). The spectra were measured over a period of two years by three different investigators. Spectra for Samples No. 1 and No. 3 were recorded with a scanning spectrophotometer whereas spectra for Sample No. 2 were determined with a spectrograph. All three samples were prepared by the individual investigators using different sources for the lipid. The range in T_0 was 40.4 °C to 41.1 °C.

Its bilayer structure appeared, on comparison with the values of the gel state intensity ratios for the other samples, to be as ordered at low temperatures, although it did not exhibit the gradual increasing disorder associated with the positive value of a. Its phase transition temperature, though somewhat higher than the others, did not change significantly nor did the transition interval to within measurement precision. The transition concluded at a much less disordered state than the other samples and then, corresponding to a large value of b, continued to disorder at a much greater rate than the others until reaching a comparable intensity ratio approximately 10 °C above the phase transition temperature. Although the two-state model cannot explain the molecular origins of such behavior, the fit of the data to eq (5) provides a basis of the intercomparison of temperature profiles in a methodical, reproducible, and quantitative manner.

The values of the asymptotic slopes observed for the temperature profiles of intensity ratios cannot be interpreted on the basis of domains of small size alone. Even for the three conforming profiles in figure 5, the values of the slopes at high and low temperature are on the order of 0.5% to 1.2%, somewhat greater than the value of 0.46% obtained for the broadest domain size distribution reported in table 1. The slopes are most readily interpreted as the ability of the hydrocarbon chains of the lipid molecules to form *gauche* bonds near the acyl chain termini at the bilayer center without triggering the phase transition and, for the liquid crystalline phase, as a continuing disordering following completion of the phase transition.

Figure 6 compares the temperature profiles derived from the $I(2850\ \mathrm{cm}^{-1})/I(2885\ \mathrm{cm}^{-1})$, $I(2940\ \mathrm{cm}^{-1})/I(2850\ \mathrm{cm}^{-1})$ and $I(2940\ \mathrm{cm}^{-1})/I(2885\ \mathrm{cm}^{-1})$ peak height intensity ratios for 1,3/2-1P-dipalmitoylcyclopentane-1,2,3- triol phosphatidic acid, an analog of DPPC in which the glycerol backbone is replaced by a more rigid cyclopentane triol [13]. All three profiles give the same value for the phase transition temperature within the limits of the standard deviations obtained from the least squares fit. The values of ΔT, however, vary, and this variation can be used as a test of a structure-based model for the phase transition, since the $I(2850\ \mathrm{cm}^{-1})/I(2885\ \mathrm{cm}^{-1})$ ratio reflects primarily lateral chain-chain interactions, while the $I(2940\ \mathrm{cm}^{-1})/I(2885\ \mathrm{cm}^{-1})$ ratio reflects *trans-gauche* conformational changes in addition to the lateral effects [14]. This suggests that different chain interactions as probed by different spectral regions may either exhibit different degrees of cooperativity in the phase transition, different energies for the transition, or a combination of both effects.

An even more striking comparison of temperature profiles for the cyclopentanoid derivative of DPPC can be seen in figure 7. Simultaneous measurements of the C-H stretching and the C-C stretching mode regions showed a shift of 1.5° for the transition temperature for the C-C stretching profile, a shift which cannot be explained by the choice of intensities for forming the ratio as sug-

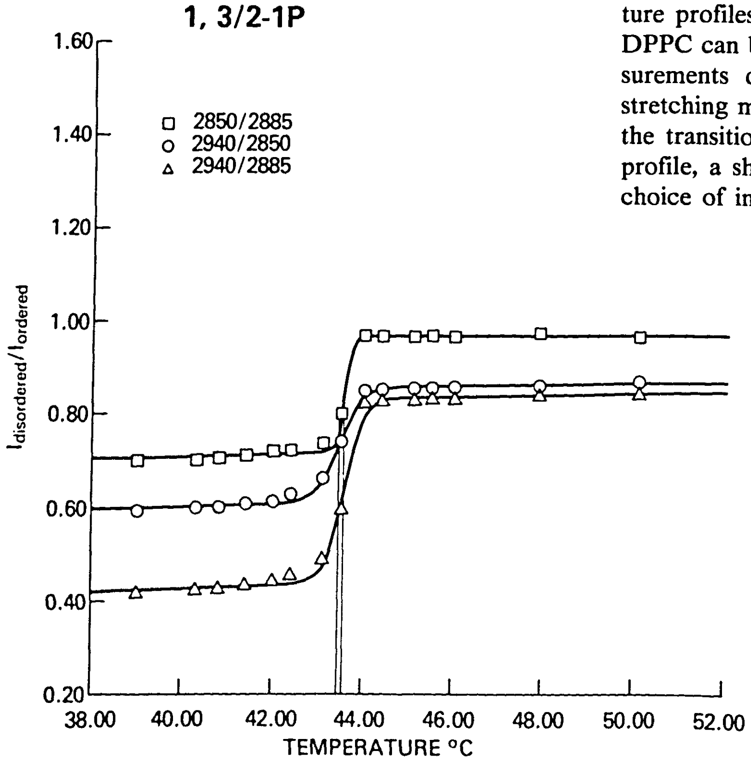

Figure 6–A comparison of the temperature profiles for three spectral features in the C-H stretching region for 1,3/2-1P-dipalmitoylcyclopentane-1,2,3-triol phosphatidic acid. For the 2850/2885 profile (□), T_0=43.6 °C and ΔT=0.6 °C; for the 2940/2850 profile (○), T_0=43.4 °C and ΔT=1.0 °C; for the 2940/2885 profile (△), T_0=43.6 °C and ΔT=0.8 °C.

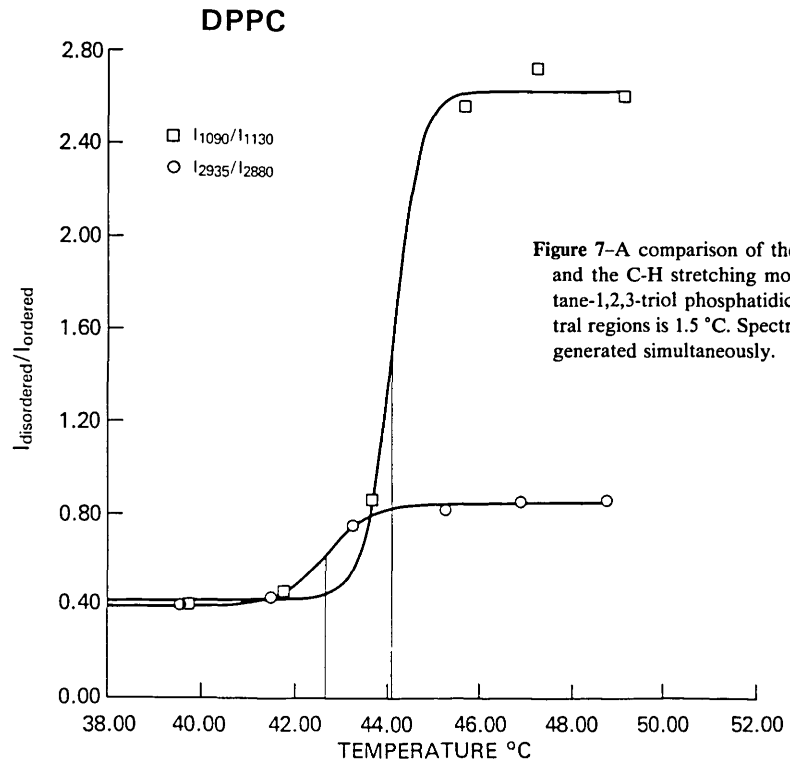

Figure 7–A comparison of the temperature profiles for the C-C stretching and the C-H stretching mode regions for 1,3/2-1P-dipalmitoylcyclopentane-1,2,3-triol phosphatidic acid. The difference in T_0 for the two spectral regions is 1.5 °C. Spectral data for both stretching mode regions were generated simultaneously.

gested by the discussion accompanying eq (6). Although the temperature intervals were too coarse to obtain precise values of ΔT, the difference in T_0 between the two profiles suggests that lattice expansion precedes the intrachain *trans-gauche* isomerization as the bilayer undergoes the phase transition. (The change in the intensity ratio in the C-H stretching region is not only a function of the degree of *trans-gauche* isomerization but also the interactions between neighboring hydrocarbon chains [1].) It is just this type of molecular-scale information that provides insight into the molecular mechanism of the phase transition. Also, without a statistical estimate of the uncertainty in T_0, it would not be possible to assess whether the observed temperature difference is statistically significant.

Finally, returning to figure 6, an asymmetry can be observed in the shapes of profiles which cannot be explained by a thermodynamic equilibrium model. The curvature at low temperature appears to be gradual, while at high temperature the curvature is quite sharp. Such an asymmetry is suggestive of a coalescing of domains of liquid crystalline lipid to give a narrower distribution of domains of larger size toward the end of the transition. This behavior is similar to that implied by the model of Freire and Biltonen [15], and observed by Marsh et al., using electron spin resonance techniques to examine the DPPC phase transition [16].

Conclusions

We have outlined a systematic approach for extracting phase transition temperatures and van't Hoff enthalpies from temperature profiles derived from Raman spectral peak height intensity ratios. Within the degree of precision of the experimental data; namely, temperature intervals of 1–2 °C, temperature measurement accuracy of 0.1 °C, and peak height intensity measurement accuracy of 1 to 5%, the simple, equilibrium, two-state model implied by eq (5) fits most of the experimental data to within measurement error. Alternatively, with the above degree of precision of the experimental data, it will not be possible to distinguish between more detailed models. As a next step, therefore, in the systematic evaluation of phase transition behavior through Raman spectroscopic studies, the precision of the temperature and intensity measurements must be improved by an order of magnitude while decreasing the temperature intervals throughout the phase transition region by an order of magnitude.

The advantage of deriving an analytical expression for the Raman intensity behavior as a function of temperature lies in the development of statistically based assessments of competing models. Data such as the exact profile curvature immediately preceding and following the phase transition and hysteresis effects can be used for model testing only when the data are reproducible and the measurement accuracy is controlled. A fruitful approach is to combine improvements in the model with improvements in the experimental procedures, while using the statistical fit of analytical expressions to the data as a basis for testing both the model and the adequacy of the data.

We appreciate the limitations of the present model. Although the two-state model conveys no information concerning the molecular nature or origin of the phase transition, the vibrational spectroscopic data provide a means for directly monitoring structural changes within the lipid bilayer over a large temperature range. The spectroscopic data are thus complementary to the calorimetric data. Moreover, the extraction of thermodynamic information from the spectroscopic studies provides confirmation that the spectroscopic and calorimetric studies are responding to the same phenomena. This aspect is particularly important in the study of lipid systems where sample history influences the manifestation of conformational changes. As the next step in the development of the model, further detail concerning boundary effects between domains should be included along with a variation of the domain size distribution through the phase transition.

With an increased number of parameters in an analytic expression for the phase transition profiles comes a demand for greater data density throughout the phase transition region. We have already indicated the need for decreased temperature intervals. The comparison of temperature profiles obtained from different spectral regions promises to provide extremely useful tests for molecular-scale descriptions of the phase transition and the attendant molecular dynamics.

The course of the research described in this paper was strongly influenced by discussions with Dr. James S. Vincent and Dr. Terrell L. Hill. Their assistance is gratefully acknowledged.

APPENDIX A

Development of an Analytical Expression for Describing the Effect of Temperature on the Spectrum of a Molecular System in Terms of a Two-State Model.

The total Raman scattered intensity I at a particular frequency ν can be expressed as:

$$I_\nu = I_{A\nu} N_A + I_{B\nu} N_B, \tag{A1}$$

where $I_{A\nu}$ and $I_{B\nu}$ represent the scattering intensities per molecule of molecules in each of two states A and B respectively and N_A and N_B are the number of corresponding molecules per scattering volume. The presence of other substances which may contribute to the overall scattering intensity will not affect the derivation that follows, since an expression of the form

$$I_\nu = I_{A\nu} N_A + I_{B\nu} N_B + I_{C\nu} N', \tag{A2}$$

where N' is the number of other scattering molecules, can be rewritten as

$$I_\nu = I_{A\nu} N_A + I_{B\nu} N_B + I_{C\nu} N'(N_A + N_B)/N$$

$$= I'_{A\nu} N_A + I'_{B\nu} N_B. \tag{A3}$$

$I'_{A\nu}$ and $I'_{B\nu}$, as defined, are functions, therefore, of the composition of the sample as well as the intrinsic scattering properties of the molecules of interest in states A and B. The temperature dependence of I_ν, however, will be determined by the temperature dependence of N_A and N_B. The purpose of the following mathematical treatment is to determine an explicit analytical expression for this temperature dependence. And since the treatment deals only with the numbers N_A and N_B, it is also applicable to absorption spectra in concentration ranges where the transmitted intensity or its logarithm is a linear function of concentration; that is, where Beer's Law is obeyed.

We let $\hat{N}_n$ be the number of domains of size n of which $\hat{N}_{nA}$ are in state A and $\hat{N}_{nB}$ are in state B. The number of molecules in states A and B are then

$$N_A = \sum_n n\hat{N}_{nA} \tag{A4a}$$

and

$$N_B = \sum_n n\hat{N}_{nB}. \tag{A4b}$$

In a closed, one-component system in contact with a heat bath at pressure constant pressure p, the differential expression for the internal energy of the system is

$$\mathrm{d}E = T\mathrm{d}S - p\mathrm{d}V + \sum_n \mu_n\hat{N}_n\mathrm{d}n + \sum_n \hat{\mu}_n\mathrm{d}\hat{N}_n \tag{A5a}$$

where

$$\mu_n = (1/\hat{N}_n)(\partial E/\partial n)_{S,\,V,\,\hat{N}_m,\,m} \tag{A5b}$$

and

$$\hat{\mu}_n = (\partial E/\partial \hat{N}_n)_{S,\,V,\,n,\,\hat{N}_m} \tag{A5c}$$

and where m refers to domains of all sizes other than n. The terms $\mu_n\hat{N}_n\mathrm{d}n$ and $\hat{\mu}_n\mathrm{d}\hat{N}_n$ represent a separation of the total chemical potential of the system into two factors: one factor associated with changing the number of molecules in a given domain and the other with changing the number of domains of a particular fixed size. In considering the effects of temperature on the number of domains in state A or state B, processes involving $\mathrm{d}n$ will be excluded. That is, only processes involving $\mathrm{d}\hat{N}_{nA}$ and $\mathrm{d}\hat{N}_{nB}$, where $\mathrm{d}\hat{N}_{nA} = -\mathrm{d}\hat{N}_{nB}$, will be allowed.

The Gibbs free energy G for a system consisting of a mixture of domains of varying but distinguishable size in one of two states, A or B, can then be written as:

$$G = \sum_n \hat{\mu}_{nA}\hat{N}_{nA} + \hat{\mu}_{nB}\hat{N}_{nB} \tag{A6}$$

where

$$\hat{N} = \sum_n \hat{N}_n = \sum_n \hat{N}_{nA} + \hat{N}_{nB} \tag{A7}$$

is the total number of domains in the system and where the chemical potentials $\hat{\mu}_{nA}$ and $\hat{\mu}_{nB}$ are the free energies of domains of size n in states A or B respectively. The condition for equilibrium between states A and B is then:

$$\Delta G = \sum_n \hat{\mu}_{nB} - \hat{\mu}_{nA} = 0. \tag{A8}$$

We define the partition coefficients for the system of domains as:

$$Z = \prod_n Z_{nA}Z_{nB} \tag{A9}$$

where

$$Z_{ni} = \frac{\zeta_{ni}^{\hat{N}i}}{(\hat{N}_{ni})\,!} \tag{A10}$$

and $\zeta\, ni$ is the partition function for a domain of size n in the state i. The chemical potential can also be defined in terms of the Gibbs free energy as:

$$\hat{\mu}_{ni} = (\partial \mathrm{G}/\partial \hat{N}_{ni})_{T,\,p,\,n,\,\hat{N}_{mj}} \tag{A11}$$

and the Gibbs free energy can be expressed in terms of the partition function Z as:

$$G = -kT\ln Z + pV. \tag{A12}$$

Combining equations (A8) through (A12) and invoking Stirling's approximation for the logarithm of factorials gives:

$$\frac{\hat{N}_{nA}}{\hat{N}_{nB}} = \mathrm{e}^{-\Delta G_n^0/kT} \tag{A13}$$

where

$$\Delta G_n^0 = -kT\ln\frac{\zeta_{nB}}{\zeta_{nA}} \tag{A14}$$

is the standard state free energy change for domains of size n. The number of molecules in state A is then given by:

$$N_A = \sum_n n\hat{N}_{nA} = \sum_n \frac{n\hat{N}_n}{1+\mathrm{e}^{-\Delta G_n^0/kT}} \tag{A15a}$$

and in state B by:

$$N_B = \sum_n n\hat{N}_{nB} = \sum_n \frac{n\hat{N}_n}{1+\mathrm{e}^{+\Delta G_n^0/kT}}. \tag{A15b}$$

The temperature dependence of the intensity of a Raman spectral feature, which depends on N_A and N_B, is contained in the terms $\Delta G_n^0/kT$. As defined,

ΔG_n^0 is the difference in free energy between two domains of size n, one in state A and one in state B. For the simplest approximation to this difference, we let $\Delta G_{nA}^0 = n\Delta G_A^0$ and $\Delta G_{nB}^0 = n\Delta G_B^0$ where ΔG_A^0 and ΔG_B^0 are the standard state free energies of individual molecules in states A and B respectively. This approximation is not exact because changes in the free energy of the domains will be affected by the domain boundaries. That is, we have defined the free energy of domains strictly for the internal degree of freedon associated with the order-disorder phase transition of the lipid hydrocarbon chains. The free energy changes associated with this phase transition involve not only intramolecular but intermolecular interactions as well. Individual molecules at the boundaries between domains in different states will possess different intermolecular interaction energies in comparison with molecules within the domains themselves. The factorization of the partition function Z in eq (A9) into a product of single domain partition functions is also one that ignores boundary effects by assuming that the energy of interaction between domains is negligible. ΔG_A^0 and ΔG_B^0 as defined represent an average value of the free energy per lipid molecule for an average domain size. The definition of what constitutes an individual molecular species is flexible. A molecular species could refer to a complete lipid molecule, a single hydrocarbon chain or even a single -CH_2-CH_2-CH_2-triad, the smallest unit for defining a *trans* or *gauche* conformation. The important point is to ensure that the single unit free energy, ΔG_A^0 or ΔG_B^0, is consistent with the definition of that single molecular unit. In the remainder of this discussion, the unit will be taken as a single lipid molecule consisting of two chains.

Substitution of $\Delta G_{n\mathrm{A}}^0 = n\Delta G_{\mathrm{A}}^0$ and $\Delta G_{n\mathrm{B}}^0 = n\Delta G_{\mathrm{B}}^0$ into eq (A15a) yields:

$$N_{\mathrm{A}} = \sum_n \frac{n\hat{N}_n}{1+e^{-n\Delta G^0/RT}}. \qquad \text{(A16)}$$

Note that a molar scale has been adopted for the exponential term so that ΔG^0 is the free energy change per mole of lipid molecules, R is the gas constant, but n retains its definition as the number of molecules per domain. If n is large and if ΔG^0 differs from 0, the exponential value is eq (A16) rapidly approaches 0 or infinity depending on the sign of ΔG^0 and exhibits the discontinuity characteristic of a simple, first order phase transition. For smaller values of n (typically <100), the system exhibits a more continuous transition from state A to state B and can be described in a manner analogous to a two-component system in chemical equilibrium. Since we know from experiment that pure lipid bilayers exhibit sharp phase transitions, we anticipate that n will be sufficiently large to allow expansion of $\Delta G^0/T$ in a power series about $T=T_0$ the temperature at which $N_A=N_B$:

$$\Delta G^0/T = (\Delta G^0/T)\Big|_{T=T_0} + \partial(\Delta G^0/T)/\partial T\Big|_{T=T_0}(T-T_0)$$

$$+ 1/2\ \partial^2(\Delta G^0/T)/\partial T^2\Big|_{T=T_0}(T-T_0)^2. \qquad \text{(A17)}$$

We define the standard state for each domain as the one for which $N_A=N_B$, so that $\Delta G^0=0$ at $T=T_0$. The derivative of $\Delta G^0/T$ with respect to T can be evaluated from the Gibbs-Helmholz equation expressed in terms of differences in partial molar enthalpies; namely,

$$\partial(\Delta G^0/T)/\partial T = -\Delta\bar{H}/T^2 \qquad \text{(A18)}$$

where $\Delta\bar{H}=\bar{H}_B-\bar{H}_A$. From this expression the second derivative of $\Delta G^0/T$ with respect to T can be calculated:

$$\partial^2(\Delta G^0/T)/\partial T^2 = 2\Delta\bar{H}/T^3 - (1/T^2)(\partial\Delta\bar{H}/\partial T) \qquad \text{(A19)}$$

Identifying $\partial\bar{H}/\partial T$ as the molar specific heat at constant pressure, C_p, substituting eqs (A18) and (A19) into eq (A17), and rearranging, the Taylor series expansion of $\Delta G^0/T$ becomes:

$$\Delta G^0/T = -(\Delta\bar{H}/T_0)(T-T_0)/T_0$$

$$+(\Delta\bar{H}/T_0 - \Delta C_p/2)[(T-T_0)/T_0]^2 \qquad \text{(A20)}$$

In general, phase transitions for lipids have been observed to be quite sharp with complete conversion occurring over a range of less than 10 K. Thus, at phase transition temperatures on the order of 300 K, $(T-T_0)/T_0<.03$ for $T-T_0<10$ K. Unless ΔC_p is an order of magnitude larger than $\Delta\bar{H}/T_0$, the second term of eq (A20) can be ignored.

Wilkinson and Nagle have measured the heat capacities of several lipids within 5 K above and below their main phase transitions [17]. As the phase transition temperature is approached from lower temperatures, C_p increases dramatically over the increase in C_p observed for normal alkanes [18]. Above T_0, C_p is higher for the lipid systems than for the alkanes and decreases with increasing temperature. However, ΔC_p does not appear to increase significantly and may actually be lower than the value determined for the solid-liquid phase transitions in alkanes. The anomalously high values of C_p for lipids can be expected to occur when the phase transition is abnormally sharp; namely, over a temperature range of a degree or two where $(T-T_0)/T_0<.005$. Consequently, we assume that the temperature dependence of $\Delta G^0/T$ can be adequately described by the first term in eq (A20).

Substitution of the first term of eq (A20) into eq (A16) gives for the number of molecules in state A,

$$N_A=\sum_n n\hat{N}_n/(1+e^{tn}) \tag{A21}$$

where, for simplicity, we have defined a reduced temperature t as

$$t=(T-T_0)/D=\Delta\bar{H}(T-T_0)/RT_0^2 \tag{A22}$$

and the scale factor D as

$$D=RT_0^2/\Delta\bar{H} \tag{A23}$$

Similarly,

$$N_B=\sum_n n\hat{N}_n/(1+e^{-tn}) \tag{A24}$$

The magnitude of D may be estimated by letting $\Delta\bar{H}\simeq 10$ kcal/mole and $T_0\simeq 330$ K so that $D\simeq 20$ K. For $n=100$ and $T-T_0>1$ K, $N_A<N/100$.

Equations (A21) and (A24) are still too complex to be used for a least squares analysis of the temperature dependence of spectral intensities in the vicinity of a phase transition. The next step in the development is to replace the summations in eqs (A21) and (A24) with some suitable average over the distribution of domain sizes. The distribution of domain sizes is given by $\hat{N}_n$ as a function of n, where $\hat{N}_n$ satisfies the following conditions:

$$N=\sum_n n\hat{N}_n \tag{A25}$$

and

$$\hat{N}=\sum_n \hat{N}_n \tag{A26}$$

and where the moments of the distribution are defined as

$$<n^k>=(1/\hat{N})\sum_n \hat{N}_n n^k \tag{A27}$$

The substitution of $<n>$ into eq (A21),

$$N_A=\hat{N}<n>/(1+e^{t<n>}), \tag{A28}$$

would imply that $<n>^k=<n^k>$ for all k, which would be inaccurate for all but the narrowest of distributions. A better approximation is

$$N_A=\hat{N}<n>/(1+et^{<n^2>/<n>}). \tag{A29}$$

Equations (A28) and (A29) both give the correct asymptotic behavior when compared with eq (A21). Both expressions have inflection points at $t=0$. However, eq (A29) also gives the correct slope at $t=0$, namely $-\hat{N}<n^2>/4$, whereas eq (A28) gives $-\hat{N}<N>^2$.

Since eq (A29) is congruent with eq (A21) at $t=0$ and $\pm\infty$ and since neither eq (A29) nor (A21) has any minima or maxima other than $+\infty$ and $-\infty$, we conclude that eq (A21) may be approximated by a single term, namely

$$N_A=N/(1+e^{tn_{\rm eff}}) \tag{A30}$$

where $N\simeq\hat{N}<n>$ and $n_{\rm eff}\simeq<n^2>/<n>$. Similarly, eq (A24) can be approximated by

$$N_B=N/(1+e^{-tn_{\rm eff}}) \tag{A31}$$

where N and $n_{\rm eff}$ have the same values as in eq (A30) in order to conserve the total number of molecules in the system. In practice, N and $n_{\rm eff}$ will be adjusted to give the best overall agreement between eqs (A30,A31) and (A21,A24).

The accuracy of this single-term approximation can be tested by assuming a distribution function for n and comparing eq (A30) directly with eq (A21). This was done for a set of lognormal distributions as described in the main body of this paper.

Equations (A30) and (A31) can now be used in eq (A1) to describe the intensity of a Raman spectral feature as a function of temperature:

$$I=\frac{I_{A\nu}}{(1+e^t)}+\frac{I_{B\nu}}{(1+e^{-t})} \tag{A32}$$

where, as before, $t=(T-T_0)/D$, but where the explicit reference to $n_{\rm eff}$ has been absorbed into the definition of D, namely,

$$D=(RT_0^2)/\Delta\bar{H}n_{\rm eff} \tag{A33}$$

and where explicit reference to the number density N has been absorbed into the definitions of the scattering intensities $I_{A\nu}$ and $I_{B\nu}$.

APPENDIX B

The Least Squares Fit.

A computer program has been written to analyze the temperature dependence of Raman spectral data by fitting the data by the method of least squares to eq (5). Several features of this program are worth noting. Equation (5) is a linear function of the parameters A, B, a and b and a nonlinear function of T_0 and D. Thus, the parameters of Eq (5) are evaluated using an iterative approach in which r is expanded in a Taylor series for each of the parameters about its currently estimated value. The series is terminated at its linear terms. The values of $r_{obs}-r_{calc}$ are used as the dependent variables and the derivatives of r with respect to each of the parameters as the independent variables. From a linear fit of $r_{obs}-r_{calc}$ to the derivatives of r, the corrections to the parameters are obtained and the process is repeated using the new values of the parameters until the changes in the parameters for each iteration are significantly lower than the standard deviations of the parameters.

The least squares fit is a weighted fit. If we assume that errors in the measured intensities are random, uncorrelated and are drawn from a single, normally distributed population of errors, and if we let s be the estimate of the standard deviation of that population, then the variance of a particular value of an intensity ratio is given by

$$\begin{aligned} s^2(r_{12}) &= (\partial r_{12}/\partial I_1)^2 s^2(I_1) + (\partial r_{12}/\partial I_2)^2 s^2(I_2) \\ &= s^2(1+r_{12}^2)/I_2^2 \qquad \text{(B1)} \end{aligned}$$

where

$r_{12}=I_1/I_2$ and $s^2(I_1)=s^2$. Thus, the errors in the intensity ratios are not normally distributed but instead, depend on the magnitude of r and the intensity in the ratio denominator. Correspondingly, each ratio is given a weighting factor in the least squares fit proportional to the inverse square of its uncertainty, namely,

$$W=I_2^2/(1+r_{12}^2). \qquad \text{(B2)}$$

By setting the proportionality factor to unity rather than $1/s^2$ as suggested by eq (B1), the standard deviation returned by the fit should be a measure of the uncertainty of the Raman intensities. Comparison of the standard deviation of the fit with estimates of the uncertainty in the measured intensities demonstrated that eq (5) is capable of fitting the experimental data to within currently obtained measurement error.

The algorithm for the least squares analysis follows a Gram-Schmidt orthonormalization procedure. This procedure has been extensively tested [19] and a comparison between calculations using single and double precision gave identical results (to the degree of precision reported) indicating that the computation is free from numerical artifacts.

The major problem encountered in the analysis of the temperature profiles is associated with those situations in which the observed data are insufficient to determine the apparent phase transition temperature T_0 and the scaling parameter D. The remainder of this section will deal with those situations.

The parameters T_0 and D are determined solely from those data near $T=T_0$, whereas A, a, B and b are determined primarily by data from the high and low temperature asymptotes of eq (5). The range around T_0 for which D and T_0 can be determined is the range in which r deviates significantly from the asymptotes $A+a(T-T_0)$ and $B+b(T-T_0)$. A deviation is defined as "significant" by the number of standard deviations by which a measured ratio differs from each of the asymptotes. In particular, for a measured ratio to contribute to the determination of D and T_0, we require

$$\left| r_i - \left(A + a(T_i - T_0)\right)\right| > fs/\sqrt{W_i} \qquad \text{(B3a)}$$

and

$$\left| r_i - \left(B + b(T_i - T_0)\right)\right| > fs/\sqrt{W_i} \qquad \text{(B3b)}$$

where r_i is the value of the intensity ratio at the observed temperature T_i. A, a, B, b and T_0 are the values of the parameters determined by the least squares fit; W_i is the weight of the ith datum used in the least squares fit; s is the standard deviation returned by the least squares fit; and f is a multiplicative factor to allow for a more or less stringent test. The quantity, $s/\sqrt{W_i}$, is the estimated uncertainty in the experimental value of the i^{th} ratio. Equations (B3a,b) state that for the purpose of contributing to the evaluation of T_0 and D the value of an observed ratio must differ from both asymptotic limits by an amount greater than some multiple f of the expected measurement uncertainty at that temperature. If the conditions of eqs (B3a,b) are met, we say that a measurement falls within the transition interval. Equations (B3a,b) define the temperature interval; the number of experimental data falling within this interval determines the reliability with which D and T_0 can be estimated. In particular, the number of data falling within this interval is the appropriate number to use in calculating the number of degrees of freedom for the estimation of confidence intervals from a student's t distribution.

If no measured temperature falls within the transition interval, neither T_0 nor D can be estimated by a least squares fit of the data to eq (5). If one measured value falls within the interval, only T_0 can be estimated, but not D. Furthermore, the value of the uncertainty in T_0 returned by the least squares fit must be multiplied by a factor of 12.7, the value of t from the student's t distribution for one degree of freedom and confidence limits of 95%. If two measured values fall within the interval, both T_0 and D can be estimated, but the estimates of their uncertainties must be multiplied by 4.3, the value of t from the student's t distribution appropriate for two degrees of freedom. Should more than two measured values fall within the transition interval, T_0 and D can be determined with increasing reliability.

When less than two points fall within the transition interval, bounds can be placed on the values of T_0 and D, even though T_0 and D cannot be determined precisely. In order to place bounds on T_0 and D, bounds must be placed on the transition interval. The transition interval can be estimated by combining eqs (B3a,b) with eq (5) to give, ignoring terms in a and b,

$$T_x = F_x D,$$

where

$$F_x = 2\ln\left(\left|B-A\right|\frac{\sqrt{W}}{fs}-1\right) \qquad \text{(B4)}$$

and W is the average weight of a measured value in the vicinity of the phase transition temperature. The transition interval T_x is the temperature interval over which r varies from $A+a(T-T_0)\pm fs/\sqrt{W}$ to $B+b(T-T_0)\mp fs/\sqrt{W}$, where the upper sign is chosen if $A<B$ and the lower sign if $B<A$.

If no measured temperature falls within the transition interval, as tested by eqs (B3a,b), we know that

$$0<T_x<T_d \qquad \text{(B5)}$$

where T_d is the temperature interval between the successive data pair above and below the phase transition temperature. Thus, from eq (B4)

$$0<D<T_d/F_x. \qquad \text{(B6)}$$

In calculating the value of A, a, B and b, D is held fixed at its average value in the range defined by eq (B6); namely

$$D=T_d/2F_x, \qquad \text{(B7)}$$

and T_0 is given as the midpoint between the two measured temperatures spanning the phase transition interval. Depending on the precision of the Raman intensity measurements relative to the difference between A and B, F_x typically varies from 2 to 9. Most of the time a value of $f=2$ is used in eqs (B3a,b) and (B4). Substitution of $\Delta T=4D$ into eq (B6) yields

$$\Delta T=4RT_0^2/(\Delta\bar{H}n_{\mathrm{eff}})<4T_d/F_x \qquad \text{(B8a)}$$

and

$$n_{\mathrm{eff}}>F_xRT_0^2/(\Delta\bar{H}T_d). \qquad \text{(B8b)}$$

If one measured temperature T_i falls within the transition interval,

$$0<T_x<2T_d, \qquad \text{(B9)}$$

where $2T_d=T_i+1-T_i-1$ is twice the average data interval of the three measured temperatures spanning the transition interval. As with the case of no measured temperature falling within the interval, D is assigned the average value implied by the range of eq (B9); namely,

$$D=T_d/F_x, \qquad \text{(B10)}$$

and ΔT is reported as

$$\Delta T<8T_d/F_x. \qquad \text{(B11)}$$

T_0 is estimated by the least squares fit of all the data to eq (5) but is determined, almost exclusively, by the value of r at T_i relative to A and B.

References

[1] For a recent review, see Levin, I. W. In Adv. in Infrared and Raman Spectroscopy, **11**, eds. R. J. H. Clark and R. E. Hester, pp. 1–48. New York: Wiley Heyden (1984).

[2] Steer, C. J.; J. S. Vincent and I. W. Levin, J. Biol. Chem. **259** 8052–5 (1984).

[3] Nagle, J. F., Ann. Rev. Phys. Chem. **31** 157–195 (1980).

[4] Israelachvili, J. N.; S. Marcelja and R. G. Horn, Quart. Rev. Biophys. **13** 121–200 (1980).

[5] Albon, N., and J. M. Sturtevant, Proc. Natl. Acad. Sci. U.S.A. **75** 2258-6 (1978).

[6] Hill, T. L., Thermodynamics of Small Systems, pp. 89–133. New York: W. A. Benjamin, Inc. (1963).

[7] Dluhy, R. A.; D. Moffatt, D. G. Cameron, R. Mendelsohn, and H. H. Mantsch, Can. J. Chem. **63** 1925–32 (1985).

[8] Zimm, B. H., and J. K. Bragg, J. Chem. Phys. **31** 526–35 (1959).

[9] Kendall, M. G., and A. Stuart, The Advanced Theory of Statistics, vol. I, pp. 168–73. New York: Hafner Publishing Co. (1969).

[10] Sturtevant, J. M., Proc. Natl. Acad. Sci. U.S.A. **79** 3963–7 (1982).

[11] Sturtevant, J. M., Ann. Rev. Biophys. Bioeng. **3** 35–50 (1974).

[12] Kirchhoff, W. H.; A. J. Hancock and I. W. Levin, Biophysical Journal **45**:196a (1984).

[13] Singer, M. A.; M. K. Jain, H. Z. Sable, H. J. Pownall, W. W. Mantulin, M. D. Lister, and A. J. Hancock, Biochim. Biophys. Acta **731** 373–7 (1983).

[14] Huang, C.; J. R. Lapides and I.W. Levin, J. Amer. Chem. Soc. **104** 5926–30 (1982).

[15] Freire, E., and R. Biltonen, Biochim. Biophys. Acta **514** 54–68 (1978).

[16] Marsh, D.; D. Watts and P. F. Knowles, Biochim. Biophys. Acta **465** 500–14 (1977).

[17] Wilkinson, D. A., and J. F. Nagle, Biochim. Biophys. Acta **688** 107–15 (1982).

[18] Finke, H. L.; M. E. Gross, G. Waddington, and H. M. Huffman, J. Am. Chem. Soc. **76** 333–41 (1954).

[19] Wampler, R. H., J. Res. Natl. Bur. Stds. **73B** 59–90 (1969).

Journal of Research of the National Bureau of Standards

Free-Field Reciprocity Calibration Of Microphones

Volume 92 Number 2 March–April 1987

Edwin D. Burnett,
Victor Nedzelnitsky

National Bureau of Standards
Gaithersburg, MD 20899

Standardized methods for the primary free-field calibration of laboratory standard microphones deal with Type L (ANSI S1.10-1967, R1977) "one-inch" diameter microphones. However, the use of "1/2-inch" diameter microphones for measurement of the sound pressure level in acoustic fields is increasing. Consequently, the NBS has developed a fixed-cost measurement service for the free-field calibration of these microphones by the reciprocity method over the range 2.5 kHz to 20 kHz. For this service, the apparatus and procedures, including essential properties of the anechoic chamber in which the calibrations are performed, are described. Opportunities for improvements are noted. The frequency-dependent positions of the apparent acoustic centers of the microphones were obtained. The overall uncertainty estimate for free-field calibration, expressed as the sum of the magnitude of credible bounds on the systematic component (s) and the random component (2σ, where σ is the standard deviation) is 0.16 dB or better (s=0.06 dB, 2σ=0.10 dB) at frequencies 1.25 kHz $<f<$ 5 kHz, and 0.07 dB or better (s=0.02 dB, 2σ=0.05 dB) for 5 kHz $<f<$ 20 kHz. Comparison for given microphones of the measured difference between free-field and pressure response levels with the difference calculated by diffraction theory (derived by Matsui) indicates agreement of 0.16 dB or better in the low-frequency range (1.25 kHz to about 4 kHz) where free-field reciprocity measurements encounter the greatest experimental difficulties. This agreement is consistent with the estimated uncertainties of free-field and pressure calibration by the reciprocity method.

Key words: acoustic calibrations; acoustic measurements; anechoic chamber measurements; calibration; free-field microphone calibration; metrology; microphone calibration; plane-wave free-field acoustic measurements; reciprocity calibration methods; standards: acoustical; traceability: acoustical measurements; transducer calibration (reciprocity).

Accepted: December 24, 1986

1. Introduction

The two different electroacoustical responses (sensitivities) that are most frequently requested of the microphone calibration services at the National Bureau of Standards (NBS) are the pressure response (pressure sensitivity) and the free field response (free-field sensitivity). Both are usually expressed in terms of the ratio of the open-circuit voltage (at the output of the microphone) to a sound pressure in the acoustic field in which the microphone is located, for a given frequency of excitation in the sinusoidal steady state (units: V/Pa).

Throughout this paper, the voltages, currents and sound pressures are the rms (root-mean-square)

About the Authors: Edwin D. Burnett, a physicist, and Victor Nedzelnitsky, an electrical engineer, are with the NBS Center for Manufacturing Engineering, serving with the Acoustic Measurement Group in the Center's Automated Production Technology Division.

values of the sinusoidal quantities. Although these quantities will in general have phase differences between them, such differences do not figure in standardized calibration by the reciprocity method. Calibration for phase response by this method is a subject for further research and standards yet to be determined.

At a given frequency in the sinusoidal steady state, the pressure response is the ratio of the output voltage of the microphone to the sound pressure uniformly distributed over the exterior surface of the microphone diaphragm. The pressure response is generally determined using the reciprocity technique and acoustic couplers essentially enclosing a coupling cavity into which the microphone diaphragms are introduced. The pressure response is needed for measurement of the sound pressure level in cavities or couplers, as in the calibration of audiometric and other earphones and many types of acoustic calibrators.

At a given frequency in the sinusoidal steady state, the free-field response is the ratio of the output voltage of the microphone to the sound pressure which existed at the microphone's acoustic center (or specified reference point) prior to the introduction of the microphone into the path of a plane progressive sound wave. The direction of propagation of this wave has a specified orientation with respect to the principal axis of symmetry of the microphone, and for the most precise laboratory standards purposes is usually chosen parallel to this axis, so that the direction of propagation is perpendicular to and toward the diaphragm surface of the microphone. This orientation is usually termed normal incidence. The free-field response differs from the pressure response due to diffraction effects associated with the relation between the wavelength of sound and the physical dimensions of the microphone and its mounting, with the difference becoming large at frequencies sufficiently high that a wavelength becomes comparable to or smaller than these dimensions. For practical laboratory standard microphones, these diffraction effects are sufficiently large at frequencies of interest that free-field calibrations are needed for the most accurate acoustical measurements under free-field conditions.

Currently applicable standardized laboratory methods for the primary free-field calibration of 1-inch nominal diameter laboratory standard microphones (hereafter termed "1-inch" microphones; their actual diameter is about 0.936 inch or 23.77 mm) by the reciprocity method have been available for over a decade. However, many of the microphones used for precision acoustical measurements have a nominal diameter of one-half inch (hereafter termed 1/2-inch microphones; the actual diameter at the mounting base is about 0.500 inch or 12.7 mm). Such microphones are usually used for determining the sound pressure level (SPL) in acoustic fields, rather than in cavities or couplers. The use of the smaller size microphones can be expected to increase with the availability of 1/2-inch microphones which are as sensitive as those of the "1-inch" size. Thus, the capacity to perform free-field reciprocity calibrations for 1/2-inch microphones has been added to the NBS fixed-cost microphone calibration services. Refinements in electronic instrumentation, apparatus, and procedure have enabled these services to attain accuracies comparable to or better than those that had been achieved at NBS for calibration of "1-inch" microphones. The purpose of this paper is to describe the methods, apparatus, procedures, and uncertainties associated with the free-field reciprocity calibration of 1/2-inch microphones at NBS.

2. Method

The theory for reciprocity calibrations using harmonic excitation has been well developed [1–5][1] and appears in both a domestic (ANSI) standard [3] and an international (IEC) standard [5]. This theory will not be repeated in depth here. An extensive bibliography is found in reference [3]. Briefly, three microphones are used for a calibration. The procedure of specific measurements performed on the three microphones can be chosen either to determine the sensitivities of all three microphones, in which case we denote the procedure as the "three-microphone method," or to determine the sensitivities of two of the three microphones with the third microphone used only as a source, in which case we denote the procedure as the "two-microphone method."

For the three-microphone method, the microphones are used sequentially as source and receiver. At each frequency of interest for each of the three sequentially performed measurements, the ratio of the receiver output voltage to the source input current is determined. These results are combined with reciprocity theory and the values of other pertinent parameters of the method to determine the free-field sensitivities of the three microphones.

For the two-microphone method, the ratio of the receiving output voltage from each of the two microphones being calibrated to the voltage applied to the third microphone driven to act as a sound

---

[1] Bracketed figures refer to literature references.

source is measured sequentially; first, for one receiving microphone at all frequencies of calibration, next, for the other receiving microphone, after it has been substituted for the first receiving microphone. These ratios are then combined to determine, at each frequency of interest for a given free-field sound pressure, the ratio of the output voltages of the two microphones being calibrated. This ratio effectively determines the ratio of the sensitivities of these two microphones. One of these microphones is then used as the receiver and the other as the source, and the ratio of the receiver voltage to source drive current is determined. This ratio is combined with the ratio of sensitivities, reciprocity theory, and the values of other pertinent parameters of the method to determine the sensitivities of the two microphones being calibrated.

The techniques used by the NBS will be introduced by first considering the formulas from which the microphone sensitivities are determined from the measurements for the three-microphone method and the two-microphone method given in reference [5]. Using the notation of reference [3], when applicable, the three-microphone method yields the following equation for the magnitude of the sensitivity of the microphone (a):

$$|M_{fa}| = \left\{ \frac{2}{\rho_o f} \frac{r_{ab} r_{da}}{r_{bd}} \frac{|e_b/i_a| \cdot |e_a/i_d|}{|e_d/i_b|} \exp\left[\alpha(r_{ab} + r_{da} - r_{bd})\right] \right\}^{1/2} \tag{1}$$

where $r_{xy}(x,y = \text{a,b,d})$ is the distance between the acoustic centers (as defined in reference [3]) of microphone x and microphone y, f is the driving frequency, i_y is the complex amplitude of the driving current through microphone y, e_x is the complex amplitude of the output voltage of microphone x, α is the attenuation coefficient of sound in air at frequency f, and ρ_o is the ambient density of air. For the two-microphone method the magnitude of the sensitivity of microphone (a) is given by

$$|M_{fa}| = \left[\frac{2}{\rho_o f} r_{ab} \, |e_b/i_a| \cdot |e_a/e_b| \, \exp(\alpha r_{ab}) \right]^{1/2} \tag{2}$$

We first consider the merits of each of these methods. If three microphones are being calibrated at the same time, the three-microphone method gives directly the sensitivities for all three microphones. However, the two-microphone method gives a result which, for a given expenditure of labor and cost of apparatus, is more accurate in many practical cases. With this method only one measurement of current, which involves measurement of microphone driving-point electrical impedance (sometimes expressed in terms of the microphone capacitance) in our technique [4], is required instead of three. The uncertainty due to error in this particular portion of the measurement is reduced. Significant advantage is found when measuring the output of two conventional, low-sensitivity (i.e., with response levels of about −38 dB re 1V/Pa, as distinguished from high-sensitivity, with response levels about −26 dB re 1V/Pa) 1/2-inch microphones. The magnitude ratio of the output voltages of the two microphones [$|e_a/e_b|$ in eq (2)] can be determined using a high-sensitivity 1/2-inch microphone or a "1-inch" microphone as the source. With either of these microphone types, the SPL will be more than 10 dB higher over most of the frequency range than it otherwise would be for two of the three required output level determinations. This higher SPL produces a higher signal-to-noise ratio which gives a better calibration accuracy at the lower frequencies of calibration (for which the signal-to-noise ratio is lower) and reduces the time required for making the measurement by reducing the signal processing time required to reduce uncertainty introduced by the noise. The two-microphone method will be discussed throughout the remainder of this report.

Accurate methods and apparatus for deriving the calibration, using attenuator settings to determine the ratios of the source voltages to the receiver voltages and the driving-point electrical impedance of the source (reversible) microphone (which is derived from an attenuator setting and a known resistance) have been described [3,4]. Specific adaptation of these methods to free-field measurements and a description of the apparatus employed at the NBS are provided in section 3 of this paper.

Using eq (2) and its counterpart for $|M_{fb}|$ [3,5], the equation for the response level R_{fx} $(x = \text{a,b})$ in dB re 1V/Pa can be expressed as

$$R_{fa} = 20 \log_{10}[M_{fa}/(1\text{V/Pa})] = \tfrac{1}{2}[A_{bd} - A_{ad} - A_{ba}] + D_o \text{ db re 1V/Pa} \tag{3}$$

$$R_{fb} = 20 \log_{10}[M_{fb}/(1\text{V/Pa})] = \tfrac{1}{2}[A_{ad} - A_{bd} - A_{ba}] + D_o \text{ db re 1V/Pa} \tag{4}$$

where

$$D_o = 10\log_{10}\left[\frac{r_{ab}T}{p_s C_a f^2}\right] + 4.343\,\alpha\, r_{ab} + 19.605 \qquad (5)$$

r_{ab} is the distance in meters between the acoustic centers of microphones (a) and (b)

p_s is the barometric pressure in pascals

T is the absolute temperature in kelvins

$$C_a = \frac{1}{2\pi f|Z_a|}\,. \qquad (6)$$

where $|Z_a|$ is the magnitude of the driving-point electrical impedance of the reciprocal microphone (used as a sound source) in ohms.

The quantities A_{xy} (x = a,b, y = a,d), which are attenuator settings of the calibration apparatus in decibels, are defined in section 3.1.

The accuracy of the calibration can be improved by reversing the functions of the microphones (a) and (b), taking the second set of measurements, and averaging the results of these two sets.

3. Apparatus

3.1 Block Diagram

The block diagram of the electronic instrumentation is shown in figure 1. The applied sinusoidal signal from the oscillator will take one of two paths, depending upon the setting of the switch, S1. The details of the switch are shown in figure 2. When S1 is set to position "S," the drive signal is applied to the source microphone. The sound generated by the source microphone is picked up by the receiving microphone and preamplifier, amplified by the measuring amplifier, and then detected by the lock-in amplifier and indicated by the digital voltmeter. When the switch is set to position "A," the signal is electrically applied through the attenuator so that the output of the attenuator acts as a voltage source in series with the electrical terminals of the receiving microphone. The electrical path following the receiving microphone remains the same. The precision attenuator, which can be

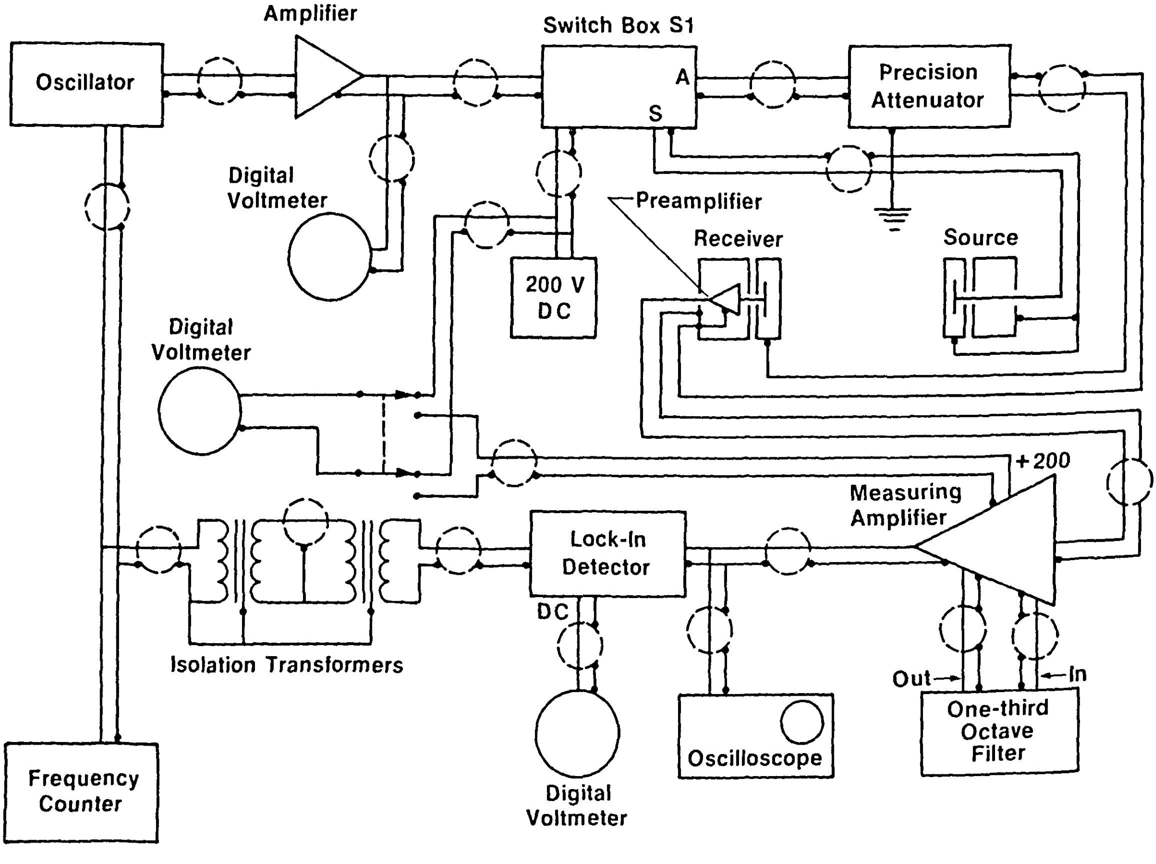

Figure 1-Block diagram of the equipment used for the free-field calibration of microphones.

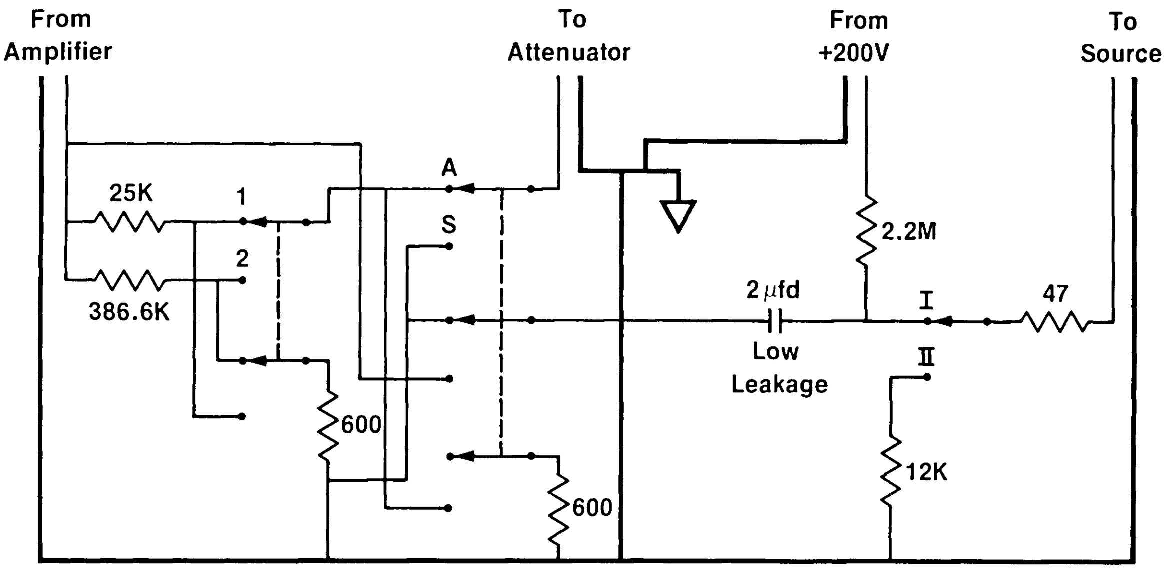

1	32.61 dB	A	Attenuator	I	Source On
2	56.36 dB	S	Source	II	Source Off
Fixed Attenuation Switch		Mode Switch		Source Switch	

Figure 2–Switch box, showing nominal resistance values and measured values of attenuation.

incremented in steps of 0.01 dB, is adjusted so the output voltage as detected by the lock-in amplifier is the same for the two switch settings. The reading of the attenuator, therefore, expresses the ratio of the source drive voltage to the receiver microphone output voltage. This quantity is denoted A_{xy} (x =a,b; y =a,d) in eqs (3) and (4), where x and y refer to the receiving and source microphones, respectively. Using this method, it is not necessary to know the absolute values of the drive and receiving voltages. The source switch (fig. 2) is left in position I when making measurements, and is turned to position II (Source Off) when removing or attaching the source microphone.

3.2 Synchronous Detector

The transmitting microphone acts as a very small single-sided electrostatic loudspeaker unit (although with a stiff diaphragm having a very high fundamental resonance frequency). Consequently, the drive voltage should be small relative to the applied dc polarizing voltage for the unit to behave as an essentially linear transducer [6], as well as to avoid ionization breakdown of the air between the diaphragm and backplate and potentially excessive stress within the diaphragm itself. The largest value of ac drive voltage used at the NBS is 10 volts rms. This limits the sound pressures, and therefore voltages, developed at the receiving microphone during calibration to rather low values, especially at the lower frequencies of calibration. For example, with many widely used 1/2-inch precision condenser microphones as both the transmitter and receiver, separated by a distance of 20 cm, the output voltage at the receiving microphone at 1500 Hz is of the order of one microvolt. The attenuation relating receiver output voltage to transmitter drive voltage is approximately 140 dB for these conditions, and signal-to-noise ratio of the measurements is a critical problem at the lower frequencies of calibration.

In order to obtain an adequate signal-to-noise ratio from the output of the receiving microphone narrow-band filters or signal averaging techniques must be used. A self-tuning lock-in amplifier makes a particularly convenient type of filter because of its narrow, but adjustable, bandwidth and its ability, when provided with a suitable reference signal phase-locked to the calibration signal, to track this calibration signal automatically.

Because of the use of the insert-voltage method to obtain accurate measurements that are relatively insensitive to many of the specific characteristics of the electronic instruments that are used in the apparatus (see sec. 2.1 of ref. [3] and the switching arrangement in fig. 1), the phases of the signals sequentially produced at the output of the receiving microphone by the driven source microphone and by the inserted attenuator signal usually will not be the same with respect to the reference signal from the oscillator. Use of the insert voltage method, however, requires that the amplified and filtered (or otherwise detected) outputs of the microphone be equal in magnitude whenever these sequentially produced microphone output signals are of equal magnitude. Consequently, for a given magnitude of input signals, the voltage magnitude detected and indicated by the lock-in amplifier must be essentially independent of the relative phase of its input and reference signals.

Some commercially-available units achieve this essential independence by shifting the phase of the reference signal to match that of the input signal. In any event, since a specification for the degree of such independence is not normally included in manufacturers' specifications of lock-in amplifier performance, it is necessary to measure this degree of independence before using a lock-in amplifier as shown in figure 1. The lock-in amplifier used was found to have (for a given magnitude of input signal) an output independent, within 0.01 dB, of the relative phase of the input and reference signals, and was therefore considered to be a satisfactory detector for the amplified, band-pass filtered, A-weighted (to reduce low-frequency noise) output of the receiving microphone. Time constants typically ranging from 0.3 to 30 s, and occasionally to 100 s, are used when making measurements. With the longest time constant, (100 s) long-term drift in the system of figure 1 can reduce the accuracy of measurements. The time constant determines the bandwidth of the detector and, therefore, the lowest signal levels that can be measured to the desired accuracy for a given signal-to-noise ratio at the input, provided that the dynamic reserve capability of the lock-in amplifier is not exceeded (i.e., provided that this amplifier is not significantly influenced by noise or Fourier components of the input signal that lie outside the passband). The A-weighting and one-third-octave band-pass filtering prior to the input of the lock-in amplifier eliminate harmonic Fourier components to which the lock-in detector might otherwise respond and ensure that the lock-in amplifier is operated within its dynamic reserve capability.

3.3 Grounding

Although the grounding procedures used are straightforward, they must be carefully followed since the magnitude of the crosstalk voltage must be less than 0.1 percent of the signal voltage magnitude for the error in signal measurement to be less than 0.01 dB. A seemingly slight variation in the grounding procedures can produce a crosstalk level that is higher than the desired signal. The ground connections and signal leads are shown in figure 1. The ground is carried through by only one path. A problem arises because the lock-in amplifier has two inputs, one for the signal and one for the reference. The signal path to the reference channel, therefore, uses two audio-frequency transformers in cascade for isolation of the ground. (One transformer did not give sufficient isolation, presumably because of capacitive feedthrough.) Each piece of equipment has the power ground broken by means of three-pin to two-pin adaptors at the connection to the power line. For considerations of safety, the entire system is grounded to earth at the attenuator panel, although connecting this ground makes no difference in the crosstalk level.

3.4 Preamplifier and Microphone Ground Shield

The preamplifier is a modified version of a commercially-available device (Bruel and Kjaer Type 2619)[2] commonly used with 1/2-inch microphones. The heater has been removed to prevent thermal gradients and atmospheric convection from influencing either the microphone or the sound transmission path between transmitter and receiver, and thus affecting the measurements. The center connector shield has been grounded, and a plastic insulating ring has been installed so that the microphone cartridge body shell can be connected to a shielded lead that is used to provide the insert voltage. The geometry of the center pin shield has not not been changed. Figure 3 shows the ground-

---

[2] This item is identified only in order to adequately specify the apparatus, and such identification in no way implies that this item is the best or the only commercially available device that could be used for the intended purpose.

shield and other key dimensions of the modified preamplifier without electronics. The preamplifier is coaxially mounted on a hollow rod of 12.7 mm (1/2-in) external diameter.

3.5 Transmitter

The transmitter to which the source microphone is connected is mechanically identical (with regard to key dimensions A through J) to the preamplifier. Instead of the preamplifier, a shielded lead is connected to the center pin that contacts the center conductor of the microphone. The electrical connection to the microphone body is effected by means of a shielded lead so the driving-point electrical impedance of the microphone can be measured *in situ*. Figure 3 shows the key dimensions of the transmitter assembly. The transmitter is also coaxially mounted on a hollow rod of 12.7 mm diameter.

3.6 Mounting

The rods supporting the preamplifier and transmitter are passed through bearings on opposite walls of a small anechoic chamber. The rod supporting the transmitter is normally fixed in one position. The rod supporting the preamplifier is attached to

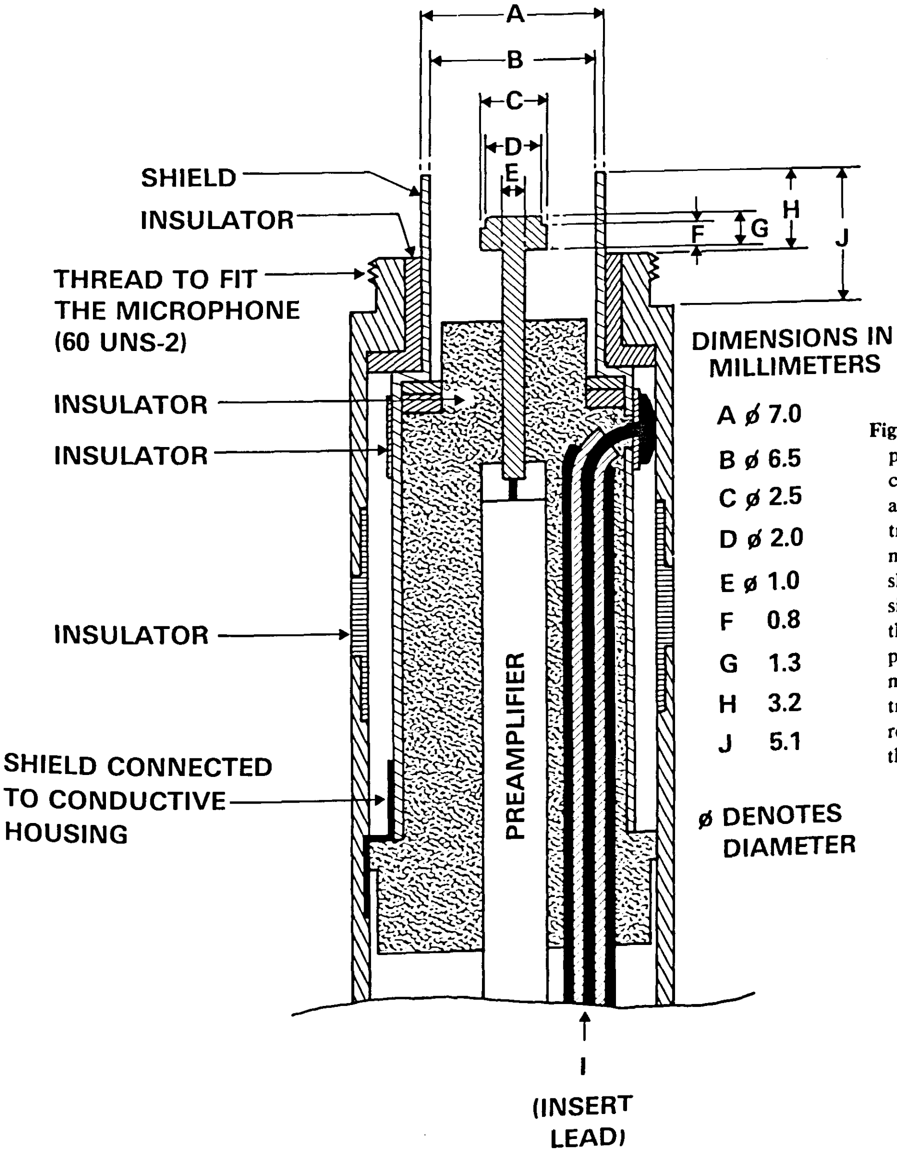

Figure 3–Cross section of the preamplifier to which the receiving microphone is attached, and the assembly on which the transmitting microphone is mounted, showing ground-shield and other key dimensions. The dimensions A through J are the same for the preamplifier and transmitting microphone assembly. In the transmitter, the preamplifier is replaced by a shielded lead to the center contact pin.

a screw-driven mechanical slide with a line-scale position indicator, external to the chamber. This arrangement allows the receiving microphone to be placed at any desired distance up to 31 cm from the source microphone, with a repeatability in position of about 0.1 mm.

3.7 Anechoic Chamber

The tests are performed in a chamber with a width of 2.1 m, a height of 1.6 m and a depth of 1.6 m between wedge tips (free volume of 5.4 m^3). The fiberglass wedges are 0.3 m deep. The chamber is single-walled but the use of a one-third-octave band-pass filter, A-frequency weighting in the measuring amplifier, and a lock-in amplifier for the detection of the signal provides adequate rejection of ambient noise. The chamber is located in a quiet, windowless control room that is separated from the rest of the NBS Sound Building by reinforced concrete walls approximately one foot (0.3 m) thick. This room is located in the most quiet part of the building, as far as possible from mechanical HVAC equipment at the opposite end of the building. The chamber rests on elastomeric blocks on the floor of this control room; these blocks provide vibration isolation from the floor.

4. Acoustic Center

The virtual locations of the source and receiving microphones are usually not at the diaphragms of the microphones but at some nearby positions known as the acoustic centers. No general analytic procedure exists for the determination of the location of the acoustic centers. An empirical method is used in this paper, based on [3] and [5]. At low frequencies and at distances commonly used in free-field calibration by the reciprocity method, these positions are in front of the diaphragm of each microphone, i.e., outside its exterior surface. A determination of the positions of the acoustic centers was obtained using the inverse relationship between the amplitude of the sound pressure at the receiving microphone and the distance between the acoustic centers of the source and receiving microphones. Data were obtained by holding the source microphone at a fixed position and varying the position of the receiving microphone for grid-to-grid separations ranging from 1 cm to 31 cm. The attenuator settings in decibels for a specified drive voltage were recorded and thus constituted relative levels at the receiving microphone. Each level was converted to relative amplitude and a correction was made for the absorption of sound by the atmosphere [7]. In order to account for the inverse relation between amplitude and grid-to-grid spacing, the amplitude for each position was normalized by multiplying it by the grid-to-grid spacing for that position. If the correction for atmospheric absorption were exact, if the acoustic centers were at the grid of each microphone, if the microphones had been within each other's far field only (i.e., with no near-field component, however small), and if the acoustical environment had been perfectly anechoic, then the normalized amplitudes for a given frequency would all have the same value. In the discussion which follows, only data from separations of 10 cm to 31 cm are considered, so that amplitude values only from positions at which the sound pressure was dominated by the far field of the microphones are used (it does not necessarily follow, however, that the near-field component was negligible at all frequencies). For purposes of presentation, the normalized data, shown in figure 4 at a typical frequency of 4005 Hz, are converted back to level. These values of level are not identical, although the differences are not large.

The normalized amplitude data were then evaluated by a first-order polynomial regression procedure which performed a least-squares fit of a straight line to the data shown in figure 4. This fit was done on a desktop computer (Hewlett-Packard 9836C, using regression analysis software contained in HP part no. 98820-13618). Had the above conditions been met, and had the acoustic centers been at the microphone grids, the data set would have a slope of value zero, and the coefficient of the first order term in the polynomial regression

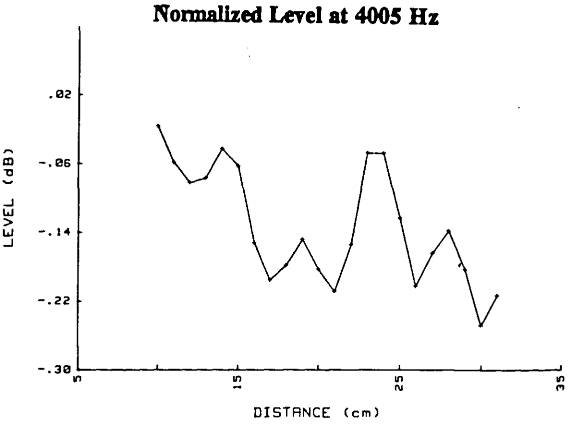

Figure 4–Deviations in level from an inverse distance relationship for the normalized (with respect to grid-to-grid separation distance) and corrected (to remove effects of atmospheric absorption of sound) data of two high-sensitivity, e.g., −26 dB re 1V/Pa, 1/2-inch microphones at 4005 Hz. The abscissa is grid-to-grid separation distance.

would have been zero. Such was not the case. The constant term and the first-order coefficient produced by the regression for 4005 Hz are:

constant term = 0.20113 dB
1st order coefficient = −0.00015 dB/cm

Such slight departures from zero slope are also typical of the data at frequencies other than 4005 Hz.

The distance corrections due to the virtual locations (apparent acoustic center positions) of the source and receiving microphones were determined and incorporated into the relative amplitude data (corrected as before for atmospheric absorption of sound) at each frequency by:

1) multiplying each relative amplitude datum obtained at the given frequency by $(d+\Delta d)$, where d is the physical separation between microphone grids (grid-to-grid distance) for that datum and Δd is a trial correction for the spacing between microphones due to the apparent acoustic center positions at that frequency.
2) replotting on a CRT display each datum above with abscissa $(d+\Delta d)$ and reapplying the first-order polynomial regression to the data for this frequency and,
3) iterating steps 1) and 2) above on the desktop computer for different values of Δd until the value of the first order coefficient (and consequently the slope of the plotted line) was essentially zero. The value of Δd corresponding to this zero slope condition was then considered a measure of the distance correction at that frequency for the range of distances represented in the data. The data corresponding to this zero slope condition were then renormalized by division by the value of the constant term in the regression corresponding to this zero slope condition, and consequently also corresponding to the final distance correction. These renormalized data are hereinafter referred to as the "renormalized amplitude data," and, when converted to level and plotted, as the "renormalized data converted to level," the "renormalized data," or the "level renormalized for measured grid-to-grid correction."

Since two microphones of the same type were used as the transmitter and receiver, the displacement of the acoustic center from the grid is considered to be one-half the amount of the distance correction, with a negative value indicating the displacement is away from the microphone; i.e., outside the exterior surface of its protection grid.

The corrections for the spacing between the two microphones at various frequencies are shown in the second column of table 1. In order to obtain distance corrections which are a smoother function of frequency than these (hereinafter referred to as the "measured corrections") obtained directly from the measured data, these corrections are them-

Table 1. Grid-to-grid corrections for distance.

Freq.	Grid-to-Grid Correction Meas-ured	Grid-to-Grid Correction 2nd Order Fit	Effect of Measured Correction @20 cm	Effect of 2nd Order Fit Correction @20 cm	Effect of Measured Correction @15 cm	Effect of 2nd Order Fit Correction @15 cm
Hz	cm #	cm #	dB •	dB •	dB •	dB •
1001	−0.70	−0.52	0.31	0.23	0.42	0.31
1251	−0.14	−0.51	0.06	0.22	0.08	0.30
1602	−0.52	−0.49	0.23	0.22	0.31	0.29
2003	−0.46	−0.47	0.20	0.21	0.27	0.28
2503	−0.61	−0.45	0.27	0.20	0.36	0.26
3153	−0.52	−0.42	0.23	0.18	0.31	0.25
4005	−0.26	−0.39	0.11	0.17	0.15	0.23
5005	−0.44	−0.35	0.19	0.15	0.26	0.21
6308	−0.34	−0.30	0.15	0.13	0.20	0.18
8009	−0.21	−0.23	0.09	0.10	0.12	0.13
9987	−0.05	−0.17	0.02	0.07	0.03	0.10
12475	−0.14	−0.08	0.06	0.03	0.08	0.05
15968	0.01	0.02	0.00	−0.01	−0.01	−0.01
19973	0.12	0.12	−0.05	−0.05	−0.07	−0.07

The acoustic center correction for a microphone, referred to the grid, is one-half of the grid-to-grid distance correction. A negative number indicates that the acoustic center is in front of (outside) the exterior surface of the grid.

• The error in a calibration response level produced by the error in level (if uncorrected for acoustic center positions) at the receiving microphone at a given distance and frequency will be one-half of the error in the measured level shown in this table.

selves subjected to a second-order polynomial regression process. The resulting smoothed values (hereinafter referred to as the "second-order fit corrections") are shown in the third column of table 1. Table 1 also shows the resulting calculated changes in level at two specific distances which occur because the acoustic center is not at the grid of the microphones. Specifically, the fourth column gives the changes which would occur for a grid-to-grid spacing of 20 cm if the acoustic centers are assumed to be at the positions given by the measured corrections, rather than at the microphone grids. The fifth column gives the changes in level which would occur if the acoustic centers are assumed to be at the positions given by the second-order fit corrections. The last columns repeat these calculations for a grid-to-grid spacing of 15 cm.

Figures 5–18. show the plots over the range 1 kHz–20 kHz for the renormalized data with the amplitudes converted to level. Clearly, even

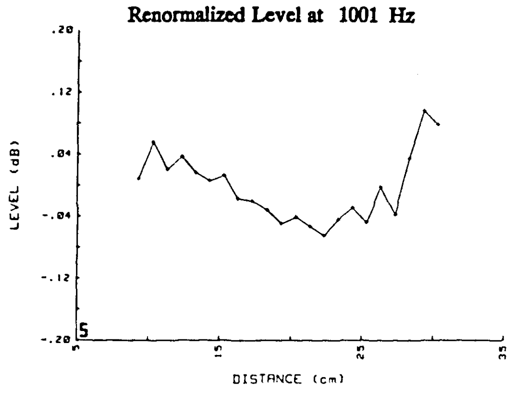
Renormalized Level at 1001 Hz

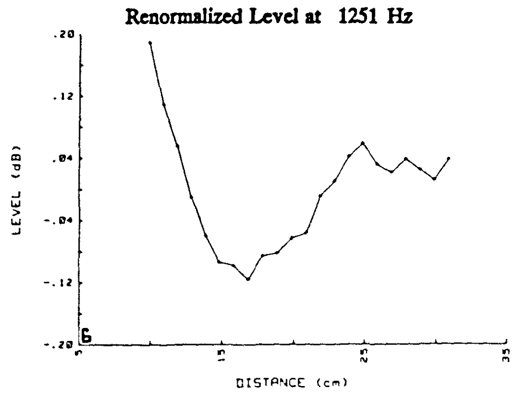
Renormalized Level at 1251 Hz

Figure 5-18–Deviations in level from an inverse distance relationship for data such as those in figure 4, but renormalized (with respect to separation distance corrected for the calculated acoustic center positions). Each figure shows data at a different frequency in the range from 1 kHz to 20 kHz. All data shown are from high-sensitivity 1/2-inch microphones. The abscissa is the sum of the grid-to-grid separation distance and the measured grid-to-grid acoustic center correction.

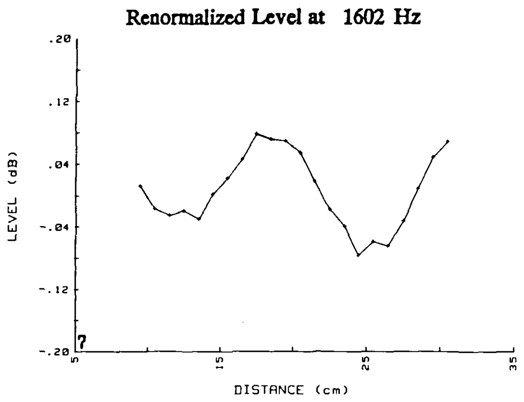
Renormalized Level at 1602 Hz

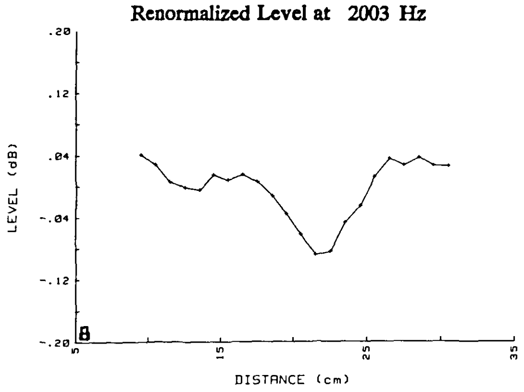
Renormalized Level at 2003 Hz

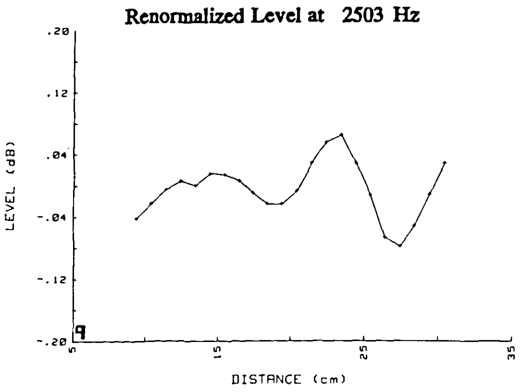
Renormalized Level at 2503 Hz

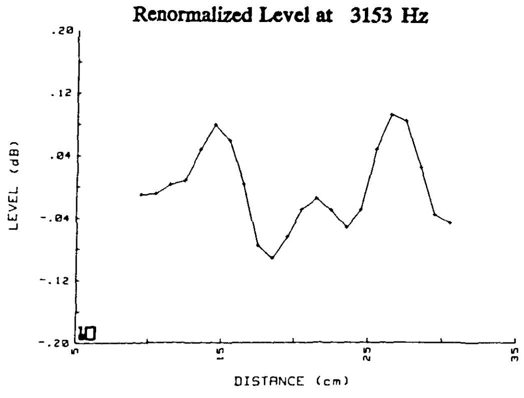
Renormalized Level at 3153 Hz

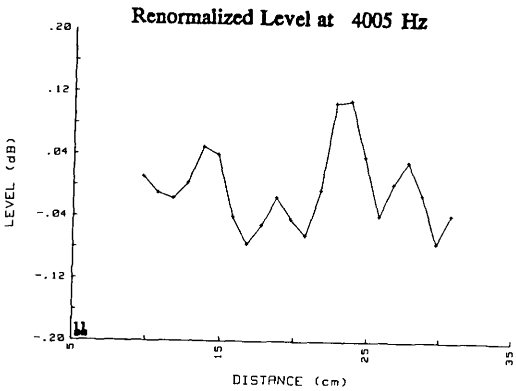
Renormalized Level at 4005 Hz

11

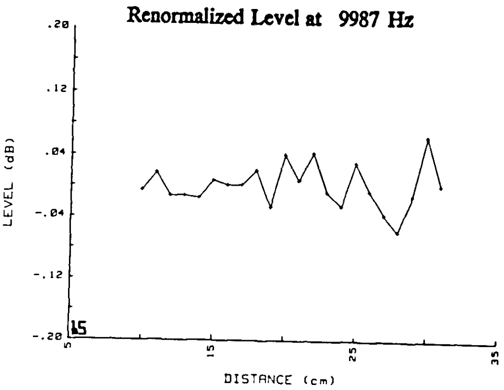
Renormalized Level at 9987 Hz

15

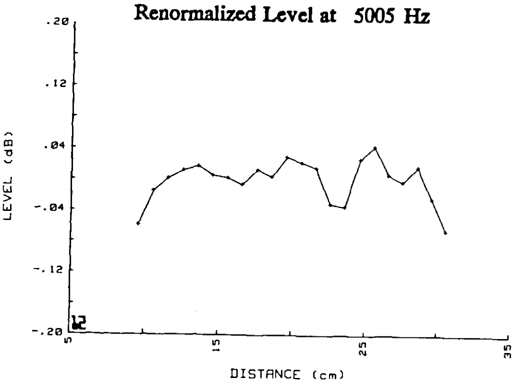
Renormalized Level at 5005 Hz

12

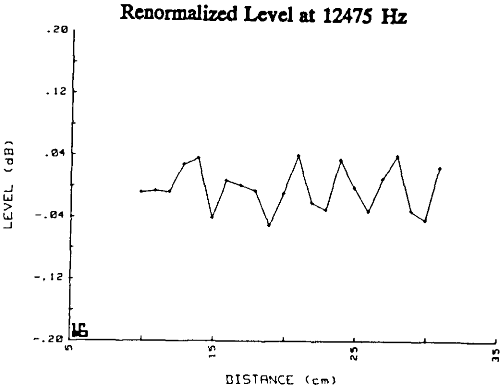
Renormalized Level at 12475 Hz

16

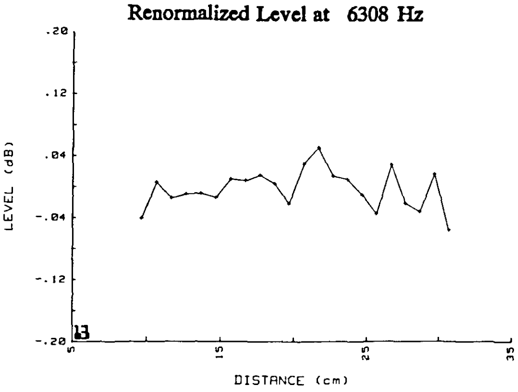
Renormalized Level at 6308 Hz

13

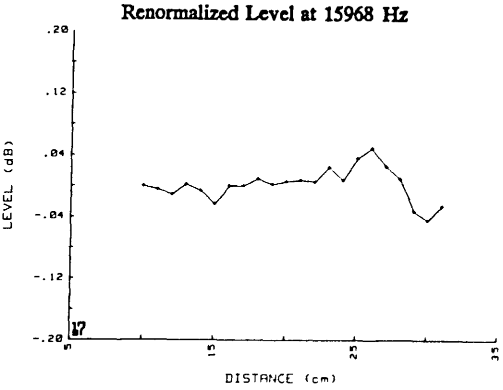
Renormalized Level at 15968 Hz

17

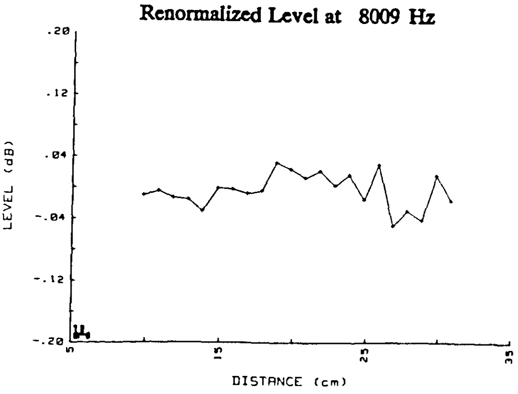
Renormalized Level at 8009 Hz

14

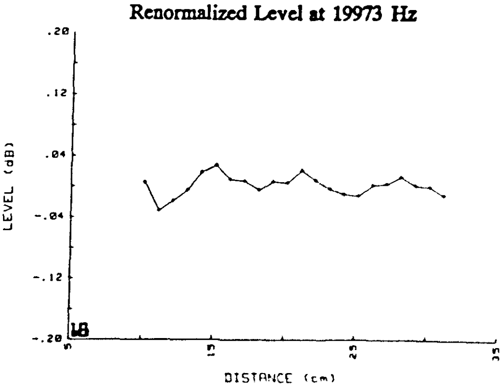
Renormalized Level at 19973 Hz

18

though the first-order regression coefficient is essentially zero, not all renormalized data points show the same level. Table 2 summarizes these renormalized levels at 15 cm, 20 cm and at the distance between 15 and 25 cm at which the worst deviation of measured level from the zero value occurs, and the value of that deviation. These deviations from zero give insight into the spatial characteristics of the sound pressure field in the chamber, and the proper choice of test parameters. These deviations most probably could be due to unaccounted-for near-field effects, or one or more of three factors: normal modes (standing waves) due to reflections within the chamber, standing waves due to reflections between the microphones, and electrical crosstalk. We will consider the possible influence of these three factors in sequence.

Factor 1. Many of the reflections within the anechoic chamber will produce deviations from the inverse distance relationship which appear somewhat random. However, in the simplest example, axial modes in the chamber that include waves with propagation vectors parallel to the axis of rotational symmetry of the microphone will produce pressure maxima or minima at integer multiples of one-half wavelength apart. For example, figure 10 shows maxima at separation distances of about 15 and 27 cm. The differences of 12 cm in the separation distances correspond reasonably closely to the wavelength for 3.15 kHz, which is approximately 11 cm. However, there is no maximum of closely comparable value at about 20 cm to 21 cm, so that the pressure standing wave pattern is clearly influenced by other (non-axial) modes within the chamber, or by other factors, as well.

Factor 2. Standing waves due to reflections between the microphones themselves will also produce maxima or minima at separation distances that are integer multiples of one-half wavelength. Such effects are seen at some frequencies. For example, at 4.0 kHz the minima seen in figure 11 are at separation distances of 12, 17, 21, 26, and 30 cm. The wavelength at 4.0 kHz is approximately 8.6 cm. However, it is not possible completely to separate the effects which are due to standing waves caused by reflections from interior surfaces of the chamber (or "room reflections") and those due to standing waves caused by reflections between the microphones. It would be expected that the effect of microphone reflections would become more pronounced as the frequency is increased (as wavelengths become comparable to the microphone diameter), and less pronounced as the separation distance between the microphones increased, since

Table 2. Measured acoustic center positions expressed as grid-to-grid distance corrections, levels measured at specific grid-to-grid distances renormalized (as in figs. 5–18) for effects of these measured acoustic center positions, and worst case grid-to-grid distances.

Freq.	Measured Grid-to-Grid Correction	Level @ 20 cm Renormalized for Measured Grid-to-Grid Correction	Level @ 15 cm Renormalized for Measured Grid-to-Grid Correction	Level @ Worst Case Renormalized for Measured Grid-to-Grid Correction	Worst Case Grid-to-Grid Distance
	cm #	dB +	dB +	dB +	cm *
1001	−0.70	−0.05	0.01	−0.06	23
1251	−0.14	−0.06	−0.09	−0.11	17
1602	−0.52	0.07	0.00	−0.08	25
2003	−0.46	−0.04	0.01	−0.09	22
2503	−0.61	−0.02	0.02	0.06	24
3153	−0.52	−0.06	0.08	−0.09	19
4005	−0.26	−0.04	0.04	0.11	24
5005	−0.44	0.03	0.00	−0.03	24
6308	−0.34	−0.02	−0.01	0.05	22
8009	−0.21	0.02	0.00	0.03	19
9987	−0.05	0.01	0.04	0.04	22
12475	−0.14	−0.01	−0.04	−0.05	19
15968	0.01	0.01	−0.02	0.04	25
19973	0.12	0.00	0.03	0.03	15
Total of absolute values		0.44	0.39	0.87	
Average of absolute values		0.031	0.028	0.062	

* The worst-case spacing was evaluated only for distances between 15 and 25 cm.

\# The acoustic center correction for a microphone, referred to the grid, is one-half of the grid-to-grid distance correction. A negative number indicates that the acoustic center is in front of the grid, i.e., outside its exterior surface.

\+ The error in a calibration produced by the deviation from zero in level at a given distance and frequency will be one-half of the given deviation.

the microphones do become much more directional at high frequencies, but sound is not scattered from the microphones by specular reflection in the range of frequencies studied. It is also expected that the effect of room reflections would be more pronounced at the lower frequencies of measurement, at which the dimensions of the sound-absorbing wedges on the walls are smaller compared to the wavelength of the sound. Since the observed deviations in level become larger at lower frequencies, it would appear that room reflections are more significant in effect than standing waves due to reflections between the microphones. Although the effects of such standing waves do not appear important in the current system, these effects most probably can be reduced even further or eliminated by tilting the plane of either microphone diaphragm a few degrees. However, such a controlled shift in our chamber would require extensive modifications to the microphone-supporting structure.

Factor 3. If present, significant crosstalk between the drive signal and the detection system will produce relative maxima or minima spaced one wavelength apart. Such phenomena do appear at some frequencies, as can be seen by comparing figures 12 and 19 for 5005 Hz. The somewhat greater deviations in the data for conventional (lower sensitivity) microphones (Bruel & Kjaer Type 4134) when compared to the data for high-sensitivity microphones (Bruel & Kjaer Type 4165) could indicate some degree of crosstalk. Fortunately, it was possible to reduce the system crosstalk by an additional 10 dB after this greater deviation for conventional microphones was noted. The deviation was not reduced by the decrease in crosstalk. The larger deviation in the data for these low-sensitivity microphones remains unexplained, but may be due to the greater uncertainty of the measurement of the lower output levels, to unknown changes in the standing wave pattern in the chamber associated with slight uncontrolled changes in ambient environmental conditions, or to unwanted sound produced by the stimulus-generating apparatus and therefore correlated with the signal.

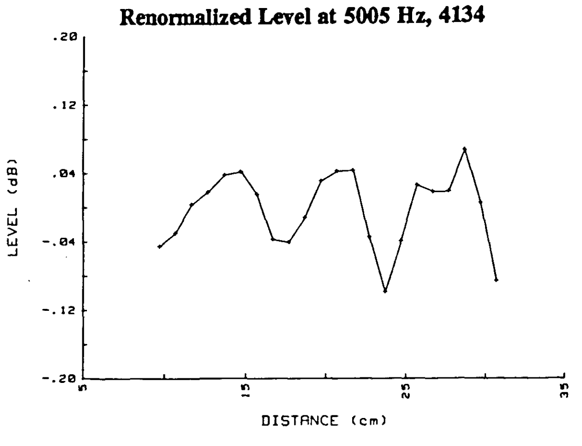

Figure 19–Deviations in level from an inverse distance relationship for the renormalized (as in figs. 5–18) data from two conventional, e.g., sensitivity about −38 dB re 1V/Pa, 1/2-inch microphones for a frequency of 5 kHz.

Ideally, the length of the traverse used to determine position of the acoustic center should be an integral number of wavelengths in order to minimize biasing of the data from end effects. Below 1.6 kHz, the traverse in the far-field is necessarily less than one wavelength, since it is not possible to obtain data at an adequate signal level at separations of more than 31 cm at low frequencies. This limitation on the length of the traverse may explain the apparent decrease in the magnitude of the measured grid-to-grid correction for the acoustic centers (col. 2 of table 1) at 1.25 kHz. It may be possible to slightly increase the accuracy of the evaluation of the acoustic center position at frequencies higher than 1.6 kHz by truncating the data from traverses at an appropriate distance. This approach is under consideration.

Another assumption in the use of the data remains to be tested, namely that a grid-to-grid spacing of 10 cm produces far-field conditions. This can be checked by noting whether the slope of the renormalized data is zero at the 10 cm spacing. Deviations in the slope due to chamber effects such as standing waves make it difficult to determine if the slope is indeed zero at this distance. An inspection of the data does indicate that spacings of less than this amount could not be used. This is another area in which slight improvements in accuracy may be possible in the future.

Most of the above determinations were made with Bruel & Kjaer Type 4165 microphones, with the protective grids in place. Essentially similar measurements were performed at a limited number of frequencies with the grids removed from the microphones, and for other types of 1/2-inch microphones. Very long time constants and time-consuming mechanical adjustments can be required for these measurements. In fact, it is not even feasible to make such measurements over the lowest portion of the frequency range with other than high-sensitivity microphones. Figure 20 summarizes the results for all types of microphones examined. At three frequencies spanning the frequency range, measurements were made using

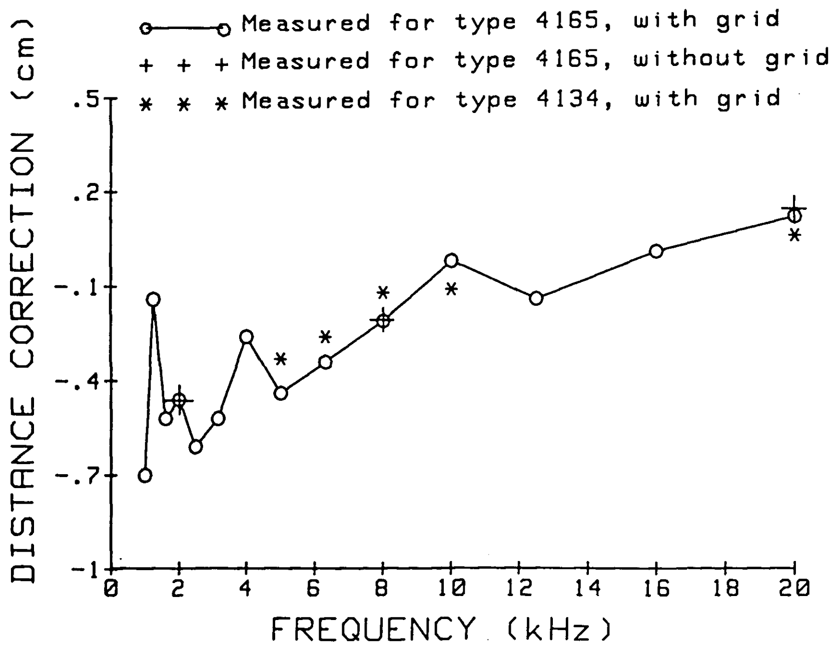

Figure 20–Summary of measured acoustic-center-position corrections for two 1/2-inch microphone types from 1 kHz to 20 kHz. The ordinate shows the distance correction for two microphones, to be added to the grid-to-grid separation of the microphones. One set of measurements for Type 4165 microphones was taken with their protection grids removed; these distance corrections are to be added to the grid-to-grid separation that would apply if the grids were in position on the microphones.

Type 4165 microphones with the grids removed. (For this condition, distance measurements were made from the position which the grid occupies when it is in place.) The effect of the grid upon the distance correction is seen to be negligible. The results for the Type 4134 microphone do show slight differences from the Type 4165 results. However, this difference is small compared to the total uncertainty of measurement. Furthermore, the higher signal level produces more accurate data for the Type 4165 microphones, and the only significant dimensional differences between the Types 4165 and 4134 microphones are differences in length which, for a given distance from the microphone grid position, should not affect the relative acoustic center location. Consequently, the data obtained with the 4165 microphones with grids in place are used for all calibrations of 1/2-inch microphones.

5. Uncertainties in Determination Of Microphone Response Level

An inspection of eqs (2) and (3) shows the principal sources of uncertainty in the determination of M_{f_a} and R_{f_a} (uncertainties for M_{f_b} and R_{f_b} are similar to those in M_{f_a} and R_{f_a}). Note that, because of the square root appearing on the right-hand side of eq (2), most of the terms that will occur in the evaluation of eq (3) are either divided by two or are expressed as 10 times the logarithm of some quantity, instead of 20 times the logarithm of the quantity. This means that an uncertainty of, for example, 0.01 dB in an attenuator setting produces a calibration uncertainty of only 0.005 dB.

In the expression $[A_{bd}-A_{ad}-A_{ba}]/2$, the uncertainty is considered random, and is dominated by system noise and drift, except possibly at the very highest frequencies of calibration where attenuator inaccuracy (less than 0.01 dB in each measurement A_{xy}) makes a significant contribution. Expressed as two standard deviations (as are all random uncertainties described hereinafter unless otherwise noted), the uncertainty in the above expression may be as large as 0.03 dB at frequencies from 5 kHz to 20 kHz, and as large as 0.09 dB at frequencies from the lower calibration limit of 1 kHz to 5 kHz for high-sensitivity 1/2-inch microphones, and from 1.25 kHz to 5 kHz for low-sensitivity 1/2-inch microphones.

The frequency in the eq (5) is raised to the second power, and consequently the term 20 log f will appear when eq (3) is evaluated. In the current system using a quartz-stabilized frequency synthesizer, the frequency can be determined with high accuracy, to within 20 parts per million or better, resulting in an uncertainty of .0002 dB, which is considered random.

The barometric pressure and the temperature each can be measured to an accuracy which is better than one part in one thousand. An uncertainty of one part in one thousand in each of these quantities produces a calibration uncertainty of 0.004 dB in each. This uncertainty is considered random for both quantities. It is estimated from work done with the NBS system for the pressure calibration of microphones that the uncertainty in the determination of 10 $\log_{10}C_a$ contains systematic and random components of uncertainty that are each less than 0.005 dB.

The term 4.343 $\alpha\, r_{ab}$ is itself small, the maximum value being 0.07 dB at 20 kHz. An uncertainty of 10 percent for the product of $\alpha\, r_{ab}$ will produce an uncertainty in the calibration which is less than 0.007 dB, and is considered random.

Factors affecting the determination of the acoustic center have been discussed in section 4. Some idea of the uncertainty of that determination may be obtained by using the data in tables 1 and 2. A grid-to-grid spacing of 20 cm is chosen for calibration purposes.

The differences between the effects of the second-order-polynomial-fit corrections for distance and the effects of the measured corrections are taken to represent the influences of the uncertainties in the determination of the distance. To the influence of each of these uncertainties expressed as an effect upon corrected level at each frequency is added the corresponding worst-case-distance variation in level shown in column 5, table 2. The worst-case situation for the resulting sum then occurs at 4.005 kHz, where this sum shows a possible discrepancy of magnitude 0.17 dB, for a calibration uncertainty of 0.085 dB. An estimate of 0.1 dB is then a conservative estimate for the magnitude of credible bounds on the calibration uncertainty attributable to the determination of the effective distance between acoustic centers at frequencies 1 kHz to 5 kHz. Of this value, 0.06 dB is considered systematic, and 0.04 dB is considered random. At frequencies above 5 kHz up to 20 kHz, this uncertainty is considered to have a magnitude of credible bounds of 0.055 dB, which is the sum of a systematic component of 0.015 dB, and a random component of 0.04 dB.

The values obtained from the second-order polynomial fit are checked further by comparing them (fig. 21) to the corrections for the acoustic center locations given in figure 6 of reference [5] for a microphone with grid. In order to compare the distance corrections for two microphones, these corrections from reference [5] for the positions of the

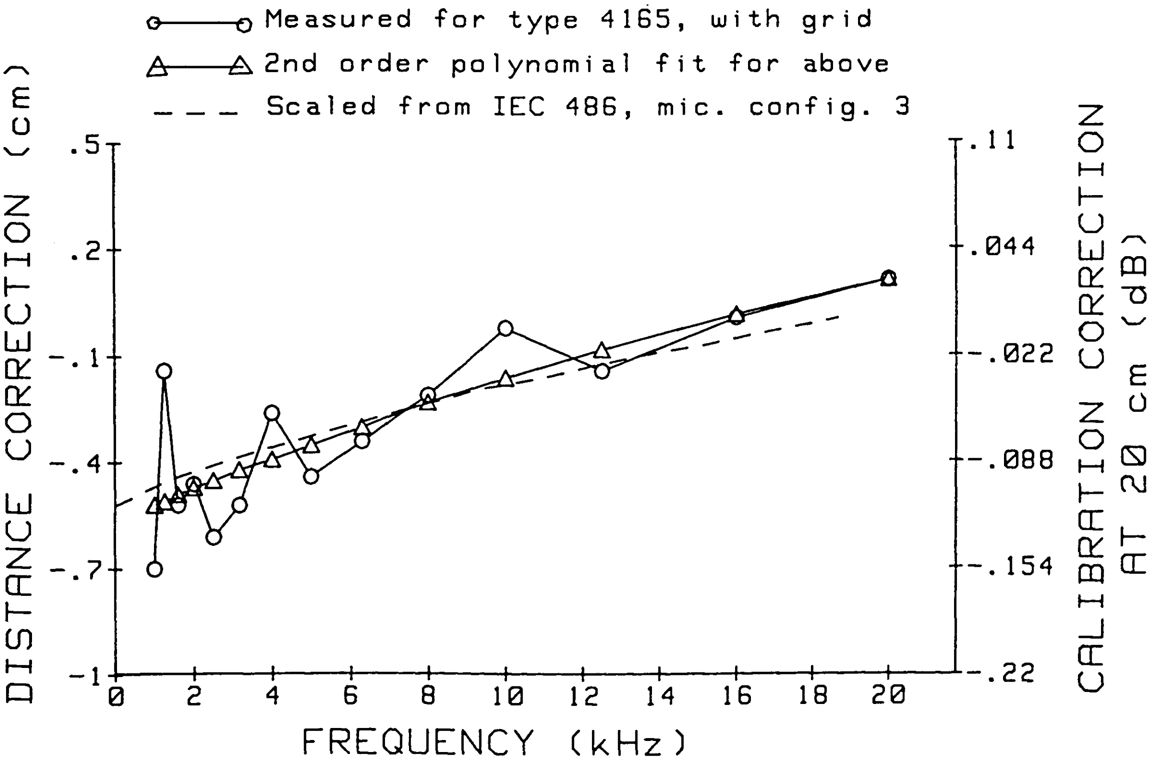

Figure 21–Summary of acoustic-center-position correction for Type 4165 microphones. Two scales for the ordinate are given: the left scale shows the corrections for two microphones, to be added to the grid-to-grid separation of the microphones; the right scale shows the effect upon calibrated microphone response level of applying these corrections to a measured grid-to-grid separation of 20 cm.

acoustic center are doubled. They are then divided by 1.87, which is the ratio of the diameters of the nominal "1-inch" microphones and 1/2-inch microphones. The frequency scale is multiplied by 1.87. These corrections give excellent agreement with the corrections obtained from the polynomial fit, the calibration differences attributable to the differences in these corrections for a spacing of 20 cm being no more than 0.02 dB at any frequency.

It might appear that the accuracy could be improved by correcting for the measured deviations at a specific distance and frequency. In general, this is not the case. The data were taken using an oscillator which had low distortion and high stability in both amplitude and frequency. However, it could not be set precisely and conveniently to the desired one-third octave center frequencies. Furthermore, calibrations may be needed at other than the one-third octave center frequencies. A frequency synthesizer is now used in the system instead of the oscillator, and its frequency can be set precisely and conveniently to the desired values. Even so, changes in atmospheric conditions or in the configuration of the chamber will cause changes in the standing wave patterns, especially at high frequencies. For these reasons, the results should be considered exemplary, rather than definitive for all conditions.

The second-order polynomial fit corrections are the ones actually used for calibration purposes. Such use appears strongly justified by the close agreement between the scaled values from reference [5] and the second-order polynomial fit to our measured correction values for microphone acoustic center positions.

Although each determination of the position of the acoustic center contains uncertainties because of the reasons just discussed, the calibration accuracy is not degraded to a similar degree. The correction for the displacement of the acoustic center is a small fraction of the total spacing between the microphone diaphragms, as a consequence of our deliberate choice to work at relatively large (most typically, about 20 cm) spacings.

The purpose of the present study has not been to establish the exact positions of the acoustic centers, but to determine the corrections with sufficient accuracy to perform the calibration. Great effort to achieve adequate signal-to-noise ratios and low crosstalk has enabled measurements to be performed at the relatively large separation distance of 20 cm. This separation distance has also been selected since at all the test frequencies shown in table 2 the value of the renormalized level in column 3 is in magnitude 0.07 dB or less, a smaller value than the corresponding magnitude for either the renormalized levels at 15 cm (column 4) or the worst-case renormalized levels (column 5).

Table 3 shows the estimated random uncertainty in decibels of each term from eqs (3) and (5). Also shown are the random uncertainties (in decibels) contributed to a microphone response level by sources not apparent in eqs (3) and (5): determination of the polarizing voltage, and departures of about 0.2 degree from the normal incidence specified for calibration. These departures reflect the tolerances on mechanical alignment of the rods upon which the microphones are mounted. Table 4 shows estimated credible bounds on the significant systematic components of uncertainty. We have assumed that the standard deviation for each term is one-half the amount shown in table 3. Also, we consider that the uncertainties in table 3 are independent. Then, the overall root-sum-square random component of error (assumed to be two standard deviations) of the measurement ranges from 0.05 dB at high frequencies to 0.10 dB at low frequencies, as shown in table 5. The overall systematic component of uncertainty, expressed as the sum of the systematic components, ranges from

Table 3. Estimated random components of uncertainty two standard deviations from the mean for each term from eqs (3) and (5).

Term from eqs (3) and (5)	Estimated uncertainty (dB)
$[A_{bd}-A_{ad}-A_{ba}]/2$	0.03 (5 kHz $\leqslant f \leqslant$ 20 kHz) to 0.09 (1.25 kHz $\leqslant f \leqslant$ 5 kHz)
$10 \log_{10} C_a$	0.005
$10 \log_{10} p_s$	0.004
$10 \log_{10} T$	0.004
$20 \log_{10} f$	0.0002
$4.343\ \alpha r_{ab}$	0.007
$10 \log_{10} r_{ab}$	0.04
polarization voltage (not in eqs (3) and (5))	0.007 dB
alignment (not in eqs (3) and (5))	0.005 dB

Table 4. Estimated credible bounds on magnitudes of systematic uncertainties of relevant terms from eqs (3) and (5).

Term from eqs (3) and (5)	Estimated upper bound on uncertainty (dB)
$10_{\log} C_a$	0.005
$10_{\log} r_{ab}$	0.015 (5 kHz $< f \leqslant$ 20 kHz) to 0.06 (1 kHz $\leqslant f \leqslant$ 5 kHz)

Table 5. Overall uncertainty estimates.

Frequency Range (kHz)	Estimated Upper Bound on Magnitude of Systematic Component (dB)	Random (Two Standard Deviations) (dB)
$20 > f > 5$	0.02	0.05
$5 > f > 1.25$	0.06	0.10

0.02 dB at high frequencies to 0.06 dB at low frequencies. Our initial objective in developing this measurement service was an overall measurement uncertainty of 0.2 dB or less. Thus, at all frequencies, the sum of the systematic error and two standard deviations, which sum is 0.16 dB at low frequencies and 0.07 dB above 5 kHz, is well within the initial objective.

As mentioned in section 2, the accuracy can be improved by taking additional sets of measurements, a procedure which reduces random uncertainty but does not alter the worst-case estimate of systematic uncertainty. The fixed-cost calibration service from NBS consists of one set of measurements, although a second set or more can be taken at additional cost upon request.

Any significant increase in accuracy of calibration at frequencies from 1 kHz to 5 kHz would require that the signal-to-noise ratio of the detection system be increased. Such an increase would require that either the preamplifier electrical noise be reduced or that the detection time be increased, which in turn would require a decrease in the long-term (during insert voltage measurement) drift of the detection system. To increase the accuracy at all frequencies, the distance which corresponds to the spacing between the apparent acoustic centers would have to be known more accurately, which would require a more nearly perfect anechoic environment.

While further refinement of apparatus is not only possible, but will ultimately become necessary to meet evolving needs, the uncertainties in the current NBS fixed-cost calibration services for 1/2-inch microphones in their frequency range 2.5 kHz to 20 kHz represent an improvement upon those in the corresponding previous (now discontinued) NBS services for "1-inch" laboratory standard microphones in 1965 [8]. When uncertainty is comparably expressed for the "1-inch" microphones as two standard deviations plus the estimated bounds on systematic error, the uncertainty in the calibration of "1-inch" microphones ranged from 0.16 dB to 0.44 dB over this frequency range.

The frequently lower transmitting and receiving sensitivities and the higher electrical impedances of the 1/2-inch microphones result in poorer signal-to-noise ratios, larger crosstalk, and consequently much more formidable difficulties in calibration than those encountered with "1-inch" microphones. Nevertheless, the superiority of current instrumentation, apparatus, and procedures has enabled lower uncertainties to be achieved in the free-field calibration of 1/2-inch microphones than had been achieved in 1965 for "1-inch" microphones.

Emphasis has been given to services for free-field calibration of 1/2-inch microphones because the use of these microphones to perform precision practical measurements is usually not nearly as limited by diffraction effects as is the use of "1-inch" microphones. While "1-inch" laboratory standard microphones can be exceptionally accurate and stable instruments for the measurement of well-specified sound fields under laboratory conditions, such as a uniform plane wave of known angle of incidence, or the sound pressure in an acoustic coupler, practical measurement situations often involve sound fields that are not so well specified. It may be difficult or impossible to choose a single, well-defined calibration (free-field at specified angle of incidence, pressure, or random incidence) that is applicable. The "1-inch" standard microphones are sufficiently large that diffraction effects at frequencies well within the audible range cause substantial differences among the available calibration choices, and ambiguity in choice of the applicable calibration can result in large uncertainty in measurement. The difference between free-field (normal incidence) and pressure response levels for a "1-inch" microphone increases as frequency is increased from a few hundred Hz to about 12 kHz, and can be as large as 9 dB at frequencies below 10 kHz (ref. [3], fig. A3). This difference is about two orders of magnitude larger than the typical uncertainty in reciprocity calibration at these frequencies. Consequently, if "1-inch" microphones are used for measurement of sounds having appreciable spectral energy at high frequencies, overall measurement uncertainty can dwarf uncertainties due to calibration.

Use of 1/2-inch microphones can reduce these uncertainties. Calibrations by reciprocity performed at NBS upon 1/2-inch microphones under comparable conditions have shown that the difference between free-field (normal incidence) and pressure response levels is less than about 4 to 5 dB (depending upon microphone type) at frequencies below 10 kHz, and reaches 9 dB only at about 19 to 20 kHz; i.e., the region of large diffraction effects is shifted to frequencies above 10 to 15 kHz. This shift increases the accuracy of most commonly-performed measurements for two reasons:

1) The objective in many practical situations is to measure the broad-band sound pressure level weighted by one of the standard A, B, or C frequency-response weighting characteristics [9]. These characteristics provide appreciable attenuation at frequencies above 10 to 15 kHz, reducing effects of measurement uncertainty at such high frequencies on the measured broad-band level.

2) The spectra of most common sounds tend to decrease in amplitude as frequency is increased beyond several kHz, so that relatively little spectral energy is likely to be present at frequencies where diffraction effects are large. Consequently, the lesser uncertainty associated with diffraction effects for 1/2-inch microphones at frequencies below 10 to 15 kHz will usually contribute to more accurate measurement of broad-band levels and to more accurate spectral energy data.

6. "One-Inch" Microphones

One-inch microphones can be calibrated by placing commercially-available "1-inch" adaptors on the 1/2-inch mounting hardware. This arrangement produces two nonstandard test conditions. The mounting rod for the microphone is not constant in diameter, but necessarily tapers from a diameter of 0.936 inch at the microphone down to 1/2 inch. The ground-shield geometry is not that specified for calibrating "1-inch" microphones [3], but is that used for 1/2-inch microphones (fig. 3). However, both of these conditions are often encountered in the actual use of some "1-inch" microphones. Under these conditions, the current instrumentation should also result in improved (relative to the 1965 values) values of uncertainty in the calibration of "1-inch" microphones.

Western Electric 640AA "1-inch" microphones cannot be tested with this mounting as the shield of the 1/2-inch preamplifier contacts the center connector of the microphone. Rods and mounting hardware for the present system are available for such "1-inch" microphones. However, the time required for removing the 1/2-inch rods, mounting and aligning the items for these "1-inch" microphones, and ultimately replacing and realigning the 1/2-inch rods is such that a relatively inexpensive fixed-cost calibration service for such "1-inch" microphones is not offered currently.

During calibrations at the NBS, the microphone denoted (d) in eqs (3) and (4) is usually of the 1/2-inch type. However, it could be a "1-inch" microphone, since its purpose is to act as a source in sequential measurements determining the ratio of sensitivities of the two microphones (denoted (a) and (b)) being calibrated. During these calibrations the microphones (a) and (b) are both 1/2-inch microphones, or are both "1-inch" microphones with identical mounting adapters, so that microphones (a) and (b) are substantially similar in size and directional pattern. This similarity helps to ensure that the sound pressure sequentially produced at microphones (a) and (b) by the source microphone (d) is essentially the same, even though the test chamber is not perfectly anechoic. Consequently, the effects of this potential source of additional uncertainty are prevented.

7. Comparison of Experimental and Theoretical Plane-Wave Free-Field Corrections for One-Half Inch Microphones

The mounting of the microphones on 1/2-inch diameter rods extending through the walls of the anechoic chamber during free-field calibrations at normal incidence by the reciprocity method closely approximates the geometry of mounting the microphones upon semi-infinite rods of the same diameter. This choice of a uniform mounting geometry is deliberate, because use of various mounting geometries with the same microphone cartridge would cause differences in its measured free-field response levels. Such differences are due to diffraction about the microphone and its supporting structures, and occur at frequencies sufficiently high that a wavelength of sound is not large compared to the microphone and significant dimensions (e.g., rod diameter) of its supporting structure.

Effects of diffraction upon the sensitivity of practical microphones constitute a principal reason for performing free-field calibrations: if a microphone of adequate sensitivity for a measurement were of negligibly small dimensions relative to the range of wavelengths of sound to be measured, the pressure and the free-field response levels of the microphone would be essentially identical for such a measurement.

Unfortunately, this is not the case for 1/2-inch (or other commonly used) microphones. Furthermore, for a given microphone it is not practical at all frequencies of interest to calculate the plane-wave free-field correction, defined in reference [3] as the free-field response level at a given frequency and orientation with respect to the direction of sound propagation, minus the pressure-response level. This impracticality occurs because this calculation is influenced by the relation between the radiation impedance loading the microphone diaphragm and the acoustic impedance of the microphone itself at that diaphragm. At frequencies approaching the fundamental diaphragm resonance, and above, this radiation impedance is not negligibly small compared with the acoustic impedance of the microphone, and calculations would have to consider the relation between these impedances for each microphone calibrated. This relation may also be dependent on unknown details (e.g., asymmetry) of the diaphragm motion in ways that are analytically intractable.

However, for frequencies at least two or three octaves below the fundamental resonance of the microphone, theoretical corrections can be expected to provide very good agreement with experimentally determined ones. In particular, Matsui [10,11] has derived theoretical plane-wave free-field corrections at normal incidence for a standard microphone with a recessed diaphragm (which he could also apply to the special case of an unrecessed, or flush-mounted, diaphragm). His analysis assumes that the standard microphone is mounted on a semi-infinite rod that has the same diameter as that of the microphone, and that vibrations of the microphone diaphragm are rotationally symmetric. The Matsui correction applicable to the 1/2-inch MR-112 microphone has been evaluated by Miura et al. [12]. Fortunately, this theoretical correction is at its best at the lowest frequencies of free-field calibration by reciprocity, where technical difficulties posed by the lower signal-to-noise ratios, greater effects of crosstalk, and slight departures from anechoic conditions are greatest, and where the NBS methods for pressure calibration by reciprocity are well-developed and relatively more accurate [13].

Consequently, the adequacy of the uncertainty estimates for the free-field calibration in the most difficult frequency range can be checked by comparing the theoretically and experimentally determined plane-wave free-field corrections for 1/2-inch microphones.

Figure 22 shows such a comparison, for an E.C.L. MR-112 1/2-inch microphone with protective grid removed, using the evaluations of Mat-

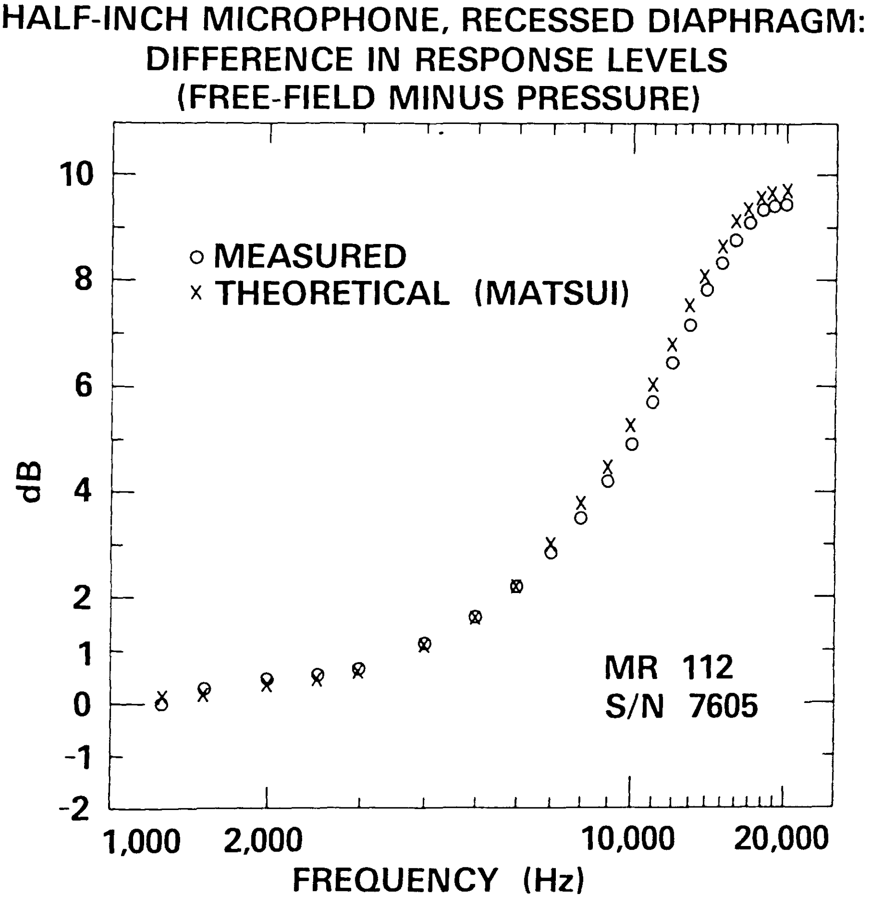

Figure 22-Comparison of experimentally and theoretically determined plane-wave free-field corrections (free-field response level at normal incidence minus pressure response level) for an E. C. L. Type MR-112 1/2-inch microphone with a recessed diaphragm configuration.

sui's theoretical expressions [10,11] by Miura et al. [12] where available, and a low-frequency approximation [11] at other frequencies (e.g., 1.25, 1.5 and 2.5 kHz). The nominal fundmental resonance freqency of the MR-112 is 30 kHz. At frequencies below 7 kHz, e.g., sufficiently below the resonance frequency, the measured and theoretical free-field corrections agree within 0.15 dB (table 6).

Table 6. Differences between measured and theoretical [after Matsui] plane-wave free-field corrections for 1/2-inch microphones with recessed (MR-112) and flush (Bruel & Kjaer 4134) diaphragm configurations (protective grids removed).

Frequency (kHz)	Difference for MR-112 (dB)	Difference for Bruel & Kjaer 4134 (dB)
1.25	−.13	−.11
1.5	.11	.08
2.0	.15	.08
2.5	.09	−.03
3	.04	−.08
4	.05	(−.16)*
5	−.03	(−.37)*
6	−.04	
7	−.10	

* Note: The low-frequency approximation to Matsui's theoretical correction [10] that was used for the Bruel & Kjaer 4134 loses validity at 4 to 5 kHz. Consequently, the differences at these frequencies show divergence between measured and theoretical values for this microphone.

Figure 23 shows the comparison of free-field plane-wave corrections for a Bruel and Kjaer Type 4134 1/2-inch microphone with protective grid removed. This microphone has a geometry that is approximated by a 1/2-inch diameter cylinder of which the microphone diaphragm constitutes the exposed face, i.e., the diaphragm is unrecessed (flush-mounted). The theoretical plane-wave free-field correction was calculated for this geometry using the approximate low-frequency correction [11] of Matsui. Theoretical corrections were plotted only at frequencies of 5 kHz and lower, because this theoretical approximation is probably losing validity at about 5 kHz, and also because this microphone type has a nominal resonance frequency of 23 kHz, so that experimental and theoretical corrections would not be expected to be nearly equal at frequencies above about 3 to 5 kHz. The agreement (table 6) at frequencies 3 kHz and below is within 0.11 dB, which is excellent. Even at 4 kHz,

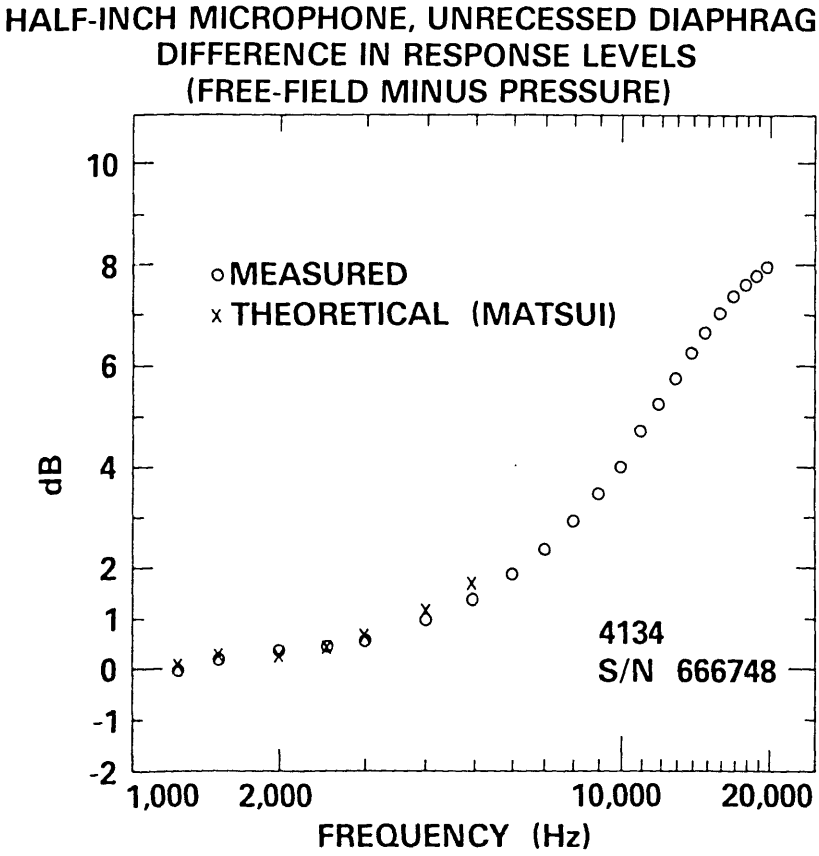

Figure 23–Comparison of experimentally and theoretically determined plane-wave free-field corrections for a Bruel and Kjaer Type 4134 microphone with an unrecessed (flush-mounted) diaphragm configuration.

the agreement is 0.16 dB. Only at 5 kHz, where the agreement is 0.37 dB, and where we have little confidence in the theoretical low-frequency approximation, does divergence become obvious. We rely upon the theoretical diffraction corrections as a check upon experimental results at frequencies below 4 kHz, the most difficult frequency range for free-field calibration by the reciprocity technique. We conclude that at these frequencies the agreement between measured and theoretical plane-wave free-field corrections is consistent with expectations based on the uncertainty estimates for free-field calibration presented herein, the uncertainty (probably at least several hundredths of a decibel) in the theoretical diffraction correction, and the uncertainty in pressure calibration by the reciprocity method in essentially closed couplers (see ref. [13]).

8. Considerations Concerning Free-Field Calibrations Traceable to the NBS

For both types of microphone geometry represented in figures 22 and 23, the values of both the theoretical and experimental plane-wave free-field corrections are less than 0.5 dB at frequencies of 2 kHz and below. The smallness of these corrections at 2 kHz and below is a principal reason that the fixed-cost calibration services for free-field calibration of 1/2-inch microphones at NBS begin at a lowest frequency of 2.5 kHz, with lower frequencies available at cost, upon special request.

A number of users of the NBS pressure calibration services send commonly-used types of "1-inch" microphones to the NBS for fixed-cost pressure calibration at frequencies from 50 Hz to 20 kHz, and infer the free-field calibration from this pressure calibration by employing tabulated frequency-dependent values standardized [3,14] for given "1-inch" laboratory standard microphone types and orientations.

However, Koidan and Siegel [15] at the NBS performed measurements of the free-field plane-wave correction for a group of such microphones, and showed that the measured differences in these free-field corrections between individual microphones of the same type were larger than could be attributed to experimental errors. In particular, they found that differences between these corrections measured for each of a group of seven Western Electric Type 640AA and two Electrical Communication Laboratory Type MR103 condenser microphones were largest at frequencies above about 6 kHz, and that these differences could be as large as 0.9 dB at 10 kHz. Citing a pertinent analysis by Foldy and Primakoff [16], Koidan and Siegel attributed these differences to the dependence of the free-field correction upon the acoustic driving-point impedance and radiation impedance of the microphone for plane waves incident on the diaphragm, and noted that different microphones of the same type have somewhat different acoustic impedances. Koidan and Siegel [15] further demonstrated a correlation between their measured free-field corrections and their measured acoustic stiffness constants of individual microphones. These results demonstrate that for measurements of the highest accuracy and precision, the determination of the free-field response level from measurements of the pressure response level and the addition of a "standard" free-field correction should be viewed with caution. For microphones manufactured with close tolerances upon their acoustic impedances, differences in the free-field correction of a given microphone from the standard correction can be expected to be smaller. Koidan and Siegel demonstrated that if data from the two Type 640AA microphones with unusually high diaphragm stiffness and acoustic resistance were excluded from their results, the range of free-field corrections measured at 10 kHz for the remaining group of five Type 640AA microphones and two Electrical Communication Laboratory Type MR103 microphones was reduced from 0.9 dB to less than 0.4 dB. This expectation is also supported by the mostly unpublished data and analysis that led to the IEC tabulations [14] of such standard corrections. For such microphone types as well as for 1/2-inch microphones, however, more extensive, archivally published data similar to that of Koidan and Siegel [15] are not available, and would be required to establish greater confidence in the uncertainties associated with standardized corrections.

Consequently, for the most demanding applications, we consider that the uncertainties associated with the use of standardized frequency-dependent conversion values at frequencies above a few kHz for specified microphone types and orientations are too large to permit this procedure to be used with the pressure calibration of a given microphone as a substitute for the NBS primary free-field calibration of that microphone.

In particular, we recommend that users of the NBS microphone calibration services who seek the most accurate free-field calibration traceable to the NBS obtain the free-field calibration of a 1/2-inch laboratory condenser microphone by the reciprocity method.

During the earliest phases of this work, R. K. Cook and E. B. Magrab provided useful comments, and W. R. Penzes helped to prepare the apparatus, especially the insert-voltage preamplifier for the receiving microphone and the source microphone assembly. F. Lalli and M. Tarica participated in acquiring some of the data presented.

10. References

[1] Cook, R. K., Absolute pressure calibration of microphones, J. Res. Natl. Bur. Stand. (U.S.) **12** 415–420 (1941).

[2] Wathen-Dunn, W., On reciprocity free-field calibration of microphones, J. Acoust. Soc. Am. **21** 542–546 (1949).

[3] *Method for the Calibration of Microphones*, ANSI S1.10-1966, American National Standards Institute, New York.

[4] Koidan, W., Method for measurement of |E'/I'| in the reciprocity calibration of microphones, J. Acoust. Soc. Am. **32** 611 (1960).

[5] *Precision Method for Free-Field Calibration of One-Inch Standard Condenser Microphones by the Reciprocity Technique*, IEC 486-1974, International Electrotechnical Commission, Geneva, Switzerland.

[6] Hunt, F. V., Electroacoustics: the analysis of transduction and its historical background, New York: American Institute of Physics for the Acoustical Society of America, 1954, 1982, 260 pp.

[7] *Method for the Calculation of the Absorption of Sound by the Atmosphere*, ANSI S1.26-1978 (ASA 23-1978), American Institute of Physics for the Acoustical Society of America, New York.

[8] Wildhack, W. A.; R. C. Powell and H. L. Mason, eds., Accuracy in measurements and calibrations, 1965, Natl. Bur. Stand. (U.S.) Tech. Note 262, 145 pp (June 1965).

[9] *Design Response of Weighting Networks for Acoustical Measurements*, ANSI S1.42-1985, American Institute of Physics for the Acoustical Society of America, New York.

[10] Matsui, E., Free-field correction for laboratory standard microphones mounted on a semi-infinite rod, J. Acoust. Soc. Am. **49** (5 pt. 2) 1475–1483 (May 1971).

[11] Matsui, E., On the free-field correction for laboratory standard microphones mounted on a semi-infinite rod, Natl. Bur. Stand. (U.S.) NBS Rep. 7038 (1960).

[12] Miura, H.; T. Takahashi and S. Sato, Corrections for 1/2-inch laboratory standard microphones, Electrotechnical Laboratory Japan Report EA77-41 (in Japanese) 22 pp. (November 1977).

[13] Nedzelnitsky, V., Uncertainties in wideband sound pressure calibration of type L microphones at NBS using acoustic couplers and the reciprocity method, J. Res. Natl. Bur. Stand. (U.S.). in press.

[14] *Values for the Difference between Free-Field and Pressure Sensitivity Levels for One-Inch Standard Condenser Microphones*, Geneva: International Electrotechnical Commission Publication 655; 1979.

[15] Koidan, W. and D. S. Siegel, Free-field correction for condenser microphones, J. Acoust. Soc. Am. **36** 2233–2234 (November 1964).

[16] Foldy, L. L., and H. Primakoff, A general theory of passive linear electroacoustic transducers and the electroacoustic reciprocity theorem. I, J. Acoust. Soc. Am. **17** 109–120 (October 1945).

APPENDIX

Key Instruments* Used in Free-Field Calibration System of Figure 1.

Preamplifier: NBS-modified version of Bruel and Kjaer Type 2619. Subsequently to establishment of the system, the Bruel and Kjaer Type 2645 preamplifier with insert-voltage capability has become available commercially. Although not tested in our system, this preamplifier could reasonably be expected to provide comparable performance to the NBS-modified 2619, provided that the manufacturer's recommendation for compatibility of microphones (especially with regard to resistance of the microphone insulator) used with the 2645 are followed.

Measuring amplifier: Brüel and Kjaer Type 2608, modified for precise control of polarization voltage by means of a 10-turn precision potentiometer.

One-third octave band-pass filter: Bruel and Kjaer Type 5004.

Lock-in amplifier: Princeton Applied Research Model 129A.

Digital voltmeter (reading dc output of lock-in amplifier): Keithley Model 172.

---

* Instruments are identified only in order to adequately specify experimental apparatus and procedures. The presence of an instrument on this list should not be interpreted to imply that this instrument is the best or the only device available for its intended purpose.

Digital voltmeter (used to check dc polarization voltages): Keithley Model 619 Electrometer/Multimeter.

Oscillator: Krohn-Hite Model 4025R (used mostly in earlier stages of work) *or* (more recently) Hewlett-Packard Model 3325A Synthesizer/Function Generator with high stability frequency reference option. The output of the 3325A is suitably attenuated (not shown in fig. 1) before entering the isolation transformers and tuning input of the lock-in amplifier.

Amplifier (at output of Oscillator): Hewlett-Packard Model 467A.

Precision Attenuator: Daven Spec. 8304.

Barometer: Wallace & Tiernan Model FA 139210.

Isolation transformers: Gertsch Model ST-200.

Conferences / Events

FUNDAMENTAL MEASUREMENTS ON OPTICALLY PREPARED ATOMS: A WORKSHOP

Measurements of our fundamental scaling parameters (e.g., R_∞, α, m_e/m_p) as well as tests of our basic theories of matter and radiation are frequently obtained from high resolution spectroscopic measurements on atomic systems. The new and evolving technologies of laser spectroscopy, laser cooling and trapping of atoms as well as squeezed states will have a dramatic impact on this area of metrology. While these topics have received a great deal of attention in their own right, there has not been a forum in which their impact on the field of fundamental measurements has been specifically addressed. For this reason, the National Bureau of Standards hosted a workshop on "Fundamental Measurements on Optically Prepared Atoms" on September 29–30, 1986.

The workshop was divided into four half-day sessions. The first dealt with atomic states and structural parameters. It was highlighted by talks involving the quantum mechanical aspects of the atom-photon interaction. The exchange of photons between atoms and the light field were treated in a way that illustrated phenomena such as anti-bunching, squeezed states and optical bistability. Similarly, the interaction of a single atom with several resonant fields was even shown to allow observation of the internal state of the atom in real time (observation of "quantum jumps"). The second session dealt mainly with the kinetic state or velocity of atoms. Demonstration of highly efficient new laser-cooling techniques based on stimulated processes as well as spontaneous emission and speculation on what may be possible with ultra-cold atoms made for a very lively and exciting session. The idea that an atom placed in a box and cooled to a temperature so low that the deBroglie wavelength is long compared to atomic dimensions might lead to confinement with almost no perturbation from encounters with the walls. If verified experimentally, this idea could have profound consequences for precision measurements.

The third session dealt with the limits to measurement accuracy as we understand them today and how those limits come into play with the new spectroscopic and cooling techniques. The last session dealt with an important applied field: the use of optically prepared atoms in frequency standards. Since frequency standards have many orders of magnitude more precision and accuracy than any other standard, they represent a great testing ground for the concepts discussed during the workshop.

The workshop was attended by 45 people. Seven countries were represented with 40% of the attendees from outside the United States. Twenty-seven papers were presented in the four half-day sessions, which had to be augmented with an evening session to accommodate the lively discussion that followed most of the papers. The format of informal talks with no subsequent publication of papers was designed to encourage speculation and judging from the discussion during and following many of the talks, we were quite successful.

A list of the workshops and talks follow:

Internal States of Atoms

H. J. Kimble:	Non-Classical Dynamics With Intra-Cavity Atoms
P. Toschek:	Absorption by the Numbers:

Recent Spectroscopy of Trapped Ions
D. McIntyre: Two-Photon Optical Ramsey Spectroscopy of Freely Falling Atoms
L. Hunter: Search for an Electric Dipole Moment of the Electron
T. Bergeman: Proposed Application of Decelerated Atomic Beams to Observe Long-Lived (Interference Stabilized) Stark Resonances
S. A. Lee: Fast Beam Laser Spectroscopy: Present and Future
W. Fairbank: Precision Wavelength Measurement of Te_2 Reference Lines Near Hydrogen and Positronium Transitions at 4880Å

External Atomic States

S. Chu: Laser Cooling and Trapping of Atoms: Where are the Limits?
C. Salomon: Cooling Atoms With Stimulated Emission
J. Hall: Some Ideas About Experiments With Freely Falling Atoms
W. Ertmer: Preparation of Cold Atoms for Precision Measurements
W. Phillips: New and Future Experiments on Cooling and Trapping of Neutral Atoms
F. Plumelle: Experiments on Laser Cooled Mg^+ Ions
B. Jaduszliwer: Electron-Cesium Collisions With Optical State Preparation and Analysis
J. Bahns: On Containerless Condensation of "Mirror" Matter

Measurement Limitations and Systematic Effects

D. Wineland: Fundamental Limits to Spectroscopic Accuracy
J. S. Boulanger: Requirements for Evaluatable Environments
J. Shirley: Majorana Effects in Atomic Beams
A. DeMarchi: Does Spin Exchange Limit the Density of Neutral Vapors for Accurate Measurements?
G. Hanes: Candidate Ions for Extended Observation Periods
R. Douglas: Multiphoton Ionization for Atom-State Detection or State Preparation

Optically Pumped Frequency Standards

G. Theobald: Detailed Studies of Cesium Beam Optical Pumping; Applications to an Atomic Clock
J.-L. Picqué: Laser Cooling and Optically Pumped Cesium Beam Frequency Standards
A. Clairon: The LPTF Optically Pumped Cesium Frequency Standard
R. Drullinger: Design of the NBS Optically Pumped Frequency Standard
M. Ohtsu: Ultrahigh Sensitive Frequency Discrimination in Diode Laser Pumped ^{87}Rb Atomic Clocks
H. Robinson: The Temperature Dependence of the Wall Shift in Some Evacuated Rb Cells

---

Robert E. Drullinger
Workshop Chairman
Time and Frequency Division
Center for Basic Standards
National Bureau of Standards
Boulder, CO 80303